

A universal law for non-breaking surface wave decay

Guoqiang Liu^{1,*} and Maryam Al Alshehhi¹

¹*Civil, Infrastructural and Environmental Engineering,
Khalifa University of Science and Technology, Abu Dhabi, United Arab Emirates*

Macroscopic friction can emerge from microscopic fluctuations whose mean vanishes but whose autocorrelation does not [1, 2]. Here we use this statistical-mechanical route to resolve a sixty-year-old problem in ocean wave physics, how non-breaking surface waves lose energy to upper-ocean turbulence [3–5]. The Navier–Stokes equations contain a stochastic vortex force (the coupling between wave orbital motion and turbulent vorticity fluctuations) that classical wave-current theory [6, 7] discards because its phase average is zero. Yet its finite-time autocorrelation survives, yielding a non-negative Green–Kubo friction coefficient and, with inertial-range scaling, a parameter-free decay law determined by the turbulent dissipation rate, wave frequency and gravity. Remote ocean swell, where competing processes are weak, isolates this mechanism for direct test. The same framework predicts two observational signatures that previous analyses missed. The standard satellite estimator systematically exceeds the physical decay rate because of an Itô correction, and a substantial fraction of individual tracks must display apparent energy gain. These events are not merely outliers or measurement artefacts, but the most discriminating fingerprint of the stochastic theory. Both predictions are supported by global satellite observations. Our results reveal a hidden non-breaking pathway by which upper-ocean turbulence drains wave energy into the ocean interior, and show how macroscopic dissipation can emerge from fluctuations that deterministic averaging eliminates.

In Brownian motion a zero-mean random force, negligible in any single collision, produces a measurable friction coefficient once its autocorrelation is integrated through the Green-Kubo relation [1, 2, 8]. We show that a similar statistical-mechanical route resolves a sixty-year-old problem in wave physics.

Wind pumps roughly 60 TW into the ocean surface through waves [9, 10]. Wave breaking is the principal irreversible pathway with an established physical mechanism [5, 11] in the open ocean, but it becomes rare for non-breaking surface waves such as swell, which nevertheless continue to decay measurably across entire ocean basins [3, 4]. Molecular viscosity underpredicts the required attenuation by four orders of magnitude. Eddy-viscosity closures overpredict it by two to three [5, 12]. The laminar air-side boundary layer [13] remains an order of magnitude too weak [14, 15]. A first-principles explanation has been missing since the first trans-Pacific tracking experiment [3].

The obstacle is structural, not merely quantitative. Classical wave-current theory is built on phase averaging [6, 7, 16], which captures the cycle-mean coupling but removes every fluctuating contribution whose phase average vanishes. The procedure is analogous to retaining only the mean force on a Brownian particle and discarding the thermal noise. The resulting phase-averaged dynamics contains no mechanism for fluctuation-induced friction. In operational wave models, swell attenuation must therefore be supplied as an empirical source term rather than derived from the governing equations [12, 17–19].

Remote ocean swell isolates the missing coupling for direct test. After leaving the storm, breaking, wind input and nonlinear transfer are all strongly reduced, so weak non-breaking losses accumulate coherently over planetary scales and become measurable by satellite altimetry [4, 20]. The observations contain a more discriminating clue than the mean decay rate alone. A

reproducible fraction of individual satellite tracks yield apparent negative attenuation, that is, inferred swell growth along the track [4, 14]. One in eight to one in four tracks across independent datasets [4, 20] display this signature. A deterministic decay law cannot produce such a tail. A stochastic dissipation process predicts it as a natural consequence of finite-sample fluctuations, just as Brownian displacement includes excursions against the mean drift.

Here we identify the missing pathway as a stochastic vortex force, present in the Navier-Stokes equations but discarded by phase averaging, whose Green-Kubo autocorrelation integral yields a closed-form, parameter-free swell decay law and simultaneously predicts the full distribution of single-track satellite estimates. We test both predictions against 241 trans-oceanic events.

The stochastic vortex force

Within the present non-breaking, potential-wave framework, phase-averaging discards the only non-viscous term whose autocorrelation can produce irreversible swell dissipation. The total velocity field admits the Helmholtz decomposition [21] $\mathbf{U} = \mathbf{u}_\phi + \mathbf{u}$, where $\mathbf{u}_\phi = \nabla\phi$ is the irrotational wave orbital velocity and \mathbf{u} contains all rotational motions. Substituting into the Navier-Stokes momentum equation and collecting terms, the wave-current coupling reduces to a single non-viscous channel, the orbital vortex force $\mathbf{f}_v = \mathbf{u}_\phi \times \boldsymbol{\omega}$, where $\boldsymbol{\omega} = \nabla \times \mathbf{u}$ (SI S1 A-B).

The vorticity $\boldsymbol{\omega}$ contains contributions on very different timescales. Extending the Craik-Leibovich decomposition [7] we separate the rotational vorticity into three layers, the ensemble-mean $\bar{\boldsymbol{\Omega}}$, the wave-slaved oscillation $\boldsymbol{\omega}_{\text{wave}}$, and the autonomous turbulent fluctuation $\boldsymbol{\omega}'$ (SI S1 D-E). The vortex force inherits the split:

$$\mathbf{f}_v = \underbrace{\mathbf{u}_\phi \times \bar{\boldsymbol{\Omega}} + \mathbf{u}_\phi \times \boldsymbol{\omega}_{\text{wave}}}_{\text{deterministic sector}} + \underbrace{\mathbf{u}_\phi \times \boldsymbol{\omega}'}_{\text{stochastic vortex force}}. \quad (1)$$

95 Phase averaging yields, at leading order, $\langle \mathbf{u}_\phi \times \bar{\boldsymbol{\Omega}} \rangle_\varphi = \mathbf{0}$ and $\langle \mathbf{u}_\phi \times \boldsymbol{\omega}' \rangle_\varphi = \mathbf{0}$, while the wave-slaved term rectifies, via the phase-averaging identity[7], into the Craik-Leibovich vortex force $\mathbf{u}_s \times \boldsymbol{\Omega}_s$ (where $\boldsymbol{\Omega}_s = \bar{\boldsymbol{\Omega}} + \boldsymbol{\omega}'$ is the full phase-averaged but not ensemble-averaged vorticity) that drives Langmuir circulations[6, 16, 22]. But irreversibility is controlled not by a one-time phase average but by the two-time autocorrelation entering the Green-Kubo formula. At that level the discarded term $\mathbf{u}_\phi \times \boldsymbol{\omega}'$ survives, whereas the rectified CL force remains a zero-frequency quantity and cannot damp the resolved swell mode.

107 We call $\mathbf{f}_{\text{svf}} = \mathbf{u}_\phi \times \boldsymbol{\omega}'$ the *stochastic vortex force* (SVF). Figure 1a-c illustrates a single wave-eddy encounter: the CL contribution carries no spectral weight at the wave frequency and therefore cannot contribute to the mode-level friction coefficient, whereas the SVF produces irreversible transfer, depositing a small random energy increment into the rotational flow. Neither the sign nor the magnitude of this increment is predictable for a single encounter. The wave may gain or lose energy depending on the instantaneous phase of $\boldsymbol{\omega}'$. Figure 1d shows the SVF autocorrelation. Although the correlation need not be strictly positive at all lags, its time integral (the Green-Kubo coefficient) is non-negative (see below). Over the $N \sim 10^5$ near-independent encounters along a trans-oceanic path, the cumulative energy change is a biased random walk (Figure 1e, Supplementary Video 1).

124 Irreversibility from reversible dynamics

125 At the wave-subspace level, the relevant object is not the field $\mathbf{f}_{\text{svf}}(\mathbf{x}, t)$ itself but its projection onto the resolved swell mode. For a narrow band centred on k , any physical force enters the amplitude equation through its mode projection $F_k(t) = \int \psi_k^* \cdot \mathbf{f} d^3x$ (Methods, equation (8)). Under Assumptions A2-A5, the only bath-driven contribution is the projected SVF, whose autocorrelation enters the Green-Kubo formula.

133 Applying Mori-Zwanzig[8, 23, 24] to the resolved amplitude $a_k(t)$ yields a generalised Langevin equation with this projected SVF as the fluctuating force. The second fluctuation-dissipation relation (FDR-II)[8, 23, 25] then connects the memory kernel to the force autocorrelation: $K_k(\tau) = \langle F_k(0) F_k^*(\tau) \rangle / \langle |a_k|^2 \rangle$ (Methods, equation (9), SI S2B). For remote swell the wave and local turbulence originate from independent sources separated by thousands of kilometres, so their cross-correlation vanishes to leading order (Assumption A3, SI S2B-C). When the force correlation time τ_c is much shorter than the damping time Γ^{-1} , the memory integral reduces to the Green-Kubo formula[1, 2, 26] for the damping rate Γ :

$$\Gamma(k) = \int_0^\infty \text{Re} \langle F_k(0) F_k^*(t) \rangle dt / 2E_k \geq 0. \quad (2)$$

146 The force autocorrelation factorises as $\langle F_k(0) F_k^*(t) \rangle =$

147 $2E_k \mathcal{G}_k(t)$, where \mathcal{G}_k depends only on the turbulent bath. The E_k cancels, so Γ is independent of wave amplitude, a material property of the ocean mixed layer, not of the swell passing through it (Extended Data Figure 3). The force is linear in $\boldsymbol{\omega}'$, so only second-order vorticity statistics enter the integral.

153 The inequality in equation (2) is guaranteed by Bochner's theorem[27]. The Green-Kubo integral equals the zero-frequency spectral density of a stationary process, which is non-negative. The ensemble-mean energy therefore decays monotonically: $d\langle E_w \rangle / dt = -2\Gamma \langle E_w \rangle \leq 0$.

159 Irreversibility arises because the turbulent bath is not frozen. $\boldsymbol{\omega}'$ evolves weakly during each encounter, so the SVF force correlation acquires a causal asymmetry that prevents exact elastic reversal. A truly frozen eddy would exchange energy elastically. The weak evolution during the encounter breaks this symmetry, producing a net loss of order $\delta^2 E_k$ while the fluctuation remains of order δE_k (SI S2I). The single control parameter $\delta \equiv u'/c_g \sim 10^{-3}$ - 10^{-2} governs both the bias and the noise (Methods, SI S6).

169 Scale locality and the universal law

170 The sign of Γ is theorem-level (equation (2)). The frequency law is not. To obtain a closed-form $\mu(\omega)$, two additional ingredients are needed. The first is scale locality of the coupling kernel. The second is a turbulence spectral closure at the selected scales.

175 Expressing the force autocorrelation in wavenumber space converts the Green-Kubo integral into a weighted sum over the turbulent energy spectrum (SI S3A-C):

$$\Gamma(k) \propto \int_0^\infty E_u(q) q \mathcal{W}\left(\frac{q}{k}\right) dq, \quad (3)$$

178 where q is the eddy wavenumber and $\mathcal{W}(q/k)$ a dimensionless kernel encoding how efficiently a swell mode at wavenumber k couples to an eddy at wavenumber q . The kernel is structurally constrained by wave-eddy geometry. For $q/k \ll 1$, Galilean invariance and action conservation force $\mathcal{W} \propto (q/k)^2$. For $q/k \gg 1$, the finite orbital penetration depth suppresses coupling at least as fast as $(q/k)^{-1}$ (SI S3F, S5B).

186 Scale locality is not assumed but computed. Three independent filters suppress the integrand at both extremes. Large eddies ($q \ll k$) produce nearly uniform vorticity across the orbital excursion, reducing the interaction to reversible refraction[28]. Small eddies ($q \gg k$) are confined shallower than the orbital layer, suppressing the depth-overlap integral[29]. Kolmogorov weighting concentrates energy at intermediate scales. Figure 2 confirms that eddies with $0.5k \lesssim q \lesssim 2k$ account for 60-70% of the total attenuation. The closure is therefore needed only at the swell-selected scales, not across the entire mixed-layer spectrum.

198 At these scales, the group speed far exceeds mixed-layer turbulent velocities, so the force decorrelates by advective sweeping ($\tau_{\text{eff}} \sim (qc_g)^{-1}$) rather than eddy

turnover (Extended Data Figure 1, Figure 1d). Substituting the Kolmogorov spectrum $E_u(q) = C_K \varepsilon_{\text{eff}}^{2/3} q^{-5/3}$ and the sweep-dominated decorrelation time, performing the angular reduction and converting to a spatial decay rate via deep-water kinematics yields

$$\mu(\omega) = C_{\text{tot}} \varepsilon_{\text{eff}}^{2/3} g^{-7/3} \omega^{8/3}, \quad (4)$$

where ε_{eff} is an effective dissipation rate weighted by the orbital energy profile (Methods) and $C_{\text{tot}} = 2\pi/3 \approx 2.09$ collects five independently constrained factors, none fitted to wave data ($C_{\text{tot}} \in [1.10, 3.34]$, SI S5). The exponent is robust once the kernel is local in scale. The Kolmogorov spectrum contributes $q^{-5/3}$, the vorticity vertex q^{+2} , and sweep decorrelation q^{-1} . Uncertainty in the physics affects only the prefactor. Equation (4) is therefore a closed-form remote-swell law. The non-negativity $\Gamma \geq 0$ is broader (it holds for any stationary bath), whereas the factorised prefactor and the $\omega^{8/3}$ scaling require the turbulence spectral closure and the remote-swell decoupling conditions (SI S9). The Kolmogorov closure is needed only at $q \sim k \approx 0.01$ – 0.03 rad m^{-1} (inverse wavenumbers $q^{-1} \approx 30$ – 80 m) where the local Ozmidov scale exceeds the orbital penetration depth and the flow is locally isotropic [30, 31] (SI S5 F). Near-surface breaking eddies are spectrally filtered by the coupling window and do not bias the estimate (Extended Data Figure 2).

From local damping to observables

The scaling law (4) governs the ensemble-mean energy decay rate μ_E at each point along a swell trajectory. Satellite altimeters measure something different. The finite-length log-energy slope $\hat{\mu}_i \equiv -L_i^{-1} \ln[E(L_i)/E(0)]$ along a track of length L_i (SI S6). Because the SVF enters the energy equation multiplicatively ($dE_w \propto E_w dW$, Methods, equations (20)–(21)), passing from energy to log-energy generates an Itô drift. The log-slope estimator $\hat{\mu}$ tracks the geometric mean of the energy ratio, not the arithmetic mean. In the near-independent-encounter limit and at leading order in δ , this fixes three structural relations (Methods, SI S6 A–B): $\langle \hat{\mu} \rangle = 2\mu_E$, $\text{Var}(\hat{\mu}) = 2\mu_E/L$, $c_0 = \text{Var}(\hat{\mu})L/\langle \hat{\mu} \rangle = 1$. Half of the observable log-slope comes from the physical damping Γ and half from the noise-induced geometric drift. The same force autocorrelation that fixes the mean also fixes the baseline single-track variance.

When the turbulent environment varies along a propagation path, the predicted observable mean for track i becomes the path-averaged rate

$$\mu_{\text{model},i} = \frac{1}{L_i} \int_0^{L_i} \left[2\mu_E(\omega_i; \varepsilon_{\text{eff}}(s)) + \mu_v^{\text{Dore}}(\omega_i) \right] ds. \quad (5)$$

Under the central-limit approximation ($N \sim 10^5$ near-independent encounters per track), the finite-length estimator is

$$\hat{\mu}_i \sim \mathcal{N}\left(\mu_{\text{model},i}, c_0 \frac{\mu_{\text{svf},i}}{L_i} + \sigma_{\text{meas}}^2\right), \quad (6)$$

where $\mu_{\text{svf}} = 2\mu_E$ is the SVF observable contribution (including the Itô factor), $\mu_{\text{model}} = \mu_{\text{svf}} + \mu_v^{\text{Dore}}$, and only the SVF component enters the intrinsic variance because the Dore channel is deterministic. Weak along-ray correlations renormalise the second moment but not the first, replacing c_0 by \mathcal{R} (Methods, SI S6 E). The signal-to-noise ratio $\mathcal{S} = \mu_{\text{model}}/\sigma_{\text{tot}} \sim \mathcal{O}(1)$ for typical trans-oceanic paths (Extended Data Figure 5), so the framework predicts a substantial fraction of negative single-track estimates: $P(\hat{\mu}_i < 0) = \Phi(-\mathcal{S}_i)$. Writing $\beta = C_{\text{tot}}/(2\pi/3)$, the zero-parameter prediction is $\beta = 1$. The pathwise variance has a leading-order structural baseline $c_0 = 1$. Along-ray correlations and environmental-input limitations renormalise c_0 in practice, making the second-moment prediction a closure test rather than a strict zero-parameter claim. Figure 4 tests the first moment. Figure 5 tests the second.

Ensemble-mean predictions

Given wind forcing and mixed-layer structure from reanalysis, the scaling law (4) predicts the ensemble-mean energy attenuation rate μ_E at every ocean point, before examining a single wave observation. The prediction depends on turbulence sustained predominantly by the local wind along the propagation path, not on the swell itself. Figure 3a maps this prediction for 14 s swell. Because $\mathcal{S} \sim \mathcal{O}(1)$ (equation (6)), no single satellite track measures μ_E directly. The median e -folding length exceeds 10,000 km (Figure 3d): long-period swell routinely crosses an entire ocean basin before decaying by a factor e .

We compare these predictions with 241 trans-oceanic swell events tracked by satellite altimetry [4, 32] (Methods). For each track, ε_{eff} is evaluated along the great-circle ray using concurrent wind and mixed-layer data [33–35]. The prefactor C_{tot} was fixed from turbulence physics before any altimeter case was examined. The global maps (Figure 4a,b) show the same spatial organisation, with elevated attenuation near storm centres and low-attenuation corridors through subtropical gyres. The observed and predicted distributions both peak near 10^{-7} m^{-1} . A paired Wilcoxon signed-rank test yields $p = 0.816$, providing no evidence for systematic bias.

The predicted magnitude falls within the empirical corridor of existing swell-dissipation coefficients [19, 20, 36], but the functional forms differ. The empirical source term predicts $\mu \propto H_s^2$, whereas the Green-Kubo coefficient Γ is independent of wave energy (equation (2)). Satellite data strongly favour amplitude independence ($r = 0.00$, $p = 0.98$ across 241 tracks, Extended Data Figure 3, SI S8), suggesting that the empirical coefficient captures the correct turbulence-set magnitude through a different partitioning of the dependence on wave amplitude and environmental forcing.

The theory predicts that roughly one in four trans-oceanic swell tracks should show apparent *energy gain*. The ensemble mean always decays, but a single satellite pass samples only $N \sim 10^4$ - 10^5 near-independent wave-eddy encounters, too few for the stochastic drift to dominate the fluctuations. The Green-Kubo framework predicts the negative fraction quantitatively. At $c_0 = 1$, $P(\hat{\mu} < 0) = \Phi(-S)$, yielding 13-27% depending on wave period and path length (verified by Monte Carlo simulation, SI S6). The observed fraction across 241 tracks is 26%.

The sharpest test is whether the theory predicts the correct fraction of negative estimates for each track individually. The intrinsic variance $c_0 \mu_{svf,i}/L_i$ is not a free parameter. The fluctuation-dissipation relation locks it to the same Green-Kubo kernel that fixes the mean drift (equation (6)). The probability of a negative estimate, $P(\hat{\mu}_i < 0) = \Phi(-S_{tot,i})$, therefore depends only on quantities already determined by the first prediction line.

Figure 5b shows the observed negative fraction binned by path length against the per-bin predictions. The agreement is quantitative. As path length increases and S grows, the negative fraction falls. Figure 5c repeats the test binned by wave frequency. Because $\mu \propto \omega^{8/3}$, higher frequencies have larger S and therefore smaller negative fractions. This frequency dependence is an unambiguous signature of the $\omega^{8/3}$ scaling law, now tested through the distribution rather than the mean, providing a wholly independent verification.

Figure 5d shows the profile log-likelihood for a multiplicative scaling factor $\beta = C_{tot}/(2\pi/3)$, profiled over c_0 . The zero-parameter prediction $\beta = 1$ ($C_{tot} = 2\pi/3$) falls within both the statistical 95% CI and the theoretical C_{tot} range [1.10, 3.34] (SI S5). Including the laminar viscous contribution (~ 12 - 17% of the total, Figure 5f) shifts β_{MLE} closer to unity. This result is robust. Jointly profiling over c_0 and σ_{meas} keeps $\beta = 1$ within the C_{tot} range (Extended Data Figure 8b). The ensemble-mean magnitude requires no rescaling. A fixed-design Monte Carlo at $(\beta, c_0) = (1, 1)$ recovers both parameters without bias and achieves nominal coverage (Extended Data Figure 4).

Here and throughout, “zero-parameter” refers to the first-moment prediction $\beta = 1$; the second moment has a structural baseline $c_0 = 1$ but is a closure-level prediction that can be renormalised by correlations and non-intrinsic noise.

The intrinsic-variance coefficient c_0 and the non-intrinsic σ_{meas}^2 are partially degenerate, trading off along a likelihood ridge (Extended Data Figure 8a). At the adopted observational lower bound $\sigma_{meas} = 0.63 \times 10^{-7} \text{ m}^{-1}$, $c_{0,MLE} \approx 0.78$. A data-driven $\sigma_{meas} \approx 1.2 \times 10^{-7} \text{ m}^{-1}$ yields a correspondingly smaller c_0 (Extended Data Figure 8c). The reported $c_{0,MLE}$ is therefore an effective value that absorbs residual prediction error in ε_{eff} . The true intrinsic c_0 may be lower.

The attenuation budget (Figure 5f) comprises the

SVF contribution $2\mu_E$ (dominant) and the laminar air-viscous rate [13] μ_v , whose fraction declines from $\sim 21\%$ at $T \approx 12$ - 13 s to $\sim 13\%$ at $T \approx 16$ - 18 s, reflecting the steeper $\omega^{7/2}$ viscous scaling relative to the $\omega^{8/3}$ SVF law.

In total, a single theory governed by $\delta = u'/c_g$ passes five independent tests across the 241-track dataset, ensemble-mean magnitude, global spatial pattern, negative fraction versus path length, negative fraction versus frequency, and predictive coverage. The data are consistent with $\beta = 1$ across the entire plausible range of σ_{meas} (Extended Data Figure 8c). The pathwise distribution has a structural baseline $c_0 = 1$. The data favour a lower effective value, but the second-moment test is more sensitive than the first to environmental-input quality along individual tracks. The negative attenuation estimates that previous studies discarded are not artefacts of satellite retrieval but the stochastic theory’s most discriminating prediction, analogous to the backward displacements in Brownian motion that confirmed the existence of molecular collisions long before individual molecules could be observed.

DISCUSSION

The central advance of this work is the identification of the stochastic vortex force $\mathbf{f}_{svf} = \mathbf{u}_\phi \times \boldsymbol{\omega}'$ as a mechanism by which the Navier-Stokes equations produce irreversible non-breaking surface wave decay. This term is present in the exact vortex force but vanishes under phase averaging, which is why it does not appear in the classical phase-averaged description of wave-current interaction. Its autocorrelation, not its mean, controls the energy transfer. Once the problem is posed at this level, non-breaking swell dissipation becomes a dissipation problem with a Green-Kubo coefficient rather than an empirical source term. The same framework predicts that a substantial fraction of individual satellite tracks must show apparent energy gain, turning what was previously treated as retrieval noise into the theory’s most discriminating observational signature.

This reframing identifies a distinct non-breaking pathway by which surface-wave energy is transferred into upper-ocean turbulence below the breaking layer. Because the coupling is weighted by the orbital structure, the energy is deposited at depths of order $O(1/k) \sim 30$ - 80 m, well below the breaking injection layer, making the mechanism relevant to mixed-layer energetics and wave-supported turbulence. A physically based representation of this pathway is currently absent from most ocean-mixing formulations [37, 38], and the scaling law derived here offers a first-principles constraint for non-breaking wave-induced vertical mixing parameterisations [38, 39]. The Green-Kubo rate also provides a physically grounded alternative to empirical swell-dissipation source terms [12, 19]. The Itô correction changes how the existing observational record should be interpreted. The relation $\langle \hat{\mu} \rangle = 2\mu_E$ does not imply that half the attenuation is spurious. It means that trackwise log-slope estimates combine physical damping with a noise-induced

420 logarithmic drift, so historical swell-decay rates should
421 not be mapped one-to-one onto the physical energy-loss
422 rate without accounting for this stochastic correction.

423 The broader implication extends beyond swell. The
424 stochastic vortex-force coupling is not peculiar to this
425 system. What is special about remote swell is that it
426 isolates the mechanism cleanly enough for direct obser-
427 vational test. More generally, the result illustrates a
428 principle familiar in statistical mechanics but still un-
429 derused in geophysical fluid dynamics. Fluctuations
430 removed by deterministic averaging can control macro-
431 scopic dissipation through their two-time correlations.
432 Remote swell is therefore a natural geophysical analogue
433 of passive microrheology[40, 41], a weak probe whose
434 stochastic response reveals dissipation properties of the
435 surrounding turbulent bath.

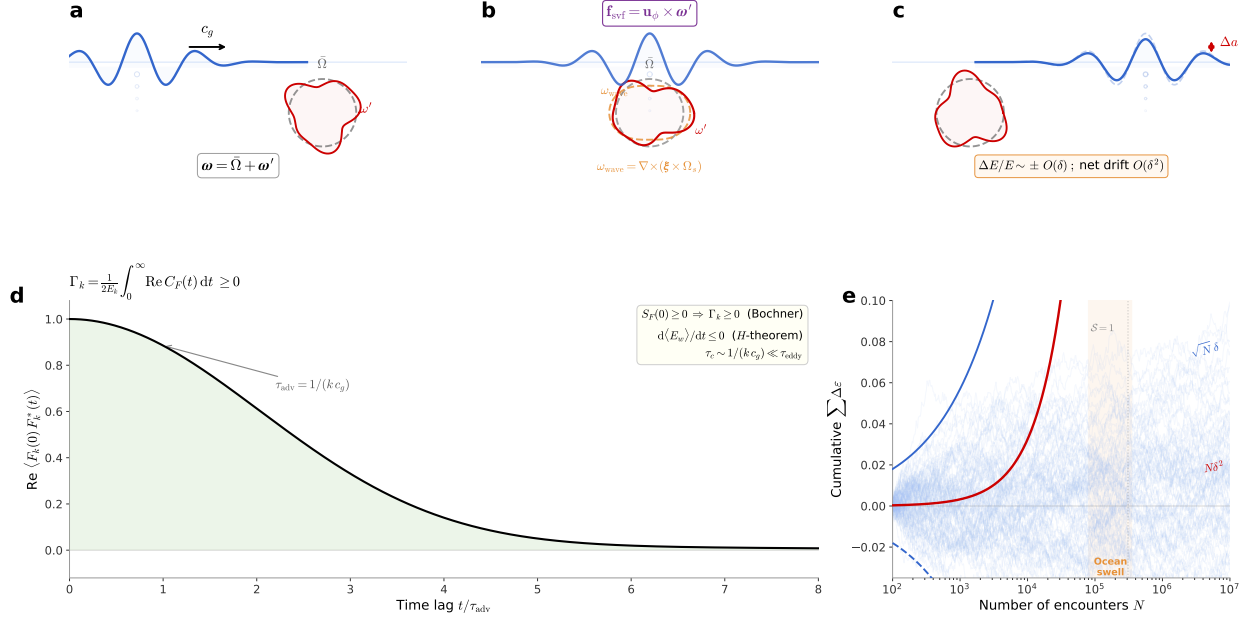


FIG. 1. The stochastic vortex force and the Green-Kubo route to irreversible swell dissipation. **a**, A swell packet propagates at group speed c_g toward a turbulent eddy. Before the encounter the vorticity has two components, the ensemble-mean $\bar{\Omega}$ (grey dashed) and the autonomous turbulent fluctuation ω' (red). The wave-slaved component ω_{wave} does not yet exist because it is created by the wave orbital motion. **b**, During the encounter. The wave-vorticity coupling generates a three-layer decomposition. $\bar{\Omega}$ (grey dashed), $\omega_{\text{wave}} = \nabla \times (\boldsymbol{\xi} \times \boldsymbol{\Omega}_s)$ (orange dashed, wave-slaved, no autonomous degrees of freedom), and ω' (red, autonomous). The mean-vorticity layer has zero phase average. The wave-slaved layer rectifies into the Craik-Leibovich vortex force, a zero-frequency quantity that does not project onto the wave mode at ω and therefore cannot enter its Green-Kubo friction coefficient. The third layer defines the stochastic vortex force $\mathbf{f}_{\text{svf}} = \mathbf{u}_\phi \times \boldsymbol{\omega}'$ (purple arrows). Its phase average vanishes, yet its nonzero autocorrelation is the only retained source of irreversible swell decay within the non-breaking, bulk-turbulence framework. **c**, After the encounter. The packet departs with a random energy increment $\Delta E/E \sim \pm O(\delta)$ whose sign depends on the instantaneous realisation of $\boldsymbol{\omega}'$. The dashed envelope marks the original amplitude. Irreversibility enters at $O(\delta^2)$ because the autonomous evolution of $\boldsymbol{\omega}'$ breaks the symmetry, and spatial separation at c_g permanently locks the energy transfer. **d**, Normalised SVF force autocorrelation $\text{Re} \langle F_k(0) F_k^*(t) \rangle$, computed from the spectral overlap integral (SI S3). After projection onto the resolved mode, the carrier-wave phase cancels in the conjugate product $F_k F_k^*$, so the residual decorrelation is controlled primarily by advective sweeping at c_g , with $\tau_{\text{adv}} \sim 1/(k c_g) \ll \tau_{\text{eddy}}$. The time integral is non-negative by Bochner's theorem. **e**, Cumulative log-energy change versus encounter number N for 100 Monte Carlo realisations (light blue). Mean drift (red) grows as $N\delta^2$ and fluctuations (blue envelope) grow as $\sqrt{N}\delta$. Signal-to-noise reaches unity at $N \sim 1/\delta^2$ (orange band), corresponding to a trans-oceanic path of $\sim 15,000$ km, so a finite fraction of tracks end with apparent energy gain.

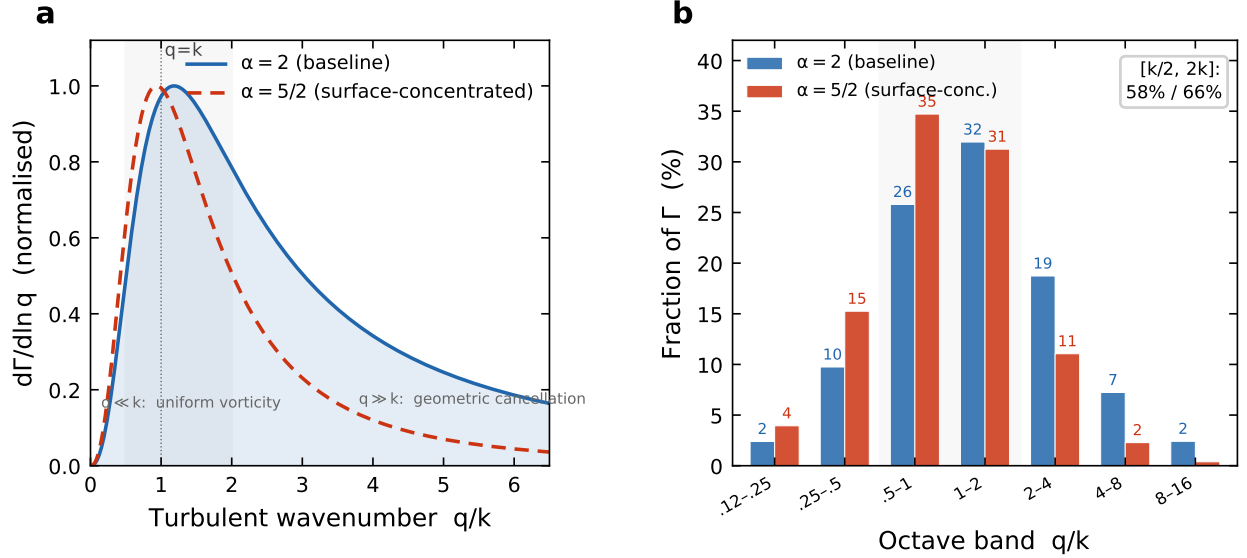


FIG. 2. Scale-selective coupling. **a**, Spectral contribution density $d\Gamma/d\ln q$ as a function of normalised turbulent wavenumber q/k , for two members of the parametric window family $\widehat{W}_\alpha(x) = x^2/(1+x^2)^\alpha$ (SI S5 B). The baseline model $\alpha = 2$ (blue solid, surface-injected turbulence with depth confinement $\chi_q \propto e^{-qz}$) and the surface-concentrated model $\alpha = 5/2$ (orange dashed, enhanced near-surface enstrophy). Three independent mechanisms suppress coupling away from $q \simeq k$. Large eddies ($q \ll k$) produce nearly uniform vorticity across the orbital excursion. Small eddies ($q \gg k$) cancel by geometric averaging within one orbital penetration depth. The Kolmogorov energy weighting concentrates the inertial-range spectrum at intermediate scales. All three select $q \simeq k$, confirming that the SVF coupling is local in scale. The shaded band marks the interval $[k/2, 2k]$. **b**, Fractional contribution to the total damping rate Γ from successive octave bands of q/k . For the baseline window ($\alpha = 2$), eddies with $k/2 \leq q \leq 2k$ account for 58% of the total. For the surface-concentrated window ($\alpha = 5/2$), the same band captures 66%. This scale locality is what allows the Kolmogorov $-5/3$ spectrum, evaluated at the single scale $q \simeq k$, to fix the $\omega^{8/3}$ exponent without free-parameter fitting. Uncertainty in the enstrophy depth profile affects only the prefactor C_{tot} (SI S5, SI Table S1).

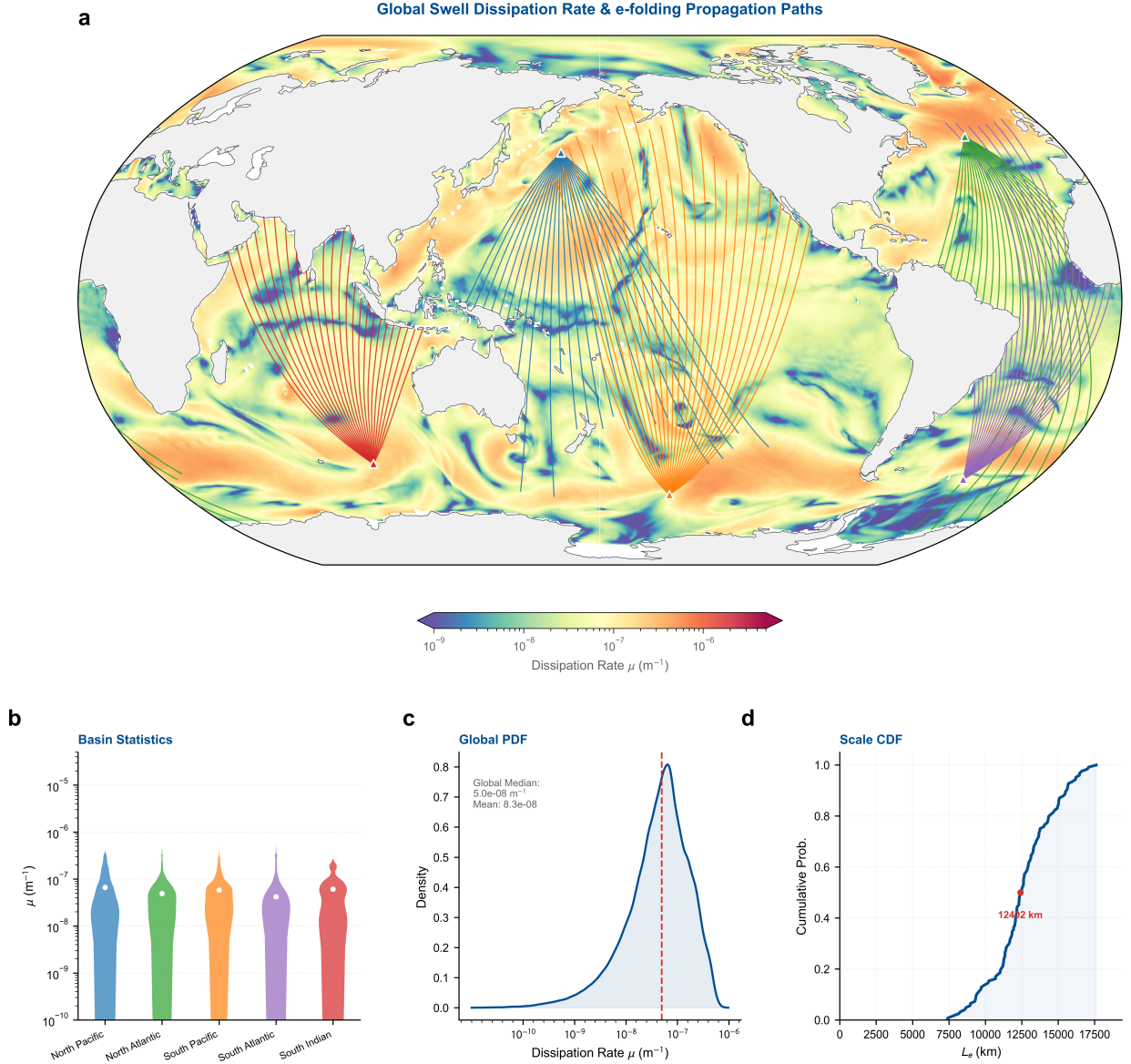


FIG. 3. Ensemble-mean swell dissipation predicted from the scaling law. All panels are computed from reanalysis environmental fields and the analytical law $\mu_E = C_{\text{tot}} \varepsilon_{\text{eff}}^{2/3} g^{-7/3} \omega^{8/3}$ with $C_{\text{tot}} = 2\pi/3$. **a**, Physical attenuation rate μ_E for $T = 14$ s swell ($k \approx 0.02 \text{ rad m}^{-1}$) on 1 January 2005 (00:00 UTC). ε_{eff} is evaluated from ERA5 10-m wind speeds via the wall-law parameterisation (SI S5D) with mixed-layer depth from ECCO V4r4. Great-circle rays (25 per source) radiate from five storm-generation zones (triangles) and are truncated where the cumulative path integral $\int_0^L \mu_E ds$ reaches unity ($L_e = 1/\bar{\mu}_E$). **b**, Basin-resolved violin plots of along-ray μ_E sampled at 20 km intervals. White circles mark medians. Southern Ocean basins show systematically higher attenuation owing to stronger background winds. **c**, Global probability density of μ_E across all ocean grid points (kernel density estimate on $\log_{10} \mu_E$, approximately log-normal). Dashed red line marks the median, and the mean exceeds the median by a factor of ~ 1.5 due to the heavy upper tail in storm-track regions. **d**, Cumulative distribution of e -folding length L_e from each ray's path-averaged $\bar{\mu}_E$. Red dot marks the median (annotated). Swell at $T = 14$ s routinely crosses an entire ocean basin before losing a factor of e in energy, confirming that non-breaking turbulent dissipation acts as a slow but persistent drain over trans-oceanic distances.

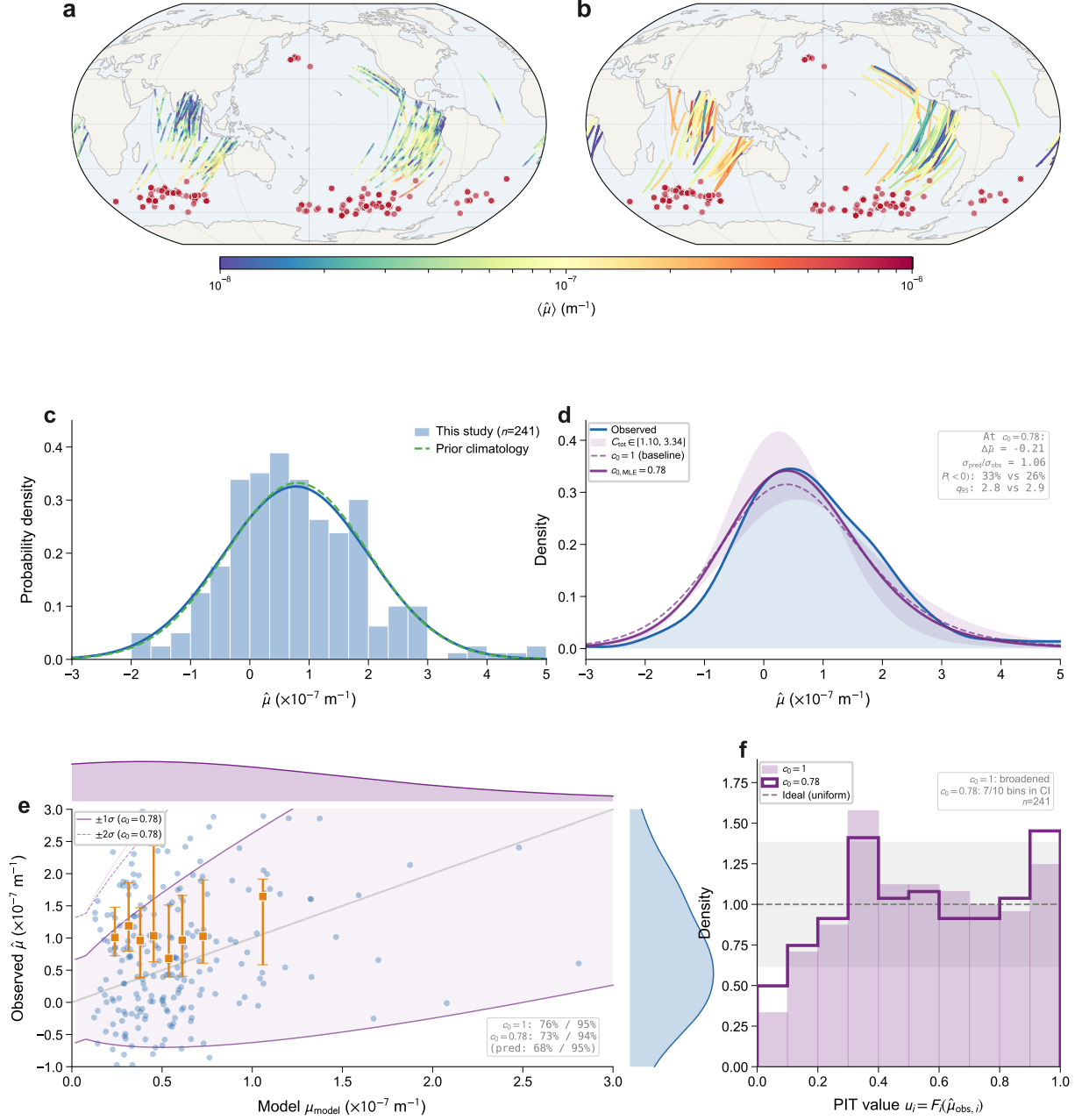


FIG. 4. Satellite validation of the universal swell attenuation law. The trackwise observable mean is $\mu_{\text{model},i} = 2\mu_{E,i}^{\text{SVF}} + \mu_{v,i}^{\text{Dore}}$, combining the SVF turbulent prediction with the laminar air-viscous rate [13]. The predictive variance uses only the SVF component, $\text{Var}_{\text{int}}(\hat{\mu}_i) = c_0 \cdot 2\mu_{E,i}^{\text{SVF}}/L_i$ (Dore is deterministic and does not contribute to intrinsic scatter). Panels d-f preview the distribution-level diagnostics developed fully in Figure 5. **a**, Model-predicted SVF attenuation rate along each observation segment, coloured by $2C_{\text{tot}}\varepsilon_{\text{eff}}^{2/3}g^{-7/3}\omega^{8/3}$, evaluated from CCMP V2.0 wind vectors and ECCO V4r4 mixed-layer depths. Red dots mark storm sources. **b**, Satellite-derived attenuation rate $\hat{\mu}$ for the same 241 events, computed from altimeter significant wave height by log-energy regression. Thin dark segments show the pre-observation propagation path. **c**, Probability density of observed $\hat{\mu}$ (histogram) compared with the climatological distribution from Jiang et al. [4] (dashed). **d**, Distribution-level comparison. Blue solid: observed KDE. Purple dashed: predicted mixture at the near-independent-encounter baseline $c_0 = 1$. Purple solid: $c_{0,\text{MLE}} = 0.78$. Shaded band spans the C_{tot} prefactor uncertainty [1.10, 3.34] (SI S5), applied to the SVF component only. Inset reports summary statistics at $c_0 = 0.78$, including bias $\Delta\bar{\mu}$, variance ratio $\sigma_{\text{pred}}/\sigma_{\text{obs}}$, negative fraction (predicted versus observed), and 95th percentile $q_{0.95}$. **e**, Trackwise scatter of observed $\hat{\mu}$ against μ_{model} . Grey diagonal: $y = x$. Purple curves mark the $\pm 1\sigma$ and $\pm 2\sigma$ prediction envelopes at $c_{0,\text{MLE}} = 0.78$ (representative envelope at median L and μ_v^{Dore}). Gold squares: binned medians with interquartile ranges. Inset reports $1\sigma/2\sigma$ coverage fractions for $c_0 = 1$ and $c_0 = 0.78$ (Gaussian expectation, 68%/95%). **f**, Probability Integral Transform (PIT) histogram. Under a well-calibrated predictive distribution, $u_i = F_i(\hat{\mu}_{\text{obs},i})$ should be uniform (dashed line). Light shading: $c_0 = 1$. Purple outline: $c_0 = 0.78$.

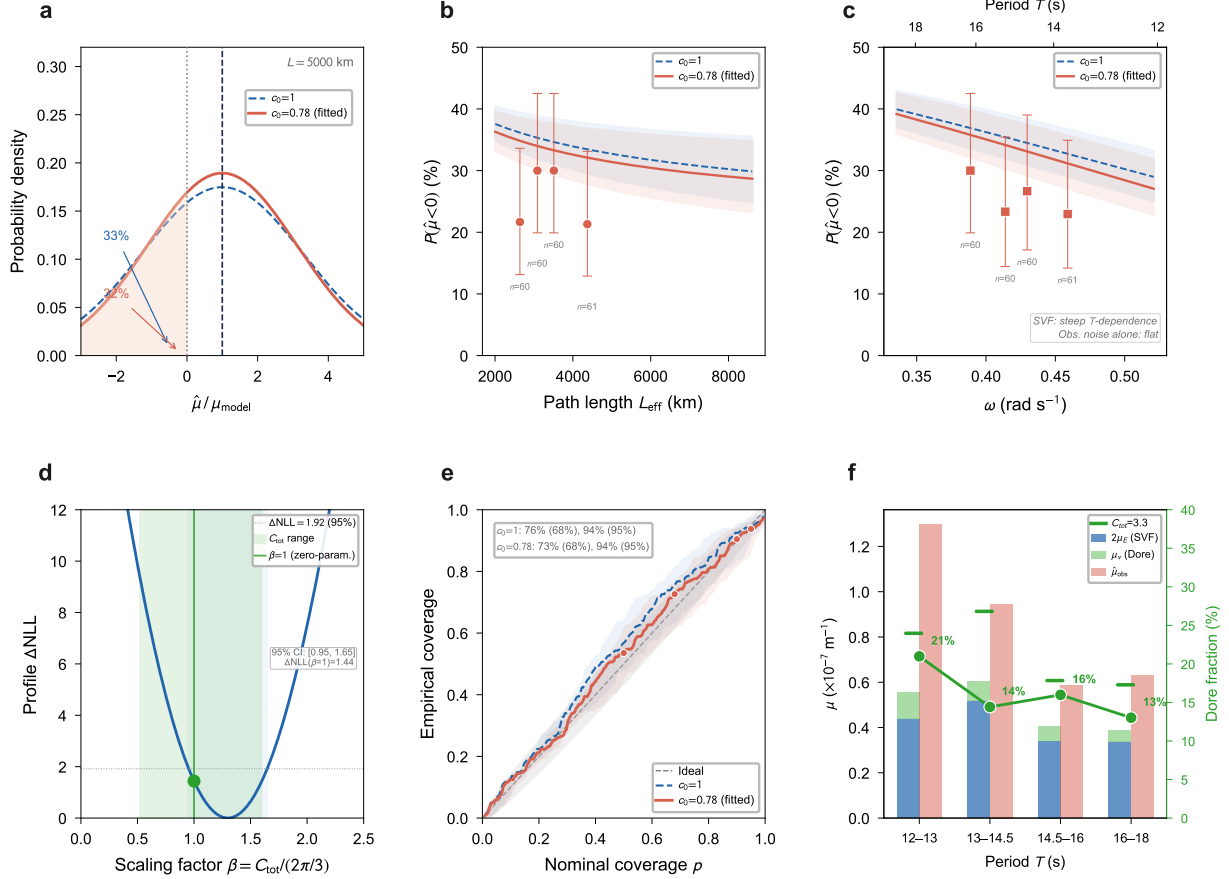


FIG. 5. Distribution-level validation and attenuation budget across swell events. The predictive distribution for each track is $\hat{\mu}_i \sim \mathcal{N}(\mu_{\text{model},i}, c_0 \mu_{\text{svf},i}/L_i + \sigma_{\text{meas}}^2)$, where $\mu_{\text{model},i} = \mu_{\text{svf},i} + \mu_{v,i}^{\text{Dore}}$ and $\mu_{\text{svf}} = 2\mu_E$. The intrinsic variance uses only the SVF component (Dore is deterministic). Two closures are compared, the near-independent-encounter baseline $c_0 = 1$ (blue dashed) and $c_{0,\text{MLE}} = 0.78$ (red solid). Shaded bands in panels b, c span the C_{tot} uncertainty [1.10, 3.34] (SI S5). **a**, Predicted single-path distribution of $\hat{\mu}/\mu_{\text{model}}$ at $L = 5,000$ km for both c_0 values. Shaded regions mark the negative-attenuation tail. **b**, Observed negative fraction versus effective path length L_{eff} (circles with Wilson 95% intervals), compared with predictions for both c_0 values. **c**, Same comparison versus peak swell frequency ω (top axis: period T). The steep frequency dependence is a discriminating signature of the $\omega^{8/3}$ law. Measurement noise alone would produce a flat curve. **d**, Profile negative log-likelihood for $\beta = C_{\text{tot}}/(2\pi/3)$, marginalised over c_0 . Blue shading: 95% CI [0.95, 1.64]. Green band: theoretical C_{tot} range (SI S5). The zero-parameter prediction $\beta = 1$ lies within both. **e**, Reliability diagram: empirical coverage versus nominal coverage p . Grey band: binomial 95% envelope. $c_0 = 1$: 76%/94% at the 68%/95% levels. $c_0 = 0.78$: 73%/94% (68%/95%). **f**, Attenuation budget by period bin (left axis) and laminar fraction (right axis, green). Blue bars: SVF contribution $2\mu_E$. Green bars: laminar viscous [13]. Pink bars: observed median $\hat{\mu}$. Horizontal green ticks: SVF+Dore at the upper C_{tot} bound (3.34), covering the observed medians in all bins. Green circles (right axis): Dore fraction, declining from $\sim 21\%$ at $T \approx 12$ s to $\sim 13\%$ at $T \approx 18$ s.

436

METHODS

437

Assumptions and projection framework

438 The derivation requires six assumptions (full dis-
 439 cussion in SI S2 A): **A1** (Resolved wave band). A
 440 narrow swell band \mathcal{B} admits a linear dispersion rela-
 441 tion. Nonlinear wave-wave transfer is negligible on the
 442 attenuation time scale. **A2** (Time-scale separation).
 443 $\tau_c \sim (k c_g)^{-1} \sim \mathcal{O}(1\text{-}5\text{ s}) \ll \Gamma^{-1} \sim 10^5\text{-}10^6\text{ s}$. The mar-
 444 gin is $\tau_c/\Gamma^{-1} \sim \delta^2 \sim 10^{-6}\text{-}10^{-4}$. **A3** (Bath statistics
 445 and phase decoupling). ω' is locally stationary and ho-
 446 mogeneous, statistically independent of the swell phase,
 447 with zero ensemble mean $\langle \omega' \rangle = \mathbf{0}$. The swell band
 448 contributes $\lesssim \mathcal{O}(10\%)$ of the total near-surface Stokes
 449 drift[37, 42], and the observed amplitude-independence
 450 of attenuation rates[14, 20] confirms the decoupling em-
 451 pirically. **A4** (Linear truncation). Feedback of order
 452 $|a_{\mathbf{k}}|^2$ on the bath is negligible. **A5** (Stationary reference
 453 measure). $\rho_{\text{ss}} \approx \rho_{\text{wave}} \times \rho_{\text{bath}}$. No equilibrium, detailed
 454 balance, or Boltzmann form is imposed. **A6** (Finite
 455 memory / mixing). The mode-projected SVF has an
 456 absolutely integrable autocorrelation.
 457 The Mori-Zwanzig inner product is $\langle A, B \rangle_\rho =$
 458 $\int A B^* \rho_{\text{ss}} d\mathbf{X}$, and the projector \mathcal{P} onto the swell sub-
 459 space is $\mathcal{P}A = \sum_{\mathbf{k} \in \mathcal{B}} \langle A, a_{\mathbf{k}} \rangle_\rho a_{\mathbf{k}} / \langle a_{\mathbf{k}}, a_{\mathbf{k}} \rangle_\rho$ (SI S2 B).
 460 The resulting generalised Langevin equation is

$$\dot{a}_{\mathbf{k}} = i\omega_{\mathbf{k}} a_{\mathbf{k}} - \int_0^t K_{\mathbf{k}}(t-s) a_{\mathbf{k}}(s) ds + F_{\mathbf{k}}(t), \quad (7)$$

461 where $K_{\mathbf{k}}(\tau)$ is a memory kernel and $F_{\mathbf{k}}(t)$ is the fluctu-
 462 ating force propagated within the orthogonal ($\mathcal{Q} = 1 - \mathcal{P}$)
 463 subspace. Under A2-A5, $F_{\mathbf{k}}$ reduces to the mode pro-
 464 jection of the physical SVF:

$$F_{\mathbf{k}}(t) = \int d^3\mathbf{x} \psi_{\mathbf{k}}^*(\mathbf{x}) \cdot (\mathbf{u}_\phi \times \omega')(\mathbf{x}, t), \quad (8)$$

465 where $\psi_{\mathbf{k}}$ is the linear velocity eigenfunction of mode \mathbf{k} ,
 466 with the normalisation convention $E_{\mathbf{k}} = \frac{1}{2}|a_{\mathbf{k}}|^2$ (SI S2 A).
 467 This identification is physical (a consequence of scale sep-
 468 aration and statistical independence), not an algebraic
 469 identity of the projector. The discarded contributions
 470 are absorbed into the streaming term and into reactive
 471 forces whose net work on the swell mode vanishes.

472 The second fluctuation-dissipation relation (FDR-
 473 II)[8, 23] is

$$K_{\mathbf{k}}(\tau) = \frac{\langle F_{\mathbf{k}}(0) F_{\mathbf{k}}^*(\tau) \rangle}{\langle |a_{\mathbf{k}}|^2 \rangle_{\text{ref}}}. \quad (9)$$

474 This is an algebraic consequence of the projection
 475 operators and holds for any stationary ρ_{ss} . No de-
 476 tailed balance, time reversal, or equilibrium structure is
 477 required[43, 44]. The force autocorrelation factorises as
 478 $\langle F_{\mathbf{k}}(0) F_{\mathbf{k}}^*(\tau) \rangle = 2E_{\mathbf{k}} \mathcal{G}_{\mathbf{k}}(\tau)$ (SI S2 C), where $\mathcal{G}_{\mathbf{k}}$ depends
 479 only on bath statistics. This cancels the $E_{\mathbf{k}}$ in the de-
 480 nominator of equation (2), making Γ a material property
 481 of the bath independent of wave amplitude, analogous to
 482 the friction coefficient of a Brownian particle[45], which

483 depends on solvent viscosity but not on the particle's
 484 velocity. Under A2 the GLE reduces to the Markovian
 485 amplitude equation

$$\dot{a}_{\mathbf{k}} = i(\omega_{\mathbf{k}} + \Delta\omega_{\mathbf{k}}) a_{\mathbf{k}} - \Gamma(\mathbf{k}) a_{\mathbf{k}} + F_{\mathbf{k}}(t), \quad (10)$$

486 with $\Delta\omega_{\mathbf{k}} = \int_0^\infty \text{Im}[K_{\mathbf{k}}(\tau)] d\tau$ ($|\Delta\omega|/\omega \sim \delta^2 \sim 10^{-6}$ -
 487 10^{-4} , SI S2 G).

Non-negativity of the Green-Kubo damping rate

488 Because $F_{\mathbf{k}}(t)$ is a stationary process with finite
 489 variance (A3 i, A5 i, A6), its autocorrelation $C_F(\tau) =$
 490 $\langle F_{\mathbf{k}}(0) F_{\mathbf{k}}^*(\tau) \rangle$ is positive-definite in the sense of Bochner:

$$\sum_{j,\ell} \alpha_j \alpha_\ell^* C_F(t_j - t_\ell) \geq 0 \quad \text{for any finite set } \{t_j\}, \{\alpha_j\}. \quad (11)$$

492 Bochner's theorem[46] guarantees that the power spec-
 493 tral density $S_F(\nu) = \int_{-\infty}^\infty C_F(\tau) e^{i\nu\tau} d\tau \geq 0$ for all ν .
 494 The Hermitian symmetry $C_F(-\tau) = C_F(\tau)^*$ allows the
 495 half-line integral to be written as

$$\int_0^\infty \text{Re}[C_F(\tau)] d\tau = \frac{1}{2} S_F(0) \geq 0, \quad (12)$$

496 so that $\Gamma(\mathbf{k}) = S_F(0)/(4E_{\mathbf{k}}) \geq 0$. The proof chain is as
 497 follows. Stationarity \Rightarrow positive-definiteness $\Rightarrow S_F(\nu) \geq$
 498 $0 \Rightarrow S_F(0) \geq 0 \Rightarrow \Gamma \geq 0$. No assumption on the bath
 499 spectrum enters at any step. The result holds equally for
 500 Kolmogorov, viscous, or any intermediate regime, and for
 501 wind seas as well as swell (SI S2 F, Theorem 1). Equality
 502 ($\Gamma = 0$) requires the zero-frequency spectral density to
 503 vanish, $S_F(0) = 0$. A time-independent (frozen) bath is
 504 one sufficient condition. Irreversibility requires the eddy
 505 field to evolve during the encounter.

Spectral overlap and vertex

506 Fourier-expanding the SVF and evaluating the mode-
 507 projected force autocorrelation along the wave-energy
 508 trajectory $\mathbf{X}(t) = \mathbf{c}_g t$ yields (SI S3 A-D):

$$\Gamma(k) = \frac{1}{2E_{\mathbf{k}}} \int d^3q \int d\Omega S_u(q, \Omega) |V(\mathbf{q}; k)|^2 \mathcal{W}_\Omega(\Omega - \mathbf{q} \cdot \mathbf{c}_g), \quad (13)$$

510 where $S_u(q, \Omega)$ is the turbulent velocity spectrum, $|V|^2$
 511 the vortex-force vertex, and \mathcal{W}_Ω the temporal mem-
 512 ory window from the Green-Kubo time integral. For
 513 isotropic turbulence the angular integration over eddy
 514 orientations gives $\tilde{\mathcal{G}}_{\text{geom}} = 2/3$. Anisotropy extends this
 515 to $[2/3, 3/4]$ (SI S5 A).

Scale-selection window

516 The coupling kernel $\mathcal{W}(q/k)$ is suppressed at both
 517 extremes of the eddy spectrum (SI S3 F). At $q \ll k$,
 518 Galilean invariance ($q = 0$) and wave-action conservation
 519 (q/k first order) force the first irreversible contribution

521 to enter at $\mathcal{O}(q^2/k^2)$. At $q \gg k$, the depth-overlap
 522 integral between the wave orbital layer ($\sim k^{-1}$) and the
 523 eddy ($\sim q^{-1}$) suppresses coupling as q^{-1} or steeper. The
 524 effective vertex is

$$|V(\mathbf{q}; k)|_{\text{eff}}^2 = U_0^2 q^2 \tilde{G}_{\text{geom}} \mathcal{W}\left(\frac{q}{k}\right), \quad (14)$$

525 with the baseline analytical window $\widehat{W}(x) = x^2/(1 +$
 526 $x^2)^2$ for surface-injected turbulence. The one-parameter
 527 family $\widehat{W}_\alpha(x) = x^2/(1 + x^2)^\alpha$ spans $\alpha \in [3/2, 5/2]$. In
 528 all cases the contribution density peaks near $x \approx 1$,
 529 confirming scale locality $q \simeq k$ (SI S5 B).

530 Sweep dominance and closure

531 The four-dimensional spectrum factorises as
 532 $S_u(q, \Omega) = S_u(q) \chi(\Omega; q)$ with $\int \chi \, d\Omega = 1$, where
 533 χ has characteristic width $\omega_q \sim (\varepsilon q^2)^{1/3}$ (the eddy
 534 turnover frequency). Inserting this into equation (13)
 535 and performing the Ω -integral converts the temporal
 536 memory window into an effective correlation time
 537 $\tau_{\text{eff}}(q; k)$ (SI S3 E). For oceanic swell, $|\mathbf{q} \cdot \mathbf{c}_g| \tau_{\text{eddy}} \gg 1$
 538 at all relevant scales, so decorrelation is controlled by
 539 advective sweeping rather than eddy turnover:

$$\tau_{\text{eff}}(q; k) \simeq \frac{C_\tau}{q c_g(k)}, \quad (15)$$

540 with $C_\tau \in [0.89, 1.25]$ (Extended Data Figure 1, SI S5 C).
 541 The crossover wavenumber $q_* = \varepsilon/c_g^3$ lies far below the
 542 swell wavenumber k for $\varepsilon \lesssim 10^{-6} \text{ m}^2 \text{ s}^{-3}$. Hence the
 543 advective limit applies at all contributing eddy scales.

544 Combining the angular integral, scale-selection win-
 545 dow, advective correlation time, and depth-projection
 546 factor $C_E = 1$ (SI S3 F), the one-dimensional Green-
 547 Kubo form is

$$\Gamma(k) \simeq \frac{C_\tau \tilde{G}_{\text{geom}} U_0^2}{2 E_k c_g(k)} \int_0^\infty dq E_u(q) q \mathcal{W}\left(\frac{q}{k}\right). \quad (16)$$

548 Kolmogorov closure

549 With the Kolmogorov spectrum

$$E_u(q) = C_K \varepsilon_{\text{eff}}^{2/3} q^{-5/3}, \quad (17)$$

550 ($C_K \approx 1.5 \pm 0.1$ [47, 48]), the integrand of equation (16)
 551 carries a definite power of q from each factor. $q^{-5/3}$
 552 from the one-dimensional Kolmogorov spectrum $E_u(q)$,
 553 q^{+2} from the curl in the vorticity vertex (q^2 in $|V|^2$),
 554 q^{-1} from the sweep-dominated correlation time $\tau_{\text{eff}} \propto$
 555 $(qc_g)^{-1}$. The net integrand exponent is $-5/3 + 2 - 1 =$
 556 $-2/3$. Changing variables to $x = q/k$:

$$\int_0^\infty dq q^{-2/3} \mathcal{W}\left(\frac{q}{k}\right) = k^{1/3} \underbrace{\int_0^\infty x^{-2/3} \mathcal{W}(x) dx}_{C_S} \quad (18)$$

557 yielding $\Gamma(k) \propto k^{1/3}$. The spatial attenuation rate
 558 $\mu = 2\Gamma/c_g$ inherits factors of c_g^{-1} and U_0^2/E_k that

combine with the dispersion relation $k = \omega^2/g$ to give
 560 $\mu(\omega) \propto \omega^{8/3}$ (SI S4). The q^2 from the curl vertex and
 561 the q^{-1} from the advective decorrelation are the only
 562 factors that depend on the specific physical mechanism.
 563 The remaining powers are kinematic bookkeeping. The
 564 geometric vertex factor $\tilde{G}_{\text{geom}} = 2/3$ is q -independent
 565 and does not affect the exponent.

Environmental inputs and path integration

567 The effective dissipation rate $\varepsilon_{\text{eff}}(k)$ is the orbital-
 568 weighted depth average of $\varepsilon(z)$ below the breaking layer,
 569 evaluated under law-of-the-wall scaling (SI S5 D-E).
 570 Wind stress fields are from ERA5 reanalysis[49] (0.25°,
 571 6-hourly) for the global map (Figure 3) and CCMP V2.0
 572 satellite wind vectors[33, 34] (0.25°, 6-hourly) for the
 573 241-track validation (Figure 4). Mixed-layer depths are
 574 from ECCO V4r4[35] (0.5°, daily). Model predictions
 575 along each ray are computed by integrating $\mu(\omega; \varepsilon_{\text{eff}}(\mathbf{x}))$
 576 along the great-circle path using concurrent data. Storm
 577 sources are identified with a local minimum detection
 578 algorithm (1000 km exclusion radius, SI S5 E).

579 Comparing theory with satellite tracks requires one
 580 additional step. The theoretical quantity μ_E governs
 581 the decay of ensemble-mean energy. Satellite altimeters,
 582 however, return a finite-length regression estimator $\hat{\mu}_i$
 583 for each track. Its path-averaged expectation equals
 584 $2\mu_E$, the Itô correction associated with multiplicative
 585 noise (Methods). The model prediction for each track is
 586 equation (5), evaluated along the great-circle trajectory
 587 using concurrent environmental data.

Satellite data and validation

589 Observed attenuation rates follow the altimeter track-
 590 ing method[4]. Along-track H_s from Jason-2, Jason-3,
 591 and Sentinel-3A. Selection criteria: (i) $\lambda = 250$ -500 m,
 592 (ii) propagation distance > 2000 km, (iii) directional
 593 spread $< 30^\circ$, (iv) $H_{s,\text{swell}}/H_{s,\text{total}} > 0.7$. After qual-
 594 ity filtering, $N = 241$ cases remain (SI S7 A-B). The
 595 observed rate:

$$\ln H_s(s) = \ln H_{s,0} - \frac{1}{2} \mu_{\text{obs}} s. \quad (19)$$

596 Statistical diagnostics: PDFs of μ_{obs} and μ_{model} , paired
 597 Wilcoxon signed-rank test, log-ratio $\log_{10}(\mu_{\text{model}}/\mu_{\text{obs}})$,
 598 coverage diagrams. Frequency-scaling tests: $\log_{10} \mu$ ver-
 599 sus $\log_{10} \omega$ regression with bootstrap CIs. Variance bud-
 600 get and cross-dataset consistency checks are in SI S7 C-D.
 601 Uncertainty sources: altimeter noise ($\sim 5\%$ in H_s), storm-
 602 source localisation (~ 100 km), and along-track sampling
 603 gaps, propagated to case-by-case error estimates.

Observable bridge and Itô correction

605 The Markovian dynamics (10) imply that the band-
 606 integrated swell energy satisfies

$$\frac{dE_w}{dt} = -2\Gamma E_w + \tilde{\eta}(t), \quad (20)$$

607 with noise autocorrelation locked by FDR-II (equa-
608 tion 9):

$$\langle \tilde{\eta}(0) \tilde{\eta}(\tau) \rangle = \frac{2D_E}{\tau_c} g(\tau/\tau_c), \quad D_E = 4\Gamma E_w^2, \quad (21)$$

609 with g a normalised correlator ($\int_0^\infty g(s) ds = 1$, SI S6 A).
610 Because $D_E \propto E_w^2$, the noise is multiplicative. Passing
611 to $\ln E_w$ introduces an Itô correction. The derivation of
612 the pathwise distribution proceeds in four steps.

613 The instantaneous power delivered to the wave mode
614 is $\dot{W}_k = \text{Re}(a_k^* F_k)$ (SI S6 A). Its autocorrelation $C_{\dot{W}}(\tau)$
615 involves the product of two bilinear expressions in a_k
616 and F_k . Using the identity $\text{Re}(z_1)\text{Re}(z_2) = \frac{1}{2}\text{Re}(z_1 z_2^*) +$
617 $\frac{1}{2}\text{Re}(z_1 z_2)$ with $z_1 = a_k^* F_k(0)$, $z_2 = a_k^* F_k(\tau)$. The first
618 average gives $\langle z_1 z_2^* \rangle = 2E_k C_F(\tau)$ (since $|a_k|^2 = 2E_k$).
619 The anomalous correlator $\langle z_1 z_2 \rangle$ vanishes to leading or-
620 der by the properness of the narrow-band mode process
621 (equivalently, by translational invariance of the underly-
622 ing real homogeneous field, SI S6 A). Hence

$$C_{\dot{W}}(\tau) = E_k \text{Re} C_F(\tau). \quad (22)$$

623 The factor E_k in $C_{\dot{W}}$ relative to C_F is the structural
624 reason the variance coefficient is twice the drift coefficient
625 at encounter level, yielding $\beta_\xi = 2\alpha$ after FDR-II is
626 applied.

627 Over one advective correlation time $\tau_{\text{adv}} \sim \ell_c/c_g$, the
628 fractional energy change $\xi \equiv \Delta E/E$ has mean $\langle \xi \rangle =$
629 $-\alpha \delta^2$ with $\alpha = 2\Gamma\tau_{\text{adv}}/\delta^2$ (from the ensemble-mean
630 decay equation (20) and FDR-II), and variance $\text{Var}(\xi) =$
631 $\beta_\xi \delta^2$ with $\beta_\xi = 2\tau_{\text{adv}} I_F / (E_k \delta^2)$ (from equation (22)
632 integrated via the Green-Kubo approximation). The
633 FDR-II relation gives $I_F \equiv \int_0^\infty \text{Re} C_F d\tau = 2E_k \Gamma$ (from
634 $\Gamma = I_F / (2E_k)$, equation (2)). Substituting:

$$\beta_\xi = \frac{2\tau_{\text{adv}} \cdot 2E_k \Gamma}{E_k \delta^2} = \frac{4\Gamma\tau_{\text{adv}}}{\delta^2} = 2\alpha, \quad \text{hence} \quad \frac{\alpha}{\beta_\xi} = \frac{1}{2}. \quad (23)$$

635 This ratio is fixed by FDR-II and the bilinear coupling
636 structure. It is independent of δ , ℓ_c , the shape of $C_F(\tau)$,
637 and E_k (SI S6 A).

638 Expanding $\Delta \varepsilon \equiv \ln(1 + \xi) \approx \xi - \frac{1}{2}\xi^2 + \mathcal{O}(\delta^3)$ and
639 using $\langle \xi^2 \rangle = \text{Var}(\xi) + \langle \xi \rangle^2 = \beta_\xi \delta^2 + \mathcal{O}(\delta^4)$:

$$\begin{aligned} \langle \Delta \varepsilon \rangle &= -\alpha \delta^2 - \frac{1}{2}\beta_\xi \delta^2 \equiv -A \delta^2, \\ A &= \alpha + \frac{1}{2}\beta_\xi = \beta_\xi, \\ \text{Var}(\Delta \varepsilon) &= \beta_\xi \delta^2 \equiv B \delta^2. \end{aligned} \quad (24)$$

640 The $\frac{1}{2}\beta_\xi$ term in A is the Itô correction, the geometric
641 drift due to multiplicative noise, analogous to the $-\frac{1}{2}\sigma^2$
642 in geometric Brownian motion.

643 The ensemble-mean energy decay rate (from S3-S5) is
644 $\mu_E = \alpha \delta^2 / \ell_c$, while the satellite estimator mean is $\langle \hat{\mu} \rangle =$
645 $A \delta^2 / \ell_c = (A/\alpha) \mu_E = 2\mu_E$. The estimator variance is
646 $\text{Var}(\hat{\mu}) = B \delta^2 / (L \ell_c) = (B/\alpha) \mu_E / L = 2\mu_E / L$. Both δ
647 and ℓ_c cancel in these ratios. Here and throughout, “zero-
648 parameter refers to the first-moment prediction $\beta = 1$;
649 the second moment has a structural baseline $c_0 = 1$ but
650 is a closure-level prediction that can be renormalised by
651 correlations and non-intrinsic noise.

652 The intrinsic-variance coefficient is

$$\sigma_\mu^2 = c_0 \frac{\mu}{L}, \quad c_0 = \frac{B}{A} = \frac{\beta_\xi}{\beta_\xi} = 1. \quad (25)$$

653 No specific form for $C_F(\tau)$ has been assumed. No
654 thermal-equilibrium hypothesis enters. The relation
655 between drift and diffusion is inherited from FDR-II and
656 the multiplicative coupling structure (SI S6 B). By the
657 central limit theorem ($N \sim 10^5$ encounters, approximate
658 independence from A6):

$$\hat{\mu}_i \sim \mathcal{N}\left(2\mu_{E,i}, \underbrace{\frac{2\mu_{E,i}}{L_i}}_{\sigma_{\text{intr},i}^2} + \sigma_{\text{meas}}^2\right). \quad (26)$$

659 The factors 2 (mean) and 2 (variance) are exact at lead-
660 ing order in δ . The ratio $c_0 = 1$ is determined by the
661 universal structural ratio $\alpha/\beta_\xi = 1/2$. Because satellite
662 retrievals fit a multi-point ordinary least-squares (OLS)
663 regression rather than a two-endpoint difference, the
664 intrinsic variance acquires an estimator efficiency fac-
665 tor $f(M) = (6/5)(M^2 + 1)/[M(M + 1)]$, where M is
666 the number of effectively independent distance measure-
667 ments per event (typically 3-15). At these low M , $f(M)$
668 lies between 1.00 and 1.13 (SI S6). Physically significant
669 departures from $c_0 = 1$ arise from $\mathcal{O}(1)$ effects outside
670 the leading-order framework. Turbulence intermittency
671 (enhances variance, pushes c_0 above 1) and weak cross-
672 encounter correlations (pulls in the opposite direction).
673 The expected range is $c_0 \sim 0.5$ -2 (SI S6 B).

Negative-rate prediction

675 The probability of a negative single-track estimate is

$$\begin{aligned} P(\hat{\mu}_i < 0) &= \Phi(-\mathcal{S}_{\text{tot},i}), \\ \mathcal{S}_{\text{tot},i} &= \frac{\mu_{\text{model},i}}{\sqrt{c_0 \mu_{\text{svf},i} / L_i + \sigma_{\text{meas}}^2}}. \end{aligned} \quad (27)$$

676 where Φ is the standard normal CDF. The intrinsic
677 signal-to-noise ratio $\mathcal{S}_{\text{int}}(\omega) = \sqrt{2\mu_E L} \propto \omega^{4/3} \sqrt{L}$ in-
678 creases with both frequency and path length. Higher-
679 frequency swell and longer paths yield smaller negative
680 fractions. The frequency and path-length dependences
681 constitute two independent one-sided falsification tests
682 of the $\omega^{8/3}$ exponent through the distribution rather
683 than the mean.

684 To test whether any global rescaling is required, a
685 multiplicative factor β is applied to both the mean and
686 intrinsic variance:

$$\hat{\mu}_i \sim \mathcal{N}\left(2\beta \mu_{E,i}^{\text{SVF}} + \mu_{v,i}^{\text{Dore}}, c_0 \frac{2\beta \mu_{E,i}^{\text{SVF}}}{L_i} + \sigma_{\text{meas}}^2\right). \quad (28)$$

687 The Green-Kubo prediction corresponds to $\beta = 1$. The
688 profile log-likelihood is evaluated over the 241-track sam-
689 ple, profiling over c_0 to obtain the marginal β estimate
690 and vice versa. Model adequacy is assessed via a cover-
691 age (reliability) diagram and profile-likelihood confidence
692 intervals (Extended Data Figure 7). Standardised residu-
693 als $z_i = (\hat{\mu}_i - \mu_{\text{model},i})/\sigma_{\text{tot},i}$ test normality (SI S7 C-D).

694 The total variance of single-track estimates decom-

695 poses into three mutually independent channels:

$$\sigma_{\hat{\mu}}^2 = \underbrace{\frac{2\mu E}{L}}_{\text{intrinsic}} + \underbrace{\sigma_{\text{env}}^2}_{\text{environmental}} + \underbrace{\sigma_{\text{obs}}^2}_{\text{observational}}, \quad (29)$$

696 where the intrinsic term follows from equation (26).
 697 The environmental term captures variability of ε_{eff}
 698 along propagation paths (propagated through the scal-
 699 ing law on a logarithmic scale, SI S6 C). The obser-
 700 vational term collects altimetric noise, spectral par-
 701 titioning uncertainty, and regression error, estimated
 702 from the four independent error sources identified in
 703 the altimetric error analysis[4] (SI S7 C). In the predic-
 704 tive distribution (6), the environmental and observa-
 705 tional channels are absorbed into σ_{meas}^2 , which therefore
 706 represents the total non-intrinsic variance. We adopt
 707 $\sigma_{\text{meas}} = 0.63 \times 10^{-7} \text{ m}^{-1}$ as a lower bound reflecting
 708 observational errors alone. This maximises the variance
 709 attributable to the intrinsic channel and provides the
 710 most conservative test of $\beta = 1$. A joint profile likelihood
 711 over $(c_0, \sigma_{\text{meas}})$ at $\beta = 1$ yields a data-driven estimate
 712 $\sigma_{\text{meas}} \approx 1.2 \times 10^{-7} \text{ m}^{-1}$ (95% CI [1.00, 1.38], Extended
 713 Data Figure 8a,c), with the excess over the observa-
 714 tional baseline attributable to residual ε_{eff} prediction
 715 error. The first-moment prediction $\beta = 1$ is insensitive
 716 to this choice (Extended Data Figure 8b,c). Because
 717 all three physical channels are independent (microscopic
 718 encounters, synoptic weather variability, and instrument
 719 characteristics), the variances add in quadrature (Ex-
 720 tended Data Figure 6).

721

ACKNOWLEDGEMENTS

722 We thank Haoyu Jiang (Shenzhen University) for pro-
723 viding the reprocessed altimeter swell-tracking dataset[4]
724 used throughout this study. This work was supported
725 by Khalifa University of Science and Technology, Abu
726 Dhabi, UAE.

727

DATA AVAILABILITY

728 The satellite swell-tracking data used in this study
729 are derived from the reprocessed altimeter dataset[4].
730 ERA5 reanalysis fields are available from the Coperni-
731 cus Climate Data Store (cds.climate.copernicus.eu).
732 Cross-Calibrated Multi-Platform (CCMP) Ocean Sur-
733 face Wind Vector Analyses (V2.0) are available from
734 Remote Sensing Systems (www.remss.com). ECCO
735 V4r4 daily mixed-layer depth fields are available from
736 the NASA Physical Oceanography Distributed Active
737 Archive Center. Processed data supporting the findings
738 of this study are available from the corresponding author
739 upon reasonable request.

740

CODE AVAILABILITY

741 The code used for data processing, model evaluation,
742 and figure generation is available at [https://zenodo.](https://zenodo.org/records/19135704)
743 [org/records/19135704](https://zenodo.org/records/19135704).

744

AUTHOR CONTRIBUTIONS

745 G.L. conceived the theoretical framework, derived all
746 analytical results, performed the numerical and statis-
747 tical analyses, and wrote the manuscript. M.A. con-
748 tributed to data analysis and interpretation.

749

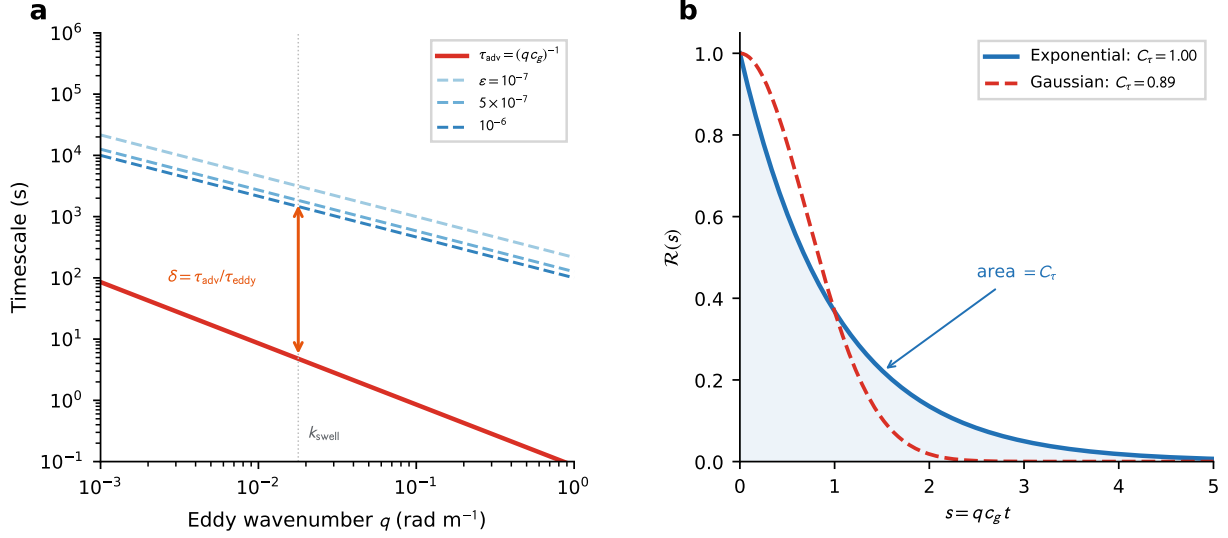
COMPETING INTERESTS

750 The authors declare no competing interests.

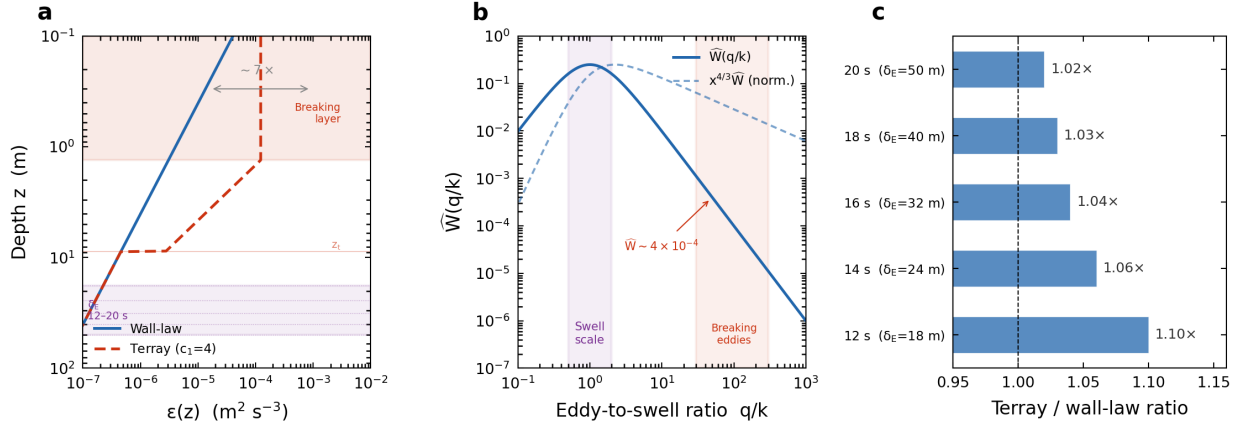
751

CORRESPONDENCE

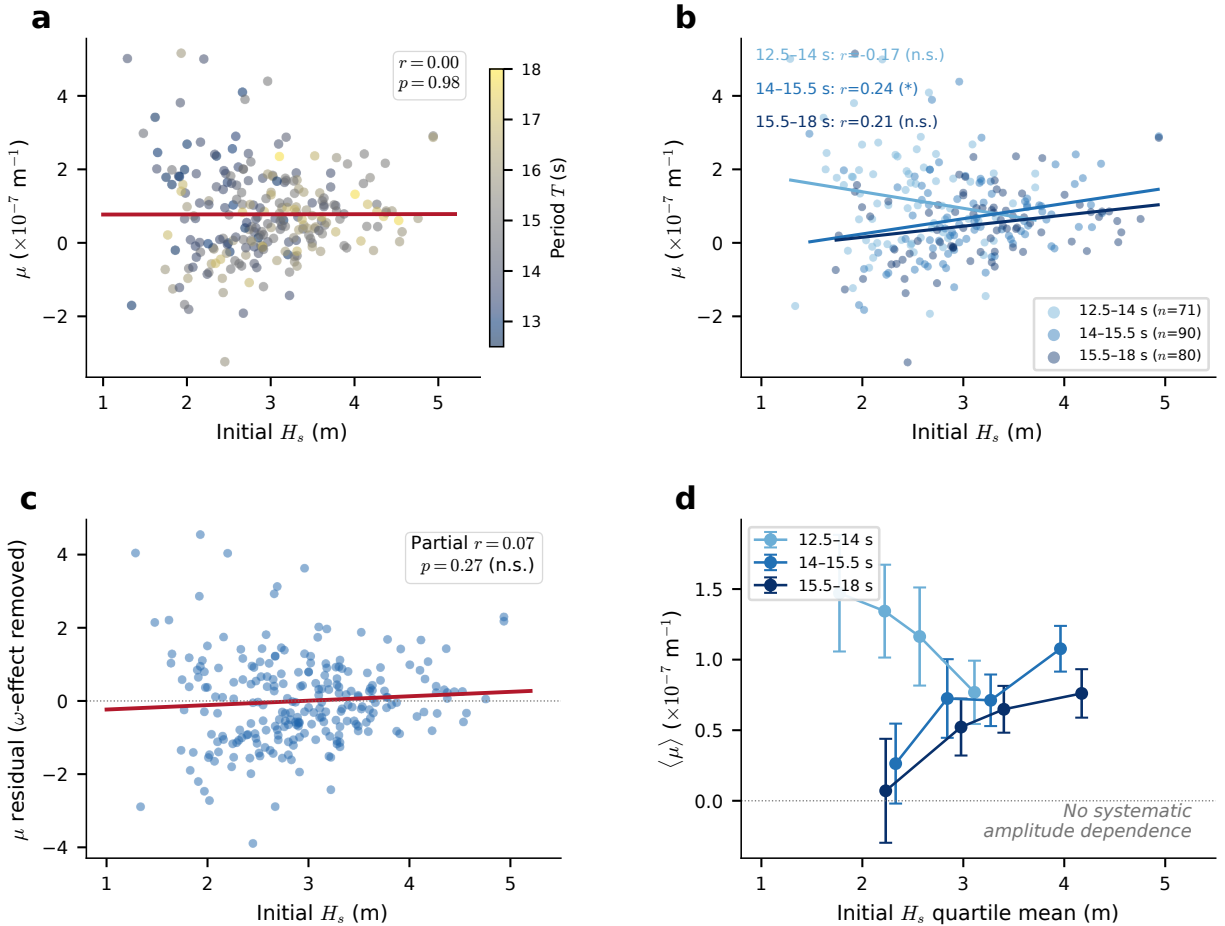
752 Correspondence and requests for materials should be
753 addressed to G.L. (guoqiang.liu@ku.ac.ae).



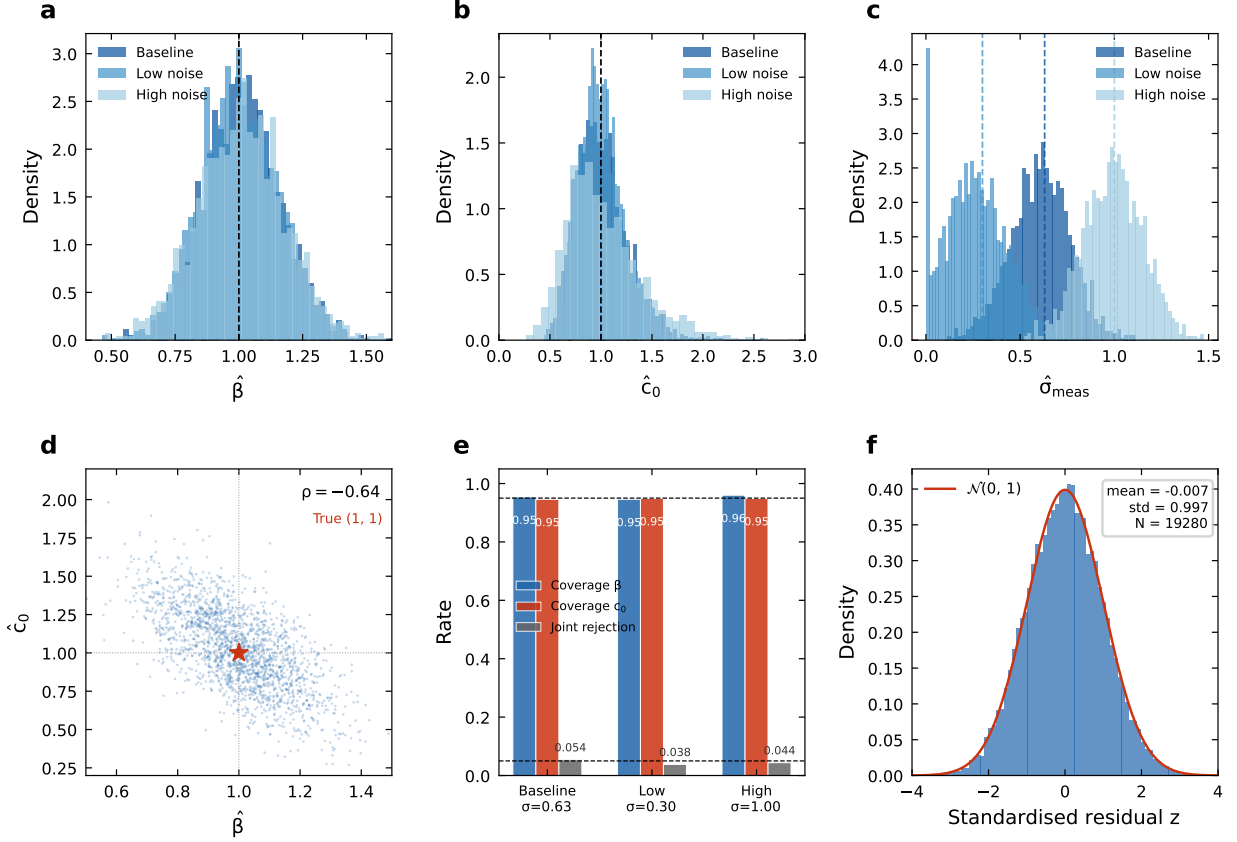
Extended Data Figure 1. **Decorrelation timescale comparison at swell-selected scales.** The Green-Kubo friction coefficient depends on the autocorrelation time of the stochastic vortex force. Two mechanisms compete to destroy that correlation: eddy turnover, with timescale $\tau_{\text{eddy}} \sim (\varepsilon q^2)^{-1/3}$, and advective sweeping by the wave packet, with timescale $\tau_{\text{adv}} = (qc_g)^{-1}$. For remote swell the group speed $c_g \sim 8\text{--}15 \text{ m s}^{-1}$ far exceeds mixed-layer turbulent velocities, making sweeping faster by orders of magnitude at all relevant eddy scales. **a**, Timescale comparison for $T = 15 \text{ s}$ swell ($c_g \approx 11.7 \text{ m s}^{-1}$). Red: τ_{adv} ; blue family: τ_{eddy} for $\varepsilon = 10^{-7}$, 5×10^{-7} , and $10^{-6} \text{ m}^2 \text{ s}^{-3}$. At the swell wavenumber $k_{\text{swell}} \approx 0.018 \text{ rad m}^{-1}$ the ratio $\delta = \tau_{\text{adv}}/\tau_{\text{eddy}} \approx 0.003$, confirming that, during each encounter, the eddy field is quasi-frozen for spatial sampling, even though its weak internal evolution remains essential for irreversibility. **b**, Normalised spatial correlation functions $\rho(s)$ with $s = qc_g t$. Exponential correlator (solid): $C_\tau = 1.00$; Gaussian correlator (dashed): $C_\tau = 0.89$. Shaded area equals C_τ . The physical range $C_\tau \in [0.89, 1.25]$ contributes less than 15% uncertainty to the total prefactor C_{tot} , making the theory insensitive to the unknown functional form of the turbulent correlator.



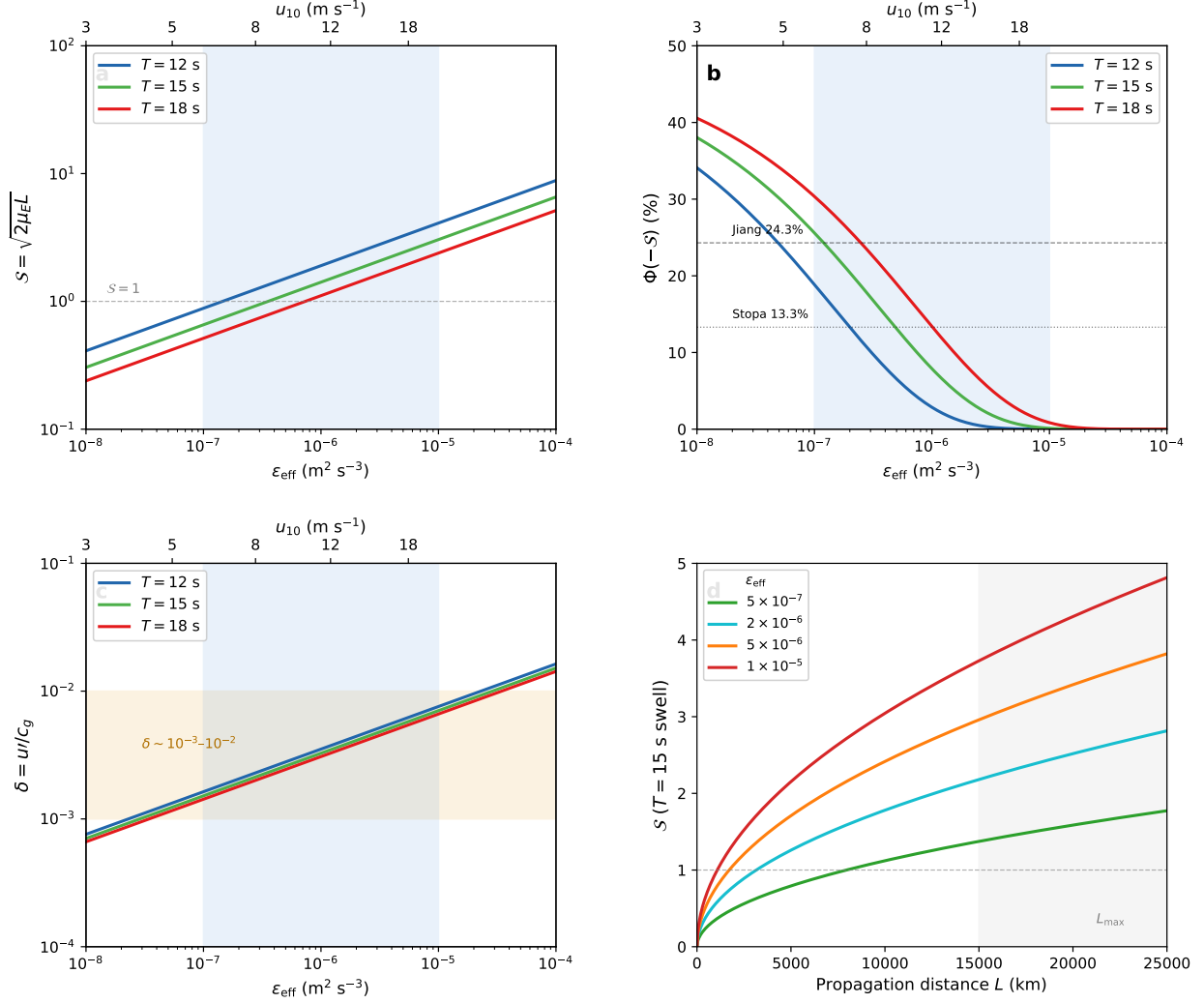
Extended Data Figure 2. **Breaking-layer contamination test for the swell coupling efficiency.** The effective dissipation rate ε_{eff} entering the scaling law is the orbital-weighted depth average of the turbulent dissipation profile (SI S5D). Near-surface wave-breaking eddies could, in principle, bias ε_{eff} upward, but the scale-selection window suppresses their contribution. Parameters: $U_{10} = 10 \text{ m s}^{-1}$, local wind-wave $H_{s,w} = 2.2 \text{ m}$ (Pierson-Moskowitz), swell band $T = 12\text{--}20 \text{ s}$. **a**, Depth profiles of turbulent dissipation rate $\varepsilon(z)$ under the wall-law model (blue solid) and the Tarray surface-enhanced model with $c_1 = 4$ (red dashed). The Tarray profile shows three layers: constant dissipation at $z < z_b = 0.6 H_{s,w} = 1.3 \text{ m}$ (dark shading), power-law decay to $z_t = c_1 H_{s,w} = 9 \text{ m}$ (light shading), and wall-law asymptote below. Near-surface enhancement reaches $\sim 7\times$. Coloured dotted lines mark the swell orbital penetration depth $\delta_E = (2k)^{-1}$ for periods 12–20 s (purple band), which lies entirely below the breaking layer. **b**, Scale-selection window $\bar{W}(q/k) = x^2/(1+x^2)^2$ (solid) and spectral contribution density $x^{4/3}\bar{W}(x)$ (dashed). Swell-scale eddies ($q \sim k$, purple band) dominate the coupling integral. Wind-wave breaking eddies ($q_b/k \sim 30\text{--}300$, red band) are suppressed by $\bar{W} \sim 4 \times 10^{-4}$: including them in ε_{eff} while retaining the baseline C_S would double-count their contribution. **c**, Integrated Tarray-to-wall-law ratio for swell damping as a function of swell period, after applying the coupling filter and orbital weight e^{-2kz} . All ratios are within 10% of unity, confirming that the wall-law baseline used throughout this paper is self-consistent with the spectral framework even when near-surface breaking enhancement is present.



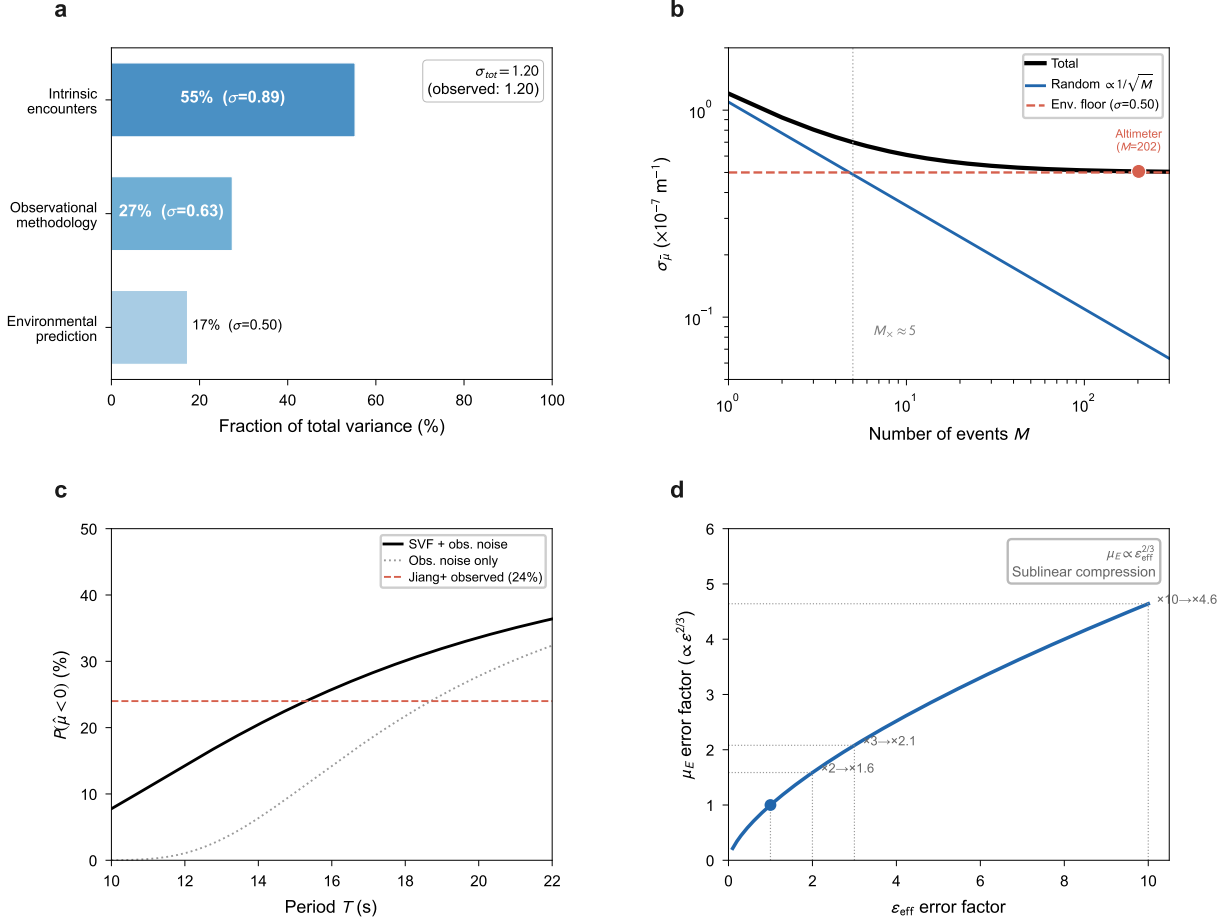
Extended Data Figure 3. **Amplitude dependence of the attenuation rate.** **a**, Observed $\hat{\mu}$ versus initial significant wave height $H_{s,0}$ for 241 satellite swell tracks, coloured by wave period. The red line is the ordinary least-squares fit ($r = 0.00$, $p = 0.98$). The empirical amplitude-dependent formulation predicts $\mu_E \propto H_s^2$, implying a factor-of-14 variation across the observed dynamic range; none is detected. **b**, Data partitioned into three period bins with regression lines per bin. No bin shows a significant positive trend at the 1% level ($|r| \leq 0.24$, $R^2 \lesssim 0.06$). **c**, Partial correlation after removing the $\omega^{8/3}$ dependence by regression: $r_{\text{partial}} = 0.07$ ($p = 0.27$), confirming no residual amplitude effect. **d**, Quartile-binned mean $\langle \hat{\mu} \rangle$ (± 1 s.e.m.) versus $H_{s,0}$ within each period group, showing no systematic trend. The non-detection is particularly significant because the factor-of-3.8 dynamic range in $H_{s,0}$ would produce a factor-of-14 signal under the empirical amplitude-dependent parameterisation, well above the observational noise floor.



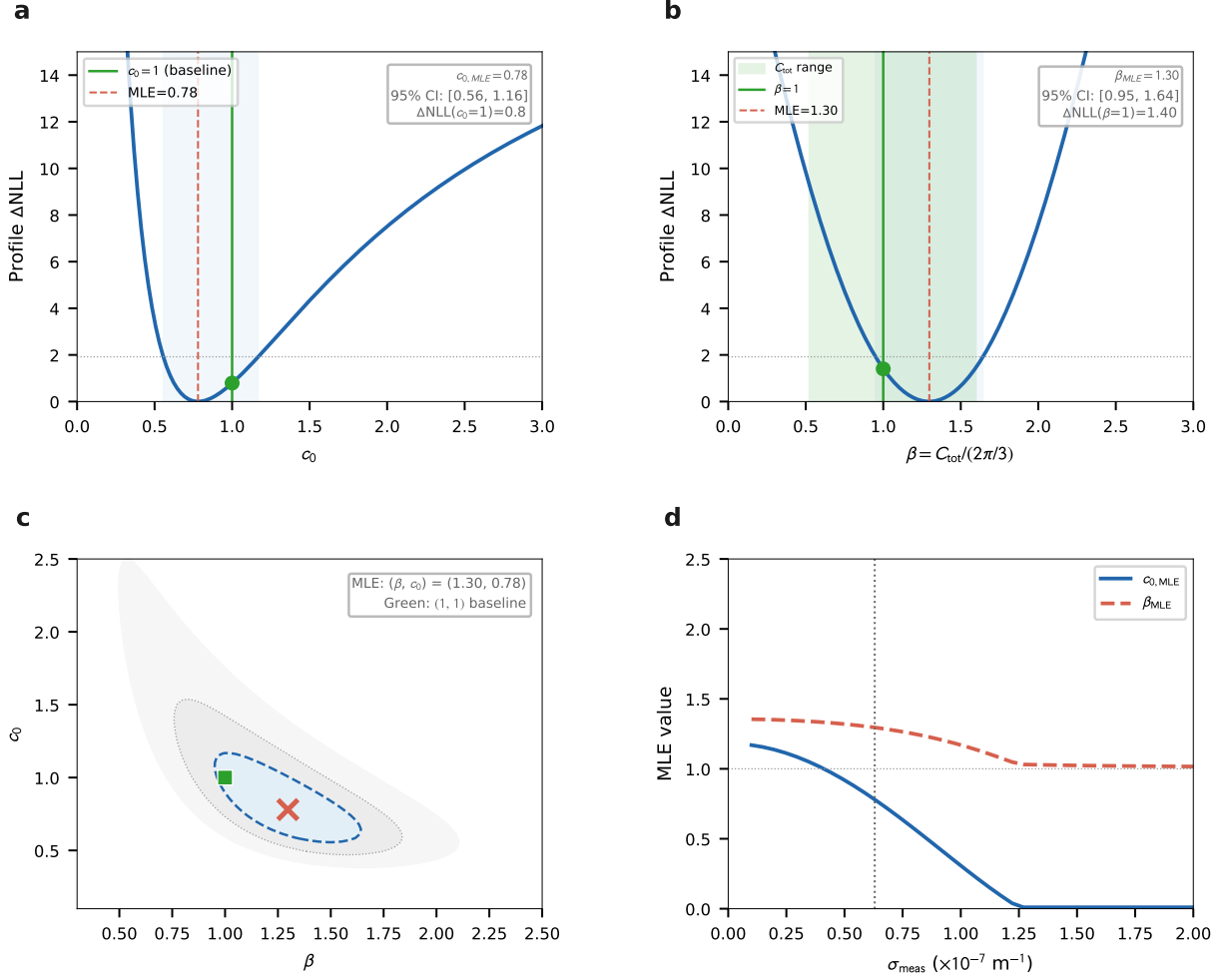
Extended Data Figure 4. **Fixed-design Monte Carlo validation of the heteroscedastic inference layer.** The 241-track design matrix ($L_i, \mu_{svf,i}$) is held fixed and only the observations are regenerated from the model $\hat{\mu}_i \sim \mathcal{N}(\beta^* \mu_{svf,i}, c_0^* \beta^* \mu_{svf,i} / L_i + \sigma_{meas}^{*2})$ with $(\beta^*, c_0^*) = (1, 1)$ and $R = 2000$ replications per scenario. Three noise levels are tested: baseline $\sigma_{meas}^* = 0.63$ (dark shading), low noise 0.30 (medium), and high noise 1.00 (light), all in units of 10^{-7} m^{-1} . **a**, $\hat{\beta}$ recovery. All three scenarios centre on $\beta^* = 1$ (dashed) with $|\text{bias}| < 0.003$. **b**, \hat{c}_0 recovery. The distribution is right-skewed ($c_0 \geq 0$ by construction) but $|\text{bias}| < 0.02$ in every case. **c**, $\hat{\sigma}_{meas}$ recovery. Dashed lines mark the imposed truth for each scenario. **d**, Joint ($\hat{\beta}, \hat{c}_0$) cloud for the baseline scenario. The moderate anticorrelation ($\rho \approx -0.64$) reflects a partial trade-off between mean scaling and variance scaling but does not compromise identifiability. **e**, Coverage and joint rejection summary. Profile-likelihood 95% coverage for β (blue) and c_0 (red) is 94.6-96.0% across all scenarios (nominal 95%, dashed line). Joint true-value rejection rates (green) are 3.8-5.4% (nominal 5%). **f**, Pooled standardised residuals from the first 80 baseline replicates ($N = 19,280 = 80 \times 241$). Mean 0.003, standard deviation 1.000, consistent with $\mathcal{N}(0, 1)$ (red curve).



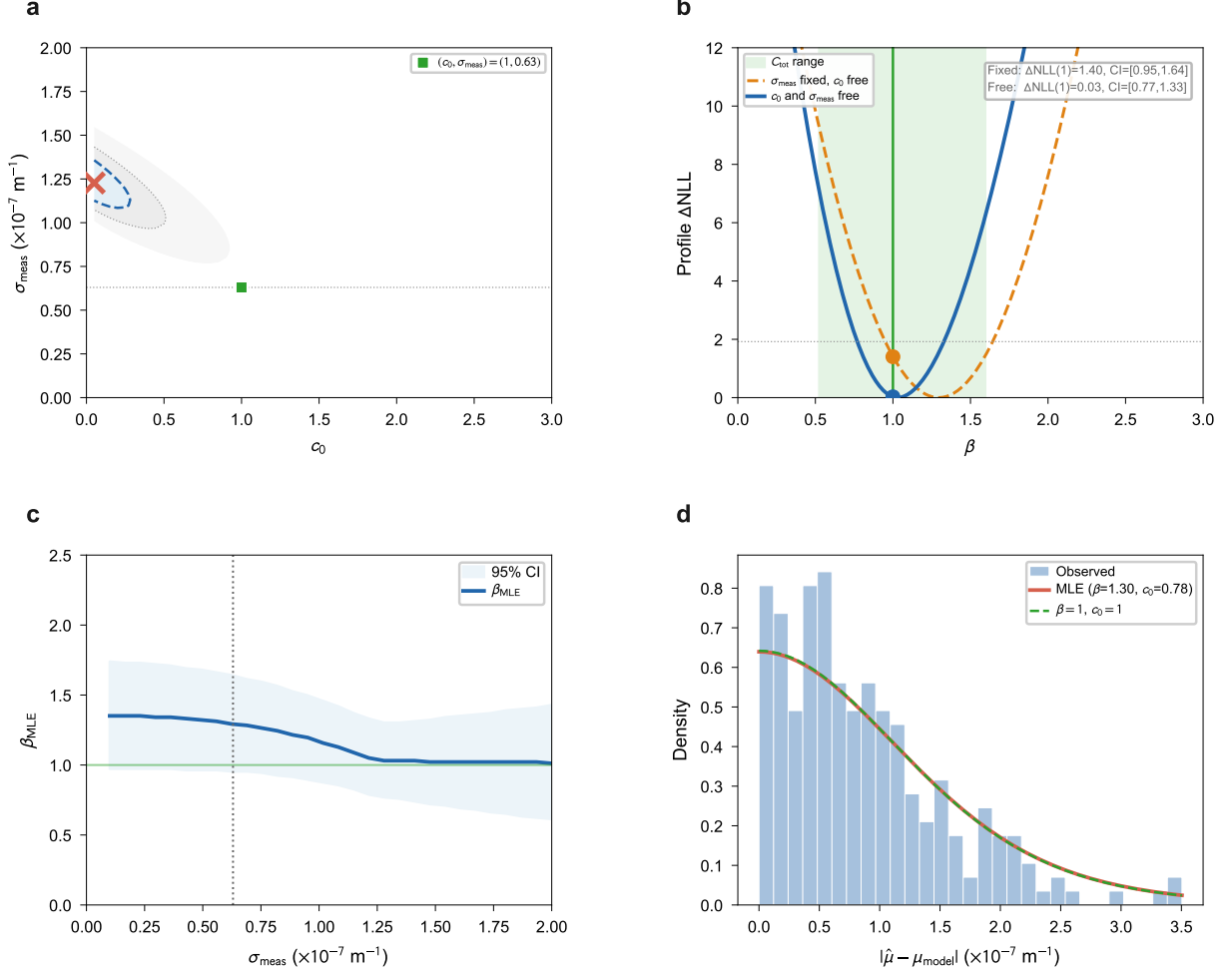
Extended Data Figure 5. **Signal-to-noise regime of far-field swell tracks.** A single satellite track measures the log-energy slope $\hat{\mu}$, which scatters around the ensemble mean $2\mu_E$ with intrinsic standard deviation $\sqrt{2\mu_E/L}$. The signal-to-noise ratio $S = \sqrt{2\mu_E L}$ determines whether a given track can resolve the mean: when $S \lesssim 1$ the negative tail of the estimator distribution extends past zero, producing apparent energy gain. This figure maps S and the resulting negative fraction across the realistic far-field parameter space. Parameters: $L = 10,000$ km, $c_0 = 1$. Upper axes convert ϵ_{eff} to indicative 10-m wind speed via the wall-law parameterisation; light blue shading marks the typical far-field range $\epsilon_{\text{eff}} \sim 10^{-7} - 10^{-5} \text{ m}^2 \text{ s}^{-3}$. **a**, S versus ϵ_{eff} for three swell periods $T = 12, 15,$ and 18 s. Shorter-period swell (higher ω) has larger $\mu_E \propto \omega^{8/3}$ and hence higher S . **b**, Predicted negative fraction $\Phi(-S)$ versus ϵ_{eff} , showing the transition from $\sim 40\%$ (calm, long-period) to $\lesssim 1\%$ (windy, short-period). Dashed lines: observed aggregate fractions from the two datasets. **c**, Small parameter $\delta = u'/c_g$ versus ϵ_{eff} , confirming $\delta \sim 10^{-3} - 10^{-2}$ and justifying the weak-coupling expansion underlying the entire framework. **d**, S versus propagation distance L for $T = 15$ s swell. Because $S \propto \sqrt{L}$ and trans-oceanic propagation distances are finite, the intrinsic scatter cannot be eliminated by better instruments. It is a fundamental prediction of the theory.



Extended Data Figure 6. **Variance budget and frequency dependence of the negative tail.** Each satellite-derived attenuation rate $\hat{\mu}$ deviates from the true ensemble mean $2\mu_E$ for three independent reasons: random turbulent encounters along the propagation path (intrinsic), observational methodology errors, and spatial variability of the environment. This figure quantifies the three channels and shows that the frequency dependence of the negative-rate fraction is an unambiguous fingerprint of the intrinsic mechanism. Representative parameters: $\bar{\mu}_{\text{obs}} = 0.8 \times 10^{-7} \text{ m}^{-1}$ ($\mu_E \approx 0.40 \times 10^{-7}$), $L = 10,000 \text{ km}$, $c_0 = 1$. **a**, Variance decomposition. Intrinsic encounter noise contributes 55% of the total variance ($\sigma_{\text{int}} = 0.89 \times 10^{-7} \text{ m}^{-1}$), observational methodology 27% ($\sigma_{\text{obs}} = 0.63$), and environmental prediction 17% ($\sigma_{\text{env}} = 0.50$). The predicted total $\sigma_{\text{tot}} = 1.20$ is consistent with the observed spread, confirming closure of the variance budget without tuning. **b**, Standard deviation of the ensemble-mean estimator versus number of averaged events M . The crossover $M_x \approx 5$ separates the random-scatter-limited regime ($\sigma \propto 1/\sqrt{M}$) from the environment-limited floor. The altimeter dataset [4] ($M = 202$) is deeply environment-limited, explaining why adding more tracks cannot sharpen the ensemble mean further. **c**, Frequency-resolved negative-rate fraction $P_{\text{neg}}(T)$. Observational noise alone (grey dotted) gives a nearly flat curve; the combined prediction (black solid) shows a steep rise from $\sim 7\%$ at $T = 11 \text{ s}$ to $\sim 28\%$ at $T = 20 \text{ s}$. This steep frequency dependence is the discriminating signature: it vanishes if the negative rates were purely instrumental. The altimeter-observed aggregate of 24% (red dashed) is consistent with the theory across the observed period range. **d**, Error buffering by the $2/3$ exponent in $\mu_E \propto \varepsilon_{\text{eff}}^{2/3}$: a factor-of-3 uncertainty in ε_{eff} compresses to a factor-of-2.1 in μ_E , and even a factor-of-10 error produces less than a factor-of-5 bias. This sublinear compression explains why a climatological estimate of ε_{eff} suffices for quantitative prediction.



Extended Data Figure 7. **Likelihood analysis confirms the zero-parameter prediction at both the first- and second-moment levels.** The predictive distribution for each track is $\hat{\mu}_i \sim \mathcal{N}(\mu_{\text{model},i}, c_0 \cdot 2\mu_{E,i}^{\text{SVF}}/L_i + \sigma_{\text{meas}}^2)$ where $\mu_{\text{model},i} = 2\beta\mu_{E,i}^{\text{SVF}} + \mu_{v,i}^{\text{Dore}}$; β scales the SVF component while the laminar term remains fixed. The intrinsic variance is proportional to the SVF part alone, because the Dore channel is deterministic. The Green-Kubo zero-parameter prediction corresponds to $\beta = 1$ ($C_{\text{tot}} = 2\pi/3$) with $c_0 = 1$. **a**, Profile negative log-likelihood for c_0 (marginalised over β). $c_{0, \text{MLE}} = 0.78$ (red dashed), 95% CI [0.56, 1.16]. The baseline $c_0 = 1$ (green) lies within the 95% CI ($\Delta\text{NLL} = 0.8$), so the near-independent-encounter second-moment prediction is not rejected. The MLE lying below 1 is consistent with weak inter-encounter correlations that partially cancel the random-walk scatter (SI S6 E). **b**, Profile negative log-likelihood for $\beta = C_{\text{tot}}/(2\pi/3)$, marginalised over c_0 . $\beta_{\text{MLE}} = 1.30$, 95% CI [0.95, 1.64]. Green band: theoretical C_{tot} range [1.10, 3.34] (SI S5). $\beta = 1$ falls within both the statistical 95% CI ($\Delta\text{NLL} = 1.40$) and the C_{tot} range. The zero-parameter mean law is not rejected. **c**, Joint (β, c_0) likelihood contour. Dashed curves: 68% and 95% contours. Red cross: joint MLE $(\beta, c_0) = (1.30, 0.78)$; green square: zero-parameter baseline (1, 1). The baseline sits inside the 95% contour: both moments are simultaneously consistent with the data. **d**, Sensitivity to the assumed measurement noise σ_{meas} . Blue: $c_{0, \text{MLE}}$; red dashed: β_{MLE} . Vertical dotted: reference value $\sigma_{\text{meas}} = 0.63 \times 10^{-7} \text{ m}^{-1}$. β_{MLE} stabilises near 1.0-1.3 across the full range; $c_{0, \text{MLE}}$ decreases as more variance is absorbed by σ_{meas} . The first-moment prediction is immune to the variance partition.



Extended Data Figure 8. **Joint likelihood analysis confirms the robustness of the zero-parameter mean law to the variance decomposition.** The predictive variance contains two channels: intrinsic encounter noise $c_0 \mu_{\text{svf},i}/L_i$ and a non-intrinsic term σ_{meas}^2 . These are partially degenerate in the likelihood. **a**, Joint ΔNLL at $\beta = 1$ in the $(c_0, \sigma_{\text{meas}})$ plane. Dashed curves: 95% and 99% contours. Red cross: MLE ($c_0 \approx 0.1$, $\sigma_{\text{meas}} \approx 1.25 \times 10^{-7} \text{ m}^{-1}$), located on a likelihood ridge along which c_0 and σ_{meas} trade off at nearly constant total variance. Green square: baseline operating point $(c_0, \sigma_{\text{meas}}) = (1, 0.63)$ adopted in Figures 4-5. **b**, Profile ΔNLL for $\beta = C_{\text{tot}}/(2\pi/3)$ under two treatments. Orange dashed: $\sigma_{\text{meas}} = 0.63 \times 10^{-7}$ fixed, c_0 free ($\Delta\text{NLL}(\beta=1) = 1.40$; 95% CI [0.95, 1.64]). Blue solid: c_0 and σ_{meas} jointly free ($\Delta\text{NLL}(\beta=1) = 0.03$; 95% CI [0.77, 1.33]). Green band: theoretical C_{tot} range [1.10, 3.34] from SI S5. Under both treatments $\beta = 1$ lies well within the 95% CI and the C_{tot} range; with both nuisance parameters free, $\beta = 1$ is nearly indistinguishable from the MLE. **c**, β_{MLE} and its 95% CI (shaded) as a function of the assumed σ_{meas} . The MLE remains in the range 1.0-1.35 and the 95% band includes $\beta = 1$ throughout, confirming that the first-moment prediction is immune to the variance partition. Vertical dotted line: reference value 0.63×10^{-7} . **d**, Absolute residual distribution. Histogram: observed $|\hat{\mu}_i - \mu_{\text{model},i}|$. Red solid: MLE prediction ($\beta = 1.30$, $c_0 = 0.78$). Green dashed: baseline (β, c_0) = (1, 1). Both capture the shape of the residuals. $N = 241$.

* Corresponding author: guoqiang.liu@ku.ac.ae

- [1] Melville S. Green, Markoff random processes and the statistical mechanics of time-dependent phenomena. II. Irreversible processes in fluids, *J. Chem. Phys.* **22**, 398–413 (1954).
- [2] Ryogo Kubo, Statistical-mechanical theory of irreversible processes. I. General theory and simple applications to magnetic and conduction problems, *J. Phys. Soc. Jpn.* **12**, 570–586 (1957).
- [3] F. E. Snodgrass, G. W. Groves, K. Hasselmann, G. R. Miller, W. H. Munk, and W. H. Powers, Propagation of ocean swell across the Pacific, *Philosophical Transactions of the Royal Society of London. Series A* **249**, 431–497 (1966).
- [4] H. Jiang, J. E. Stopa, H. Wang, R. Husson, A. Mouche, B. Chapron, and G. Chen, Tracking the attenuation and nonbreaking dissipation of swells using altimeters, *Journal of Geophysical Research: Oceans* **121**, 1446–1458 (2016).
- [5] Alexander V. Babanin, *Breaking and Dissipation of Ocean Surface Waves* (Cambridge University Press, 2011).
- [6] A. D. D. Craik and S. Leibovich, A rational model for Langmuir circulations, *J. Fluid Mech.* **73**, 401–426 (1976).
- [7] J. C. McWilliams, *Quasi-linear Theory for Surface Wave-Current Interactions* (Springer, 2022).
- [8] Robert Zwanzig, *Nonequilibrium Statistical Mechanics* (Oxford University Press, New York, 2001).
- [9] W. Wang and R. X. Huang, Wind energy input to the surface waves, *J. Phys. Oceanogr.* **34**, 1276–1280 (2004).
- [10] N. Rascle, F. Ardhuin, and E. A. Terray, Drift and mixing under the ocean surface: A coherent one-dimensional description with application to unstratified conditions, *J. Geophys. Res.* **111**, C03016 (2006).
- [11] W. K. Melville, The role of surface-wave breaking in air-sea interaction, *Annual Review of Fluid Mechanics* **28**, 279–321 (1996).
- [12] Fabrice Ardhuin, Erick Rogers, Alexander V. Babanin, et al., Semiempirical dissipation source functions for ocean waves. Part I: Definition, calibration, and validation, *J. Phys. Oceanogr.* **40**, 1917–1941 (2010).
- [13] B. D. Dore, Some effects of the air-water interface on gravity waves, *Geophysical & Astrophysical Fluid Dynamics* **10**, 215–230 (1978).
- [14] Fabrice Ardhuin, Bertrand Chapron, and Fabrice Collard, Observation of swell dissipation across oceans, *Geophysical Research Letters* **36**, L06607 (2009).
- [15] Fabrice Collard, Fabrice Ardhuin, and Bertrand Chapron, Monitoring and analysis of ocean swell fields from space: New methods for routine observations, *J. Geophys. Res.* **114**, C07023 (2009).
- [16] Sidney Leibovich, The form and dynamics of Langmuir circulations, *Annu. Rev. Fluid Mech.* **15**, 391–427 (1983).
- [17] K. Hasselmann, On the spectral dissipation of ocean waves due to white capping, *Boundary-Layer Meteorol.* **6**, 107–127 (1974).
- [18] G. J. Komen, L. Cavaleri, M. Donelan, K. Hasselmann, S. Hasselmann, and P. A. E. M. Janssen, *Dynamics and Modelling of Ocean Waves* (Cambridge University Press, 1994).
- [19] S. Zieger, A. V. Babanin, W. E. Rogers, and I. R. Young, Observation-based source terms in the third-generation wave model WAVEWATCH, *Ocean Model.* **96**, 2–25 (2015).
- [20] J. E. Stopa, F. Ardhuin, A. Babanin, and S. Zieger, Comparison and validation of physical wave parameterizations in spectral wave models, *Ocean Model.* **103**, 2–17 (2016).
- [21] G. K. Batchelor, *An Introduction to Fluid Dynamics* (Cambridge University Press, Cambridge, 1967).
- [22] James C. McWilliams, Peter P. Sullivan, and Chin-Hoh Moeng, Langmuir turbulence in the ocean, *J. Fluid Mech.* **334**, 1–30 (1997).
- [23] Hazime Mori, Transport, collective motion, and Brownian motion, *Prog. Theor. Phys.* **33**, 423–455 (1965).
- [24] Robert Zwanzig, Memory effects in irreversible thermodynamics, *Phys. Rev.* **124**, 983–992 (1961).
- [25] Ming Han, Michel Fruchart, Colin Scheibner, Suriyanarayanan Vaikuntanathan, Juan J. de Pablo, and Vincenzo Vitelli, Fluctuating hydrodynamics of chiral active fluids, *Nature Physics* **17**, 1260–1269 (2021).
- [26] Ryogo Kubo, Morikazu Toda, and Natsuki Hashitsume, *Statistical Physics II: Nonequilibrium Statistical Mechanics*, 2nd ed. (Springer, Berlin, 1991).
- [27] Y. Katznelson, *An Introduction to Harmonic Analysis*, 3rd ed. (Cambridge Univ. Press, 2004).
- [28] Francis P. Bretherton and Christopher J. R. Garrett, Wavetrains in inhomogeneous moving media, *Proceedings of the Royal Society of London. Series A* **302**, 529–554 (1968).
- [29] M. A. C. Teixeira and S. E. Belcher, On the distortion of turbulence by a progressive surface wave, *Journal of Fluid Mechanics* **458**, 229–267 (2002).
- [30] N. S. Oakey, Determination of the rate of dissipation of turbulent energy from simultaneous temperature and velocity shear microstructure measurements, *J. Phys. Oceanogr.* **12**, 256–271 (1982).
- [31] E. Kunze, A unified model spectrum for anisotropic stratified and isotropic turbulence in the ocean and atmosphere, *J. Phys. Oceanogr.* **49**, 385–407 (2019).
- [32] Haoyu Jiang, Justin E. Stopa, He Wang, Romain Husson, Alexis Mouche, Bertrand Chapron, and Ge Chen, Tracking the attenuation and nonbreaking dissipation of swells using altimeters, *Remote Sensing of Environment* **200**, 446–459 (2017).
- [33] Robert Atlas, Ross N. Hoffman, Joseph Ardizzone, S. Mark Leidner, Juan Carlos Jusem, Deborah K. Smith, and Daniel Gombos, A cross-calibrated, multiplatform ocean surface wind velocity product for meteorological and oceanographic applications, *Bull. Amer. Meteor. Soc.* **92**, 157–174 (2011).
- [34] Carl A. Mears, Deborah K. Smith, and Frank J. Wentz, Comparison of Cross-Calibrated Multi-Platform (CCMP) ocean surface wind products with moored buoys, *Remote Sens.* **14**, 4083 (2022).
- [35] ECCO Consortium, Ichiro Fukumori, Ou Wang, Ian Fenty, Gaël Forget, Patrick Heimbach, and Rui M. Ponte, *ECCO central estimate, version 4 release 4*, PO.DAAC (2021).
- [36] Qingxiang Liu, Alexander V. Babanin, Yalin Fan, Stefan Zieger, Changlong Guan, and Ian R. Young, Numerical simulations of ocean surface waves under hurricane conditions: Assessment of existing model performance, *Ocean Model.* **118**, 73–93 (2017).
- [37] S. E. Belcher, A. L. M. Grant, K. E. Hanley, B. Fox-Kemper, L. Van Roekel, P. P. Sullivan, W. G. Large, A. Brown, A. Hines, D. Calvert, A. Rutgersson, H. Pettersson, J.-R. Bidlot, P. A. E. M. Janssen, and J. A. Polton, A global perspective on Langmuir turbulence in the ocean surface boundary layer, *Geophys. Res. Lett.* **39**, L18605 (2012).
- [38] Baylor Fox-Kemper, Leah Johnson, and Fangli Qiao, Ocean near-surface layers, in *Ocean Mixing*, edited by

- 888 Michael Meredith and Alberto Naveira Garabato (Elsevier, 2022) pp. 65–94. 910
- 889 911
- 890 [39] Fangli Qiao, Yeli Yuan, Yongzeng Yang, Quanan Zheng, Changshui Xia, and Jian Ma, Wave-induced mixing in the upper ocean: Distribution and application to a global ocean circulation model, *Geophysical Research Letters* **31**, L11303 (2004). 912–916
- 891 913
- 892 914
- 893 915
- 894 916
- 895 [40] T. G. Mason and D. A. Weitz, Optical measurements of frequency-dependent linear viscoelastic moduli of complex fluids, *Phys. Rev. Lett.* **74**, 1250–1253 (1995). 917–919
- 896 918
- 897 919
- 898 [41] T. M. Squires and T. G. Mason, Fluid mechanics of microrheology, *Annu. Rev. Fluid Mech.* **42**, 413–438 (2010). 920–922
- 899 921
- 900 922
- 901 [42] Adrean Webb and Baylor Fox-Kemper, Wave spectral moments and Stokes drift estimation, *Ocean Model.* **40**, 273–288 (2011). 923–925
- 902 924
- 903 925
- 904 [43] Denis J. Evans and Gary P. Morriss, *Statistical Mechanics of Nonequilibrium Liquids*, 2nd ed. (Cambridge University Press, Cambridge, 2008). 926–928
- 905 927
- 906 928
- 907 [44] U. M. B. Marconi, A. Puglisi, L. Rondoni, and A. Vulpiani, Fluctuation-dissipation: Response theory in statistical physics, *Phys. Rep.* **461**, 111–195 (2008). 929–931
- 908 930
- 909 931
- 932
- [45] Albert Einstein, Über die von der molekularkinetischen Theorie der Wärme geforderte Bewegung von in ruhenden Flüssigkeiten suspendierten Teilchen, *Ann. Phys.* **322**, 549–560 (1905).
- [46] S. Bochner, Monotone Funktionen, Stieltjessche Integrale und harmonische Analyse, *Math. Ann.* **108**, 378–410 (1933).
- [47] S. B. Pope, *Turbulent Flows* (Cambridge University Press, 2000).
- [48] K. R. Sreenivasan, On the universality of the Kolmogorov constant, *Phys. Fluids* **7**, 2778–2784 (1995).
- [49] H. Hersbach, B. Bell, P. Berrisford, S. Hirahara, A. Horányi, J. Muñoz Sabater, J. Nicolas, C. Peubey, R. Radu, D. Schepers, A. Simmons, C. Soci, S. Abdalla, X. Abellan, G. Balsamo, P. Bechtold, G. Biavati, J. Bidlot, M. Bonavita, G. De Chiara, P. Dahlgren, D. Dee, M. Diamantakis, R. Dragani, J. Flemming, R. Forbes, M. Fuentes, A. Geer, L. Haimberger, S. Healy, R. J. Hogan, E. Hólm, M. Janisková, S. Keeley, P. Laloyaux, P. Lopez, C. Lupu, G. Radnoti, P. de Rosnay, I. Rozum, F. Vamborg, S. Villaume, and J.-N. Thépaut, The ERA5 global reanalysis, *Quarterly Journal of the Royal Meteorological Society* **146**, 1999–2049 (2020).

Supplementary Information for
A universal law for non-breaking surface wave decay

Guoqiang Liu^{1,*} and Maryam Al Alshehhi¹

¹*Civil, Infrastructural and Environmental Engineering,
Khalifa University of Science and Technology, Abu Dhabi, United Arab Emirates*

**Corresponding author: guoqiang.liu@ku.ac.ae*

Contents

S1	From Navier-Stokes to the stochastic vortex force	3
	A Incompressible Navier-Stokes equations and Helmholtz decomposition	3
	B Orbital vortex force and its energetic role	4
	C Wave-phase averaging, Stokes drift and gradient equivalence	4
	D Three-layer vorticity decomposition and the McWilliams identity	6
	E Identification of the stochastic vortex force	8
S2	Non-negativity of the Green-Kubo damping coefficient	10
	A Assumptions A1-A6	10
	B Non-equilibrium steady states and FDR-II	13
	C Operational construction of the reference measure	13
	D Time-scale separation and local validity	15
	E Projected dynamics and identification of the stochastic vortex force	15
	F Green-Kubo relation and non-negativity of Γ	17
	G Markovian limit and monotonic energy decay	18
	H Dual-line prediction structure	19
	I Physical origin of irreversibility: the single wave-eddy encounter	19
S3	Evaluating the force autocorrelation in wavenumber space	21
	A The Green-Kubo starting point	21
	B Force autocorrelation in wavenumber-frequency space	22
	C Vortex-force vertex and angular integration	23
	D Scale-selection window	24
	E Frequency integration and the effective correlation time	25
	F Reduced one-dimensional integral and modal normalisation	26
S4	From the force autocorrelation to the swell attenuation law	27
S5	Order-of-magnitude of the prefactor C_{tot} and robustness of the Kolmogorov closure	28
	A The geometric vertex factor \tilde{G}_{geom}	28
	B The scale-selection constant C_S	30
	C The advective correlation factor C_τ	31
	D The vertical-weighting factor C_E	32
	E Effective dissipation rate and numerical baseline	32
	F Self-consistency of window shape and dissipation profile	34
	G Validity of Kolmogorov scaling at swell-selected eddy scales	34
	H Assembly of the total prefactor	35
S6	Random-walk theory and intrinsic variance closure	35

A	Random walk in logarithmic energy	36
B	Variance renormalisation from inter-encounter correlations	41
C	Signal-to-noise ratio and deterministic emergence scale	43
D	Variance decomposition and error budget	45
E	Negative attenuation rates and discriminating tests	46
S7	Comparison with satellite observations	47
A	Altimeter tracking dataset	48
B	SAR tracking dataset	48
C	Variance budget and the Monte Carlo gap	49
D	Fixed-design Monte Carlo validation of the inference layer	50
E	Cross-dataset consistency	51
S8	Amplitude independence of the attenuation rate	51
S9	Domain of validity: why remote swell isolates the universal dissipation law	53

S1. From Navier-Stokes to the stochastic vortex force

We derive the stochastic vortex force (SVF) from the incompressible Navier-Stokes equations under the assumptions stated in the main text (bulk incompressible flow, non-breaking potential waves, negligible air-side friction). We work at leading order in the small wave slope and assume clear separation between the fast wave phase and the slower evolution of currents and turbulent vorticity.

A. Incompressible Navier-Stokes equations and Helmholtz decomposition

Consider an incompressible Newtonian fluid of constant density ρ , neglecting buoyancy, stratification and surface tension. The total Eulerian velocity field $\mathbf{U}(\mathbf{x}, t)$ satisfies

$$\partial_t \mathbf{U} + (\mathbf{U} \cdot \nabla) \mathbf{U} = -\frac{1}{\rho} \nabla P + \nu \nabla^2 \mathbf{U}, \quad \nabla \cdot \mathbf{U} = 0, \quad (\text{S.1})$$

where P is the mechanical pressure (including the hydrostatic contribution $\rho g z$, so that gravity does not appear explicitly) and ν the kinematic viscosity. Following the Helmholtz theorem [1, 2], we decompose the total velocity into an irrotational wave part and a rotational part,

$$\mathbf{U}(\mathbf{x}, t) = \mathbf{u}_\phi(\mathbf{x}, t) + \mathbf{u}(\mathbf{x}, t), \quad (\text{S.2})$$

where $\mathbf{u}_\phi = \nabla \phi$ solves the linear free-surface boundary-value problem for the surface-wave potential, and \mathbf{u} contains all rotational motions. For small-amplitude, non-breaking surface gravity waves, the potential approximation is standard [e.g. 3–5] and implies

$$\nabla \times \mathbf{u}_\phi \approx \mathbf{0}, \quad \nabla \cdot \mathbf{u}_\phi = 0 \quad (\text{in the bulk}). \quad (\text{S.3})$$

Since each component of $\mathbf{u}_\phi = \nabla \phi$ satisfies the Laplace equation in the bulk, $\nabla^2 \mathbf{u}_\phi = \nabla(\nabla^2 \phi) = \mathbf{0}$. The bulk viscous term $\nu \nabla^2 \mathbf{u}_\phi$ therefore vanishes in the interior and drops out of the subtraction below. (Viscous boundary-layer effects on the wave field-Lamb damping-are a separate, much weaker dissipation pathway that is negligible for remote swell and lies outside the present framework.)¹ Since $\mathbf{u}_\phi = \nabla \phi$ is irrotational and divergence-free in the bulk, it satisfies the Euler equation for potential flow in the same pressure convention as Eq. (S.1),

$$\partial_t \mathbf{u}_\phi + (\mathbf{u}_\phi \cdot \nabla) \mathbf{u}_\phi = -\frac{1}{\rho} \nabla p^\varphi, \quad \nabla \cdot \mathbf{u}_\phi = 0, \quad (\text{S.4})$$

where p^φ is the irrotational pressure field in the bulk (equivalently, $p^\varphi/\rho = -\partial_t \phi - \frac{1}{2} |\nabla \phi|^2$ via Bernoulli's relation, with gravity already absorbed into the pressure as in Eq. S.1). Substituting (S.2) into (S.1) and subtracting (S.4) eliminates both the irrotational self-advection $\mathbf{u}_\phi \cdot \nabla \mathbf{u}_\phi$ and the irrotational pressure gradient, giving the governing equation for the rotational component in the bulk (cf. Eq. (2.5) of Xuan et al. 2. Boundary conditions are specified where energy budgets are taken),

$$\partial_t \mathbf{u} + (\mathbf{u} \cdot \nabla) \mathbf{u} = -\mathbf{u}_\phi \cdot \nabla \mathbf{u} - \mathbf{u} \cdot \nabla \mathbf{u}_\phi - \frac{1}{\rho} \nabla p + \nu \nabla^2 \mathbf{u}, \quad \nabla \cdot \mathbf{u} = 0, \quad (\text{S.5})$$

where p is the pressure associated with \mathbf{u} (defined up to an arbitrary function of time). The only approximations are incompressibility and the potential nature of the wave field (S.3).

¹Throughout Sections S1-S4, z is measured upward with the free surface at $z = 0$ ($z \leq 0$ in the fluid, orbital decay $\propto e^{kz}$). Section S5 switches to a depth-downward convention $z \geq 0$, giving kernels e^{-2kz} ; the switch is flagged where it occurs (Eq. S.141).

B. Orbital vortex force and its energetic role

We recast the wave-current coupling terms in (S.5) in vortex-force form. Applying the standard vector identity $(\mathbf{A} \cdot \nabla)\mathbf{B} + (\mathbf{B} \cdot \nabla)\mathbf{A} = \nabla(\mathbf{A} \cdot \mathbf{B}) - \mathbf{A} \times (\nabla \times \mathbf{B}) - \mathbf{B} \times (\nabla \times \mathbf{A})$ [e.g. 1] with $\mathbf{A} = \mathbf{u}_\phi$, $\mathbf{B} = \mathbf{u}$, noting that $\nabla \times \mathbf{u}_\phi \approx \mathbf{0}$ (Eq. (S.3)), and absorbing the resulting gradient $\nabla(\mathbf{u}_\phi \cdot \mathbf{u})$ into a modified pressure $\Pi \equiv p + \rho \mathbf{u}_\phi \cdot \mathbf{u}$, equation (S.5) becomes

$$\boxed{\partial_t \mathbf{u} + (\mathbf{u} \cdot \nabla)\mathbf{u} = \mathbf{u}_\phi \times \boldsymbol{\omega} - \frac{1}{\rho} \nabla \Pi + \nu \nabla^2 \mathbf{u}, \quad \nabla \cdot \mathbf{u} = 0.} \quad (\text{S.6})$$

where $\boldsymbol{\omega} \equiv \nabla \times \mathbf{u}$ is the vorticity of the rotational flow. The instantaneous coupling between the wave orbital motion and the rotational flow appears as the instantaneous *orbital vortex force*

$$\mathbf{f}_v(\mathbf{x}, t) \equiv \mathbf{u}_\phi(\mathbf{x}, t) \times \boldsymbol{\omega}(\mathbf{x}, t). \quad (\text{S.7})$$

We show that \mathbf{f}_v is the *only* term in (S.6) that can exchange energy between the wave field and the rotational flow. Taking the inner product of (S.6) with \mathbf{u} and integrating over the fluid volume V ,

$$\frac{d}{dt} \int_V \frac{1}{2} \rho |\mathbf{u}|^2 dV = \rho \int_V \mathbf{u} \cdot (\mathbf{u}_\phi \times \boldsymbol{\omega}) dV - \int_V \mathbf{u} \cdot \nabla \Pi dV + \rho \nu \int_V \mathbf{u} \cdot \nabla^2 \mathbf{u} dV - \rho \int_V \mathbf{u} \cdot [(\mathbf{u} \cdot \nabla)\mathbf{u}] dV. \quad (\text{S.8})$$

Under horizontally periodic boundary conditions, a rigid-lid upper surface², and sufficient decay of the rotational field at depth ($z \rightarrow -\infty$), the pressure gradient term $\mathbf{u} \cdot \nabla \Pi = \nabla \cdot (\Pi \mathbf{u})$ and the advective nonlinearity $\mathbf{u} \cdot [(\mathbf{u} \cdot \nabla)\mathbf{u}] = \frac{1}{2} \nabla \cdot (|\mathbf{u}|^2 \mathbf{u})$ both integrate to zero by the divergence theorem (the latter redistributes kinetic energy within the rotational subspace but cannot transfer energy to/from the wave). The viscous term gives $\int_V \mathbf{u} \cdot \nabla^2 \mathbf{u} dV = - \int_V |\nabla \mathbf{u}|^2 dV \leq 0$ (the integration by parts produces a boundary term $\oint \mathbf{u} \cdot (\nabla \mathbf{u} \cdot \hat{\mathbf{n}}) dS$ that vanishes under the adopted periodic/impermeable boundary conditions). The energy budget therefore reduces to

$$\frac{d}{dt} \int_V \frac{1}{2} \rho |\mathbf{u}|^2 dV = \rho \int_V \mathbf{u} \cdot (\mathbf{u}_\phi \times \boldsymbol{\omega}) dV - \rho \nu \int_V |\nabla \mathbf{u}|^2 dV, \quad (\text{S.9})$$

confirming that the orbital vortex force $\mathbf{u}_\phi \times \boldsymbol{\omega}$ is the sole retained bulk-interior non-viscous channel of energy exchange between swell and rotational motions. Within the potential-wave approximation, the only bulk term that can transfer energy between the two subspaces is this volume integral. Other wave-energy pathways (boundary layers, breaking, air-side stress) are excluded by construction. The viscous term is strictly dissipative and cannot return energy to the wave.

C. Wave-phase averaging, Stokes drift and gradient equivalence

The classical Craik-Leibovich (CL) theory [6–10] describes the effect of non-breaking surface waves on slowly evolving currents by averaging over the fast wave phase. Let $\langle \cdot \rangle_\varphi$ denote this wave-phase (fast-time) average at fixed Eulerian position. (Throughout this paper, $\langle \cdot \rangle_\varphi$ denotes the wave-phase average and $\langle \cdot \rangle$ the ensemble average over the stationary mixed-layer measure ρ_{ss} , defined in Section S2.) Any field A decomposes as

$$A = \bar{A} + A', \quad \bar{A} \equiv \langle A \rangle_\varphi, \quad \langle A' \rangle_\varphi = 0. \quad (\text{S.10})$$

²The rigid-lid approximation for the rotational flow is the energetically consistent companion to the CL framework [6, Eq. (3.16)]. It introduces errors of $O((ak)^2)$ in the energy balance-of order 10^{-4} - 10^{-3} for remote swell ($ak \sim 0.01$ - 0.05)-the same order as terms already neglected in the potential-wave approximation. The phase-resolved simulations of Xuan et al. [2] adopt the same boundary treatment at $O(1)$ (their Eq. (A3)).

For a monochromatic deep-water wave propagating along $\hat{\mathbf{x}}$ with phase $\varphi \equiv kx - \omega t$, the orbital velocity at a fixed Eulerian position is

$$\mathbf{u}_\phi = a\omega e^{kz}(\cos\varphi \hat{\mathbf{x}} + \sin\varphi \hat{\mathbf{z}}), \quad (\text{S.11})$$

with a the wave amplitude, ω the angular frequency and k the wavenumber ($\omega^2 = gk$ in deep water). Every component is proportional to $\cos\varphi$ or $\sin\varphi$, so averaging over one full period gives

$$\langle \mathbf{u}_\phi \rangle_\varphi = \mathbf{0}, \quad (\text{S.12})$$

exact for the linear wave field at each spatial point. Following McWilliams [6, Chap. 4], we assume clear separation between the wave scales and the mean-flow/turbulence scales. Slowly varying fields have characteristic length scale L and time scale L/V . The waves have wavelength $\lambda \sim 2\pi/k$ and period $T = 2\pi/\omega$. The scale-separation parameter

$$\varepsilon_{\text{CL}} \equiv \frac{V}{C} = \frac{\text{current speed}}{\text{wave phase speed}} \ll 1, \quad (\text{S.13})$$

with $C = \omega/k$ the linear deep-water phase speed, guarantees that any slowly varying field S is effectively constant during a single wave period and can be factored out of the phase average,

$$\langle SQ \rangle_\varphi = S \langle Q \rangle_\varphi + O(\varepsilon_{\text{CL}}/(kL)). \quad (\text{S.14})$$

We refer to (S.14) as the *slow-field extraction rule* and invoke it repeatedly below. The error is controlled by the fractional change of the slow field during one wave period. If S evolves on an advective time scale L/V , then $|T \partial_t S|/|S| = O(V/(\omega L)) = O(\varepsilon_{\text{CL}}/(kL))$. Under the standard CL scale separation $kL \gg 1$ (slow fields vary weakly over a wavelength), this quantity is small [6, Chap. 4]. More generally, the extraction requires only that S be independent of the fast wave phase, i.e. $T/\tau_S \ll 1$ where τ_S is the characteristic evolution time of S . The estimate L/V is the standard large-scale value in the CL setting. Applying (S.10) to the vorticity gives a split into phase-averaged (slow) and wave-slaved (oscillatory) parts,

$$\boldsymbol{\omega} = \boldsymbol{\Omega}_s + \boldsymbol{\omega}_{\text{wave}}, \quad \boldsymbol{\Omega}_s \equiv \langle \boldsymbol{\omega} \rangle_\varphi, \quad \langle \boldsymbol{\omega}_{\text{wave}} \rangle_\varphi = \mathbf{0}. \quad (\text{S.15})$$

The slow vorticity $\boldsymbol{\Omega}_s$ includes all fields that do not depend on the wave phase. It contains both the mean-flow vorticity and the autonomous turbulent vorticity driven by local forcing (wind stress, wave breaking, and buoyancy). Its further decomposition requires a second averaging operation and is carried out in Section D. Let $\boldsymbol{\xi}(\mathbf{x}, t) = \int^t \mathbf{u}_\phi(\mathbf{x}, t') dt'$ be the T -periodic wave-induced displacement, satisfying $\nabla \cdot \boldsymbol{\xi} = 0$ and $\langle \boldsymbol{\xi} \rangle_\varphi = \mathbf{0}$. The Stokes drift is defined in Eulerian form [6, Eq. (3.11)] as

$$\mathbf{u}_s(\mathbf{x}) \equiv \langle (\boldsymbol{\xi} \cdot \nabla) \mathbf{u}_\phi \rangle_\varphi. \quad (\text{S.16})$$

Unlike $\langle \mathbf{u}_\phi \rangle_\varphi = \mathbf{0}$, the Stokes drift is a nonzero *second-order* quantity—the phase average of two correlated first-order oscillatory fields. Within the Generalised Lagrangian Mean (GLM) framework, $\nabla \cdot \mathbf{u}_s = 0$ [6, Eq. (3.12), Appendix C]. Finally, we adopt the gradient-equivalence convention

$$\mathbf{F} \equiv_{\nabla} \mathbf{G} \iff \mathbf{F} - \mathbf{G} = \nabla \chi \text{ for some scalar field } \chi(\mathbf{x}). \quad (\text{S.17})$$

Two forces that are \equiv_{∇} -equivalent have the same curl and produce the same vorticity forcing and volume-integrated power (under the incompressibility and boundary conditions adopted in Eq. (S.9) below), since any gradient can be absorbed into the Bernoulli head. All equalities between forces below are understood in this sense unless stated otherwise.

D. Three-layer vorticity decomposition and the McWilliams identity

The phase-averaged vorticity $\boldsymbol{\Omega}_s \equiv \langle \boldsymbol{\omega} \rangle_\varphi$ introduced in (S.15) contains all fields that vary slowly compared with the wave period. We decompose it further using a second averaging operation—the ensemble average $\langle \cdot \rangle$ over the stationary mixed-layer measure ρ_{ss} ,

$$\boldsymbol{\Omega}_s = \bar{\boldsymbol{\Omega}} + \boldsymbol{\omega}', \quad \bar{\boldsymbol{\Omega}} \equiv \langle \boldsymbol{\Omega}_s \rangle = \langle \langle \boldsymbol{\omega} \rangle_\varphi \rangle, \quad \langle \boldsymbol{\omega}' \rangle = \mathbf{0}. \quad (\text{S.18})$$

Here $\bar{\boldsymbol{\Omega}}$ is the ensemble-mean vorticity of the mean flow and $\boldsymbol{\omega}' \equiv \boldsymbol{\Omega}_s - \bar{\boldsymbol{\Omega}}$ is the zero-ensemble-mean vorticity fluctuation. Physically, $\boldsymbol{\omega}'$ is driven predominantly by local forcing (wind stress, wave breaking, buoyancy) and the turbulent cascade, not by the remote-source swell—a characterisation formalised in Assumptions A3 and A5 (Section S2) and supported by the energetic estimates therein. Under standard ergodicity assumptions, the ensemble mean coincides with the Reynolds mean used in turbulence theory.

A notational convention. From Eq. (S.18) onward, the overbar denotes the *ensemble* mean ($\bar{\boldsymbol{\Omega}} \equiv \langle \boldsymbol{\Omega}_s \rangle$) and the prime the turbulent fluctuation ($\boldsymbol{\omega}' \equiv \boldsymbol{\Omega}_s - \bar{\boldsymbol{\Omega}}$), replacing the earlier phase-decomposition usage. The two averaging operators are always distinguished by the bracket subscript, $\langle \cdot \rangle_\varphi$ for phase, $\langle \cdot \rangle$ for ensemble. Combined with (S.15), this gives the *three-layer* decomposition of the total vorticity,

$$\boxed{\boldsymbol{\omega} = \bar{\boldsymbol{\Omega}} + \boldsymbol{\omega}' + \boldsymbol{\omega}_{\text{wave}}.} \quad (\text{S.19})$$

The first step (phase averaging, yielding $\boldsymbol{\Omega}_s$ and $\boldsymbol{\omega}_{\text{wave}}$) follows the standard CL framework of McWilliams [6], who treats $\boldsymbol{\Omega}_s$ as a single deterministic slow field. The second step is where the statistical-mechanical structure enters. By splitting $\boldsymbol{\Omega}_s$ into its ensemble mean $\bar{\boldsymbol{\Omega}}$ and the zero-mean turbulent fluctuation $\boldsymbol{\omega}'$, we assign the roles that the Mori-Zwanzig formalism (Section S2) will formalise: the swell amplitude is the slow observable, and $\boldsymbol{\omega}'$ is the fast bath whose autonomous dynamics supply both the random force and the dissipation kernel. This separation is absent in the CL framework, whose design target is the phase-averaged wave-induced forces acting on the slow-time current evolution, not wave dissipation [6, Chap. 11]. Within CL, $\boldsymbol{\Omega}_s$ enters diagnostically as a given field. For any configuration of the slow flow it determines the Stokes vortex force $\mathbf{u}_s \times \boldsymbol{\Omega}_s$. As a deterministic framework, CL does not introduce the statistical-mechanical structure (ensemble averaging, autocorrelation functions) from which a friction coefficient could be constructed. Wave dissipation is explicitly left to other mechanisms [6, p. 54]. Our contribution is to show that the dissipation mechanism is already encoded in the CL vortex-force decomposition. It is the fluctuating component $\mathbf{u}_\phi \times \boldsymbol{\omega}'$, which requires retaining the phase-resolved orbital velocity and adding a statistical-mechanical projection over the bath degrees of freedom.

The wave orbital motion tilts and stretches the slow vorticity $\boldsymbol{\Omega}_s$, generating $\boldsymbol{\omega}_{\text{wave}}$ as a phase-locked oscillation. Taking the curl of (S.6) gives the vorticity equation $\partial_t \boldsymbol{\omega} = \nabla \times [(\mathbf{u}_\phi + \mathbf{u}) \times \boldsymbol{\omega}] + \nu \nabla^2 \boldsymbol{\omega}$. On the fast wave timescale T , $\boldsymbol{\Omega}_s$ is effectively frozen ($T/\tau_{\text{eddy}} \ll 1$). Decomposing $\boldsymbol{\omega} = \boldsymbol{\Omega}_s + \boldsymbol{\omega}_{\text{wave}}$ in the wave-driven term $\nabla \times (\mathbf{u}_\phi \times \boldsymbol{\omega})$, the leading-order contribution is $\nabla \times (\mathbf{u}_\phi \times \boldsymbol{\Omega}_s)$. The feedback $\nabla \times (\mathbf{u}_\phi \times \boldsymbol{\omega}_{\text{wave}})$ is $O(ak)$ relative to this, because $\boldsymbol{\omega}_{\text{wave}}/\boldsymbol{\Omega}_s = O(ak)$. Iterating, it produces corrections to $\boldsymbol{\omega}_{\text{wave}}$ at $O((ak)^2)$ relative to $\boldsymbol{\Omega}_s$. The rotational self-interaction $\nabla \times (\mathbf{u} \times \boldsymbol{\omega})$ is $O(\varepsilon_{\text{CL}})$ relative to the wave-driven term. Both are negligible at leading order. Hence $\partial_t \boldsymbol{\omega}_{\text{wave}} \approx \nabla \times (\mathbf{u}_\phi \times \boldsymbol{\Omega}_s)$. Writing $\mathbf{u}_\phi = \partial_t \boldsymbol{\xi}$ and noting that $\boldsymbol{\Omega}_s$ does not depend on the fast time, the time integration acts only on $\boldsymbol{\xi}$ (with $\nabla \cdot \mathbf{u}_\phi = 0$ and $\nabla \cdot \boldsymbol{\Omega}_s = 0$ simplifying the curl-of-cross product), giving

$$\boldsymbol{\omega}_{\text{wave}} \approx \nabla \times (\boldsymbol{\xi} \times \boldsymbol{\Omega}_s). \quad (\text{S.20})$$

No additional long-wavelength expansion of $\boldsymbol{\Omega}_s$ is required. The derivation is carried out at a fixed Eulerian position, with $\nabla \boldsymbol{\Omega}_s$ treated as the given spatial derivative field wherever it

appears. The only approximation is temporal freezing, with corrections of $O(T/\tau_{\text{eddy}})$. This is the particular (forced) solution of the linearised vorticity equation. It carries no independent degrees of freedom. It is entirely determined by the wave kinematics ($\boldsymbol{\xi}$) and the full slow vorticity $\boldsymbol{\Omega}_s$, and oscillates synchronously with the wave. Because it is linear in $\boldsymbol{\Omega}_s$,

$$\boldsymbol{\omega}_{\text{wave}} = \underbrace{\nabla \times (\boldsymbol{\xi} \times \bar{\boldsymbol{\Omega}})}_{\text{driven by mean vorticity}} + \underbrace{\nabla \times (\boldsymbol{\xi} \times \boldsymbol{\omega}')}_{\text{driven by turbulent vorticity}}. \quad (\text{S.21})$$

The first term is deterministic, the second stochastic but phase-locked to the wave (proportional to $\boldsymbol{\xi}$).

The autonomous turbulent vorticity $\boldsymbol{\omega}' = \boldsymbol{\Omega}_s - \bar{\boldsymbol{\Omega}}$ is driven by local forcing and the turbulent cascade-not by the wave. It therefore carries no dependence on the fast wave phase at a fixed Eulerian position and is approximately frozen over one wave period: $\tau_{\text{eddy}} \sim \ell/u' \gg T$. Statistical independence from the wave phase is a separate statement from this kinematic freezing and follows from the remote origin of swell. For trans-oceanic swell generated by a distant storm, the local realisation of $\boldsymbol{\omega}'$ carries no information about the wave phase at a fixed point on the ray. The local turbulence is driven by local wind, breaking and buoyancy forcing, whereas the swell phase is set by conditions thousands of kilometres away. This physical decoupling underpins the phase-independence assumption A3(ii) formalised in Section S2.

On the wave timescale, $\boldsymbol{\omega}'$ therefore looks the same as $\bar{\boldsymbol{\Omega}}$ in the narrow sense that both are approximately constant during one period T . The critical distinction lies in their *internal structure*:

1. $\bar{\boldsymbol{\Omega}}$ is the ensemble-mean vorticity, a single deterministic vector at each position, with no internal degrees of freedom accessible to the wave. Its contribution to $\boldsymbol{\omega}_{\text{wave}}$ (Eq. S.21) is a periodic oscillation synchronous with the wave phase. Any work done during one half-cycle is returned during the other, yielding zero net energy transfer over a full period.
2. $\boldsymbol{\omega}'$, by contrast, is a full turbulent field possessing its own internal degrees of freedom, including the full hierarchy of the turbulent cascade and local forcing. Although $\boldsymbol{\omega}'$ is approximately frozen on the wave timescale, its internal dynamics continuously redistribute energy among its modes on the eddy-turnover time ℓ/u' . During a single wave period, a small fraction $T u'/\ell \sim \mathcal{O}(10^{-2})$ of any energy injected by the wave into an eddy is redistributed among the eddy's internal modes before the wave phase returns to its original value. This small but nonzero redistribution prevents exact energy return.

This distinction-the presence or absence of internal degrees of freedom-is the microscopic origin of irreversibility in the SVF theory, analogous to the distinction between elastic scattering off a rigid wall and inelastic scattering off a thermal-bath molecule (Section S2 I).

The connection between the wave-slaved coupling and the Stokes-drift form used in CL theory is established by the McWilliams identity [6, Appendix G]. For any solenoidal field \boldsymbol{Z} that is independent of the fast wave phase (i.e. varies only on timescales $\gg T$),

$$\langle \boldsymbol{u}_\phi \times [\nabla \times (\boldsymbol{\xi} \times \boldsymbol{Z})] \rangle_\phi = \boldsymbol{u}_s \times \boldsymbol{Z} + \nabla C, \quad (\text{S.22})$$

where C is a scalar field. The identity rectifies a quadratic wave-phase correlation into the Stokes-drift form. It is linear in \boldsymbol{Z} and relies on small slope, incompressibility, and phase-independence of \boldsymbol{Z} [6, Appendix G]. To verify (S.22), one expands $\nabla \times (\boldsymbol{\xi} \times \boldsymbol{Z})$ via the BAC-CAB identity, takes the cross product with \boldsymbol{u}_ϕ , and phase-averages term by term using the explicit orbital velocity (S.11). The key step is that the second-order correlator $\langle u_i^\phi \partial_j \xi_k \rangle_\phi$ evaluates, by direct calculation with the deep-water eigenfunction, to a combination of Stokes-drift components and gradient corrections. Collecting terms yields the right-hand side of (S.22). A self-contained proof occupies approximately two pages of vector algebra and is given in McWilliams [6, Appendix G].

Remark 1 (Assumptions behind the McWilliams identity). *Identity (S.22) is a kinematic consequence of wave-period averaging of quadratic wave quantities. It requires only that \mathbf{Z} be solenoidal and independent of the fast wave phase, so that it may be treated as frozen in time during the one-period phase average. No additional weak-spatial-variation assumption is required for the identity itself beyond the conditions stated in McWilliams [6, Appendix G]. Any spatial dependence of \mathbf{Z} enters only through gradient terms that are absorbed into ∇C . Since $\nabla \times (\nabla C) = \mathbf{0}$, such terms do not affect the vorticity forcing. The fact that the residual term indeed takes pure gradient form is proved in McWilliams [6, Appendix G, Eq. (G.7)] for any non-divergent \mathbf{Z} . Separately, the approximation (S.20) for the wave-slaved vorticity relies on temporal scale separation ($\partial_t \Omega_s$ negligible over one wave period), with corrections controlled by T/τ_{slow} for the relevant slow component.*

Setting $\mathbf{Z} = \Omega_s = \bar{\Omega} + \omega'$ in (S.22) and using (S.20),

$$\langle \mathbf{u}_\phi \times \omega_{\text{wave}} \rangle_\phi \equiv \nabla \mathbf{u}_s \times \Omega_s = \mathbf{u}_s \times \bar{\Omega} + \mathbf{u}_s \times \omega'. \quad (\text{S.23})$$

The first term, $\mathbf{u}_s \times \bar{\Omega}$, is the deterministic CL vortex force driving Langmuir circulations [11, 12]. The second, $\mathbf{u}_s \times \omega'$, is a slow stochastic contribution. The full phase-averaged force $\mathbf{u}_s \times \Omega_s$ modifies the mean flow on time scales $\gg T$ but carries no power at the swell frequency ω and thus does not, by itself, damp the wave mode. (A separate, direction-dependent CL energy pathway $\propto \cos \Delta\theta$ exists in wind seas but is expected to be small in path mean for remote swell owing to sign cancellations, see Section S9.)

The identity (S.23) and the wave-slaved vorticity (S.20) have been independently verified by wave-resolving simulation [13], which solved the full Navier-Stokes equations without invoking CL averaging. In our notation, their mean-vorticity analysis confirms that the wave-induced torque $\nabla \times \langle \mathbf{u}_\phi \times \omega_{\text{wave}} \rangle_\phi$ agrees with the curl of the vortex force $\nabla \times (\mathbf{u}_s \times \Omega_s)$ to correlation coefficients exceeding 0.99, and that ω_{wave} is produced by tilting and stretching of the slow vorticity Ω_s by wave motion, consistent with (S.20).

E. Identification of the stochastic vortex force

Substituting the three-layer decomposition (S.19) into the orbital vortex force (S.7) separates three physically distinct couplings. Interaction with the ensemble-mean vorticity $\bar{\Omega}$, with the wave-slaved vorticity ω_{wave} , and with the autonomous turbulent fluctuation ω' . The turbulent fluctuation ω' participates in two of these. First, wave orbital motion acting on ω' generates a component of the wave-slaved vorticity $\omega_{\text{wave}} = \nabla \times (\boldsymbol{\xi} \times \Omega_s)$ (Term II below). The resulting phase-averaged force is the zero-frequency CL contribution $\mathbf{u}_s \times \omega'$, which does not project onto the wave mode. Second, ω' couples directly to the oscillating orbital velocity through $\mathbf{u}_\phi \times \omega'$ (Term III below). This force has zero phase mean but nonzero autocorrelation, and constitutes the microscopic coupling analysed in Sections S2-S5. The three-term split is,

$$\mathbf{f}_v = \mathbf{u}_\phi \times \omega = \underbrace{\mathbf{u}_\phi \times \bar{\Omega}}_{\text{Term I}} + \underbrace{\mathbf{u}_\phi \times \omega_{\text{wave}}}_{\text{Term II}} + \underbrace{\mathbf{u}_\phi \times \omega'}_{\text{Term III}}. \quad (\text{S.24})$$

We evaluate the phase average of each term in turn. For Term I, $\bar{\Omega}$ is slowly varying. By (S.14) and (S.12),

$$\langle \mathbf{u}_\phi \times \bar{\Omega} \rangle_\phi = \mathbf{0}. \quad (\text{S.25})$$

For Term II, the McWilliams identity (S.23) gives

$$\langle \mathbf{u}_\phi \times \omega_{\text{wave}} \rangle_\phi \equiv \nabla \mathbf{u}_s \times \Omega_s = \mathbf{u}_s \times \bar{\Omega} + \mathbf{u}_s \times \omega'. \quad (\text{S.26})$$

For Term III, ω' is slowly varying on the wave timescale ($\tau_{\text{eddy}} \gg T$). By the slow-field extraction rule,

$$\langle \mathbf{u}_\phi \times \omega' \rangle_\phi = \langle \mathbf{u}_\phi \rangle_\phi \times \omega' + O(T/\tau_{\text{eddy}}) = \mathbf{0} \times \omega' + O(T/\tau_{\text{eddy}}) = O(T/\tau_{\text{eddy}}), \quad (\text{S.27})$$

so its phase average vanishes to leading order. This vanishing is a *kinematic* consequence of the slow-field extraction rule and $\langle \mathbf{u}_\phi \rangle_\varphi = \mathbf{0}$ and it holds regardless of how $\boldsymbol{\omega}'$ was generated. The deeper requirement—that $\boldsymbol{\omega}'$ be *statistically independent* of the wave phase, not merely slow-enters only at the ensemble level in the Green-Kubo analysis of Section S2 (Assumption A3(ii)). Collecting the three results,

$$\langle \mathbf{f}_v \rangle_\varphi \equiv \nabla \mathbf{u}_s \times \boldsymbol{\Omega}_s, \quad (\text{S.28})$$

recovering the classical CL result. On time scales long compared with the wave period, the net effect of the orbital motion on the slow flow is the CL vortex force.

All three terms in (S.24) have zero or slow phase averages, so the question of irreversibility cannot be resolved at the level of first-order (mean-force) diagnostics. Whether swell is damped or not depends on the cumulative work done by the *fluctuating* part of the force as the wave packet propagates through the turbulent field. We therefore examine each term’s capacity for net energy transfer on the wave timescale.

Mean-vorticity term ($\mathbf{u}_\phi \times \bar{\boldsymbol{\Omega}}$). $\bar{\boldsymbol{\Omega}}$ has no accessible internal degrees of freedom. Its coupling to the orbital motion therefore produces a phase-locked, reversible response. At leading order it renormalises the wave frequency, but does not contribute to the dissipative Green-Kubo real part that defines the mode-level damping rate.

Wave-slaved term ($\mathbf{u}_\phi \times \boldsymbol{\omega}_{\text{wave}}$). The wave-slaved vorticity $\boldsymbol{\omega}_{\text{wave}} = \nabla \times (\boldsymbol{\xi} \times \boldsymbol{\Omega}_s)$ carries no independent degrees of freedom at leading order. The retained wave-slaved contribution is fully determined by the instantaneous wave kinematics and the frozen slow field, leaving no autonomous bath-like dynamics that could generate irreversible redistribution of energy. Because both \mathbf{u}_ϕ and $\boldsymbol{\omega}_{\text{wave}}$ oscillate at the wave frequency ω , their product has spectral support at leading order only at frequencies 0 and 2ω . (For a narrowband wave packet with slowly modulated envelope, the spectral leakage away from 0 and 2ω is higher order and does not generate a secular component at ω to leading order.) The slow (0-frequency) component is precisely the CL force $\mathbf{u}_s \times \boldsymbol{\Omega}_s$, which modifies the mean-flow evolution on timescales $\gg T$ but carries no spectral weight at the swell frequency ω and therefore cannot contribute to the Green-Kubo damping rate of that wave mode. The 2ω component likewise has no projection onto the swell mode. Term II therefore cannot contribute to the mode-level damping rate.

Turbulent-fluctuation term ($\mathbf{u}_\phi \times \boldsymbol{\omega}'$). By contrast, $\boldsymbol{\omega}'$ possesses internal degrees of freedom that prevent exact reversal (as discussed in Section D and quantified in Section S6). Furthermore, as the swell propagates at $c_g \sim 10\text{--}15 \text{ m s}^{-1}$, it successively encounters statistically independent turbulent regions, providing a finite decorrelation length along the ray. Within this decomposition, Term III is the only component that possesses both ingredients for irreversible energy transfer. It has internal degrees of freedom, preventing exact reversal over a cycle, and spatial decorrelation, preventing coherent cancellation over many cycles. The two ingredients play distinct roles. Spatial decorrelation controls the *magnitude* of the damping rate by setting the Green-Kubo convergence time. The internal evolution of $\boldsymbol{\omega}'$ guarantees its *sign* (Section I). Within the present bulk, non-breaking, potential-wave framework, Term III is the unique candidate for irreversible swell attenuation. We define the *stochastic vortex force* (SVF),

$$\boxed{\mathbf{f}_{\text{svf}} \equiv \mathbf{u}_\phi \times \boldsymbol{\omega}'}. \quad (\text{S.29})$$

The statistical-mechanical framework of Section S2 formalises this picture. Projecting the full dynamics onto the swell subspace via the Mori-Zwanzig formalism identifies the orthogonal (noise) force that drives the memory kernel. Under the scale-separation and statistical-decoupling assumptions A2-A4, this projected force reduces precisely to the SVF,

$$F_{\mathbf{k}}(t) = [Q(\mathbf{u}_\phi \times \boldsymbol{\omega})]_{\mathbf{k}} \longrightarrow [\mathbf{u}_\phi \times \boldsymbol{\omega}']_{\mathbf{k}}, \quad (\text{S.30})$$

where $Q = 1 - P$ is the orthogonal projector in the Hilbert space of observables and the arrow denotes the identification that holds under Assumptions A2-A4 (not an algebraic identity). The discarded contributions are absorbed into the streaming term and into gradient/solenoidal forces whose net work on the swell mode vanishes.

A deliberate choice underlies the derivation. We keep a phase-resolved *Eulerian* description rather than working directly in the Generalised Lagrangian Mean (GLM) framework of classical Craik-Leibovich theory. GLM absorbs wave effects into Lagrangian-mean quantities and yields the phase-averaged CL vortex force ($\mathbf{u}_s \times \boldsymbol{\Omega}_s$), while practical mean-flow applications often focus on its ensemble-mean component ($\mathbf{u}_s \times \bar{\boldsymbol{\Omega}}$). Here our target is different. The irreversible attenuation arises from the *fluctuating* coupling $\mathbf{f}_{\text{svf}} = \mathbf{u}_\phi \times \boldsymbol{\omega}'$. This term has zero phase mean and is therefore absent from the mean CL force, yet its *two-time* autocorrelation determines the friction coefficient via the Green-Kubo formula. Retaining the wave-slaved response $\boldsymbol{\omega}_{\text{wave}}$ and the instantaneous force \mathbf{f}_{svf} makes the subsequent statistical closure and the link to observations explicit.

S2. Non-negativity of the Green-Kubo damping coefficient

This section proves that $\Gamma(\mathbf{k}) \geq 0$ for any surface gravity wave propagating through turbulence, using the Green-Kubo relation [14, 15]

$$\Gamma(\mathbf{k}) = \frac{1}{2E_{\mathbf{k}}} \int_0^\infty \text{Re} \langle F_{\mathbf{k}}(0) F_{\mathbf{k}}^*(\tau) \rangle d\tau, \quad (\text{S.31})$$

where $F_{\mathbf{k}}$ is the mode-projected stochastic vortex force identified in Section S1 and connected to the Mori-Zwanzig formalism below. The inequality follows from Bochner's theorem [16] and holds regardless of the bath spectrum $E_\omega(q)$. The quantitative evaluation is carried out in Sections S3-S5. We retain the notation of Section S1: $\langle \cdot \rangle_\varphi$ for the wave-phase average, $\langle \cdot \rangle$ for the ensemble average over the stationary bath measure ρ_{ss} .

A. Assumptions A1-A6

To connect the microscopic SVF to a coarse-grained damping rate we make six assumptions. We first state them in compact form. The subsequent discussion gives physical motivation and typical values (verified a posteriori).

A1 (Resolved wave band). There exists a narrow band \mathcal{B} of swell wavenumbers such that each $\mathbf{k} \in \mathcal{B}$ admits a linear dispersion relation $\omega(\mathbf{k})$ and a complex amplitude $a_{\mathbf{k}}(t)$, with modal energy

$$E_{\mathbf{k}}(t) \equiv \frac{1}{2} |a_{\mathbf{k}}(t)|^2. \quad (\text{S.32})$$

Ensemble averages $\langle \cdot \rangle$ act on the bath degrees of freedom $\boldsymbol{\omega}'$ at fixed $\{a_{\mathbf{k}}\}$. When needed, a further average over wave realisations is denoted explicitly. Nonlinear wave-wave interactions are negligible on the attenuation time scale Γ^{-1} for far-field swell [17].

A2 (Time-scale separation). The force autocorrelation decays on a correlation time τ_c much shorter than the attenuation time,

$$\tau_c \ll \Gamma(\mathbf{k})^{-1} \quad \text{for all } \mathbf{k} \in \mathcal{B}. \quad (\text{S.33})$$

A3 (Bath statistics and phase decoupling). Three sub-conditions on the autonomous turbulent vorticity $\boldsymbol{\omega}'$:

- (i) *Local stationarity and homogeneity.* The statistics of $\boldsymbol{\omega}'$ are stationary and translation-invariant within analysis patches of size $O(k^{-1})$; the slow along-ray variation of the bath parameters is treated by a local closure (Section S5 E).

(ii) *Phase decoupling.* The statistics of $\boldsymbol{\omega}'$ are independent of the swell phase.

(iii) *Zero ensemble mean.* $\langle \boldsymbol{\omega}' \rangle_{\rho_{\text{bath}}} = \mathbf{0}$.

A4 (Linear truncation in wave amplitude). The SVF enters the amplitude equation at first order in $\{a_{\mathbf{k}}\}$. Feedback terms of order $|a_{\mathbf{k}}|^2$ can be neglected.

A5 (Locally stationary reference measure). Two sub-conditions:

(i) *Local stationarity.* For each fixed value of the resolved wave amplitudes $\{a_{\mathbf{k}}\}$ (treated as quasi-constant over $\tau \lesssim \tau_c$), the mixed-layer turbulence admits a locally stationary reference measure $\rho_{\text{bath}}(\boldsymbol{\omega}')$ over the support of the memory kernel.

(ii) *Factorisation.* The full reference measure factorises approximately into independent wave and bath parts:

$$\rho_{\text{ss}}(\{a_{\mathbf{k}}\}, \boldsymbol{\omega}') \approx \rho_{\text{wave}}(\{a_{\mathbf{k}}\}) \rho_{\text{bath}}(\boldsymbol{\omega}'). \quad (\text{S.34})$$

No equilibrium-specific properties (Boltzmann form, detailed balance, equipartition) are imposed. The NESS structure is discussed in Section B. No global stationary measure for the coupled wave-turbulence system is assumed. The wave amplitude is quasi-frozen over $\tau \lesssim \tau_c$ ($\Gamma \tau_c \sim 10^{-6}$ - 10^{-4}), making $C_F(\tau)$ and the Mori-Zwanzig inner product well-defined to leading order in δ .

A6 (Finite memory). The mode-projected SVF has an absolutely integrable autocorrelation, so that the Green-Kubo integral converges.

The physical origin of τ_c in A2 is advective phase decorrelation along the wave-energy trajectory. For a $T = 15$ s swell ($k \approx 0.018 \text{ m}^{-1}$, $c_g \approx 11.7 \text{ m s}^{-1}$), the dominant coupling is with eddies of scale $\ell \sim k^{-1} \approx 56$ m (Section S3 F). As the wave-energy trajectory advances at c_g , the mode-projected force from a turbulent mode at wavenumber q acquires an advected phase $\exp(i\mathbf{q} \cdot \mathbf{c}_g t)$. At the dominant scale $q \sim k$ this phase reaches $O(1)$ in $\tau_{\text{adv}} \sim 1/(k c_g) \approx 4.8$ s, after which successive eddy-scale patches contribute to the Green-Kubo integral with randomised phases. The decorrelation is spatial in origin. The wave-energy trajectory advances through a spatially incoherent turbulent field, not a temporally evolving one. Irreversibility requires the eddy's internal degrees of freedom to evolve during the encounter ($\delta = \tau_c/\tau_{\text{eddy}} > 0$, Section I). Over the attenuation time $\Gamma^{-1} \sim 10^5$ - 10^6 s, the packet encounters $\Gamma^{-1}/\tau_c \sim 10^4$ - 10^5 eddies in sequence along its ray. A2 is not needed for the inequality $\Gamma \geq 0$, which follows from Bochner's theorem alone. It enters when interpreting Γ as the rate of exponential decay in the Markovian limit.

Assumption A3 draws on the three-layer decomposition of Sec. S1: $\boldsymbol{\omega} = \bar{\boldsymbol{\Omega}} + \boldsymbol{\omega}' + \boldsymbol{\omega}_{\text{wave}}$, with $\boldsymbol{\Omega}_s = \bar{\boldsymbol{\Omega}} + \boldsymbol{\omega}'$ the phase-averaged (slow) vorticity. Sub-condition A3(i) requires that the vorticity statistics be translation-invariant within each analysis patch of size $O(k^{-1})$. With this local homogeneity the SVF correlation takes the form

$$\langle \mathbf{f}_{\text{svf}}(\mathbf{x}, t) \otimes \mathbf{f}_{\text{svf}}(\mathbf{x}', t') \rangle = \mathbf{C}_f(\mathbf{x} - \mathbf{x}', t - t'). \quad (\text{S.35})$$

Sub-condition A3(ii), the phase decoupling, follows from the remote origin of swell (as discussed in Sec. S1). Even when swell-driven Stokes drift modifies the local turbulence—for instance by driving Langmuir circulations—this modification depends only on the phase-averaged Stokes drift $\mathbf{u}_s \propto |a_{\mathbf{k}}|^2 \omega_{\mathbf{k}} e^{2kz}$, a second-order quantity that carries no information about the instantaneous wave phase. The turbulence statistics may therefore depend on the swell *amplitude* (a higher-order effect addressed under A4) but remain independent of the swell *phase*, which is set by conditions thousands of kilometres away. The observed amplitude-independence of attenuation rates [18, 19] provides empirical confirmation of this decoupling. Sub-condition A3(iii), the zero ensemble mean, holds by definition of the Reynolds decomposition $\boldsymbol{\omega}' = \boldsymbol{\Omega}_s - \bar{\boldsymbol{\Omega}}$ (Section S1, Eq. S.18).

The SVF $\mathbf{f}_{\text{svf}} = \mathbf{u}_\phi \times \boldsymbol{\omega}'$ vanishes under both the phase average (because $\langle \mathbf{u}_\phi \rangle_\varphi = \mathbf{0}$) and the ensemble average (because $\langle \boldsymbol{\omega}' \rangle = \mathbf{0}$), as required for a fluctuating force in the Mori-Zwanzig sense.

The coupling parameter in A4 is $\delta \equiv u'/c_g$ (formally defined in Eq. S.71 below), where u' is a typical turbulent velocity at the eddy scale $\ell \sim k^{-1}$ that couples most strongly to the swell (Sec. S3) and c_g is the group velocity. For far-field swell, $\delta \sim 10^{-3}$ - 10^{-2} . Two estimates confirm the validity of the linear truncation. First, per-encounter linearity. Over one correlation time $\tau_c \sim 5$ s the fractional amplitude change is $\Gamma\tau_c \sim 10^{-6} \text{ s}^{-1} \times 5 \text{ s} \sim 5 \times 10^{-6}$ (the value $\Gamma \sim 10^{-6} \text{ s}^{-1}$ follows from the closed-form evaluation in Sections S3-S5), well inside the linear-response regime. Nonlinear corrections enter at $\mathcal{O}(\delta^2) \sim 10^{-6}$ - 10^{-4} . Second, the weak-probe condition. The total power extracted from the swell, $\dot{W} \sim 2\Gamma E_w \sim 5 \times 10^{-3} \text{ W m}^{-2}$ for typical far-field amplitudes ($H_s \sim 2$ m), is two orders of magnitude below the ~ 0.1 - 1 W m^{-2} supplied to the mixed-layer turbulent bath by wind-wave breaking, current shear and Langmuir circulations [20–22]. Since $\dot{W} \propto H_s^2$, the weak-probe condition is comfortably satisfied for the far-field swell regime $H_s \lesssim 5$ m considered throughout this work. Near-storm conditions ($H_s \gtrsim 10$ m) violate A4 together with A1 and A3(ii).

Assumption A5 posits the existence of at least one stationary measure $\rho_{\text{ss}}(\{a_{\mathbf{k}}\}, \boldsymbol{\omega}')$ for the wind-driven mixed layer, maintained in a statistically steady state by the balance of forcing and dissipation. Correlation functions under ρ_{ss} are time-translation invariant on the support of the memory kernel ($\sim \tau_c$). The measure factorises to good approximation as in Eq. (S.34), reflecting the negligible back-reaction of remote-source swell on local turbulence. The mode-projected stochastic force in A6,

$$F_{\mathbf{k}}(t) = \int d^3\mathbf{x} \psi_{\mathbf{k}}^*(\mathbf{x}) \cdot \mathbf{f}_{\text{svf}}(\mathbf{x}, t), \quad (\text{S.36})$$

is defined by expanding the wave velocity field onto the linear deep-water eigenfunctions, $\mathbf{u}_\phi(\mathbf{x}, t) = \sum_{\mathbf{k} \in \mathcal{B}} a_{\mathbf{k}}(t) \boldsymbol{\psi}_{\mathbf{k}}(\mathbf{x}) + \text{c.c.}$, with normalisation chosen such that $E_{\mathbf{k}} = \frac{1}{2}|a_{\mathbf{k}}|^2$. For deep-water surface gravity waves the linearised operator is self-adjoint under the energy inner product, so $\boldsymbol{\psi}_{\mathbf{k}}$ serves simultaneously as the eigenfunction and its adjoint. The projection (S.36) is therefore unambiguous. The memory kernel is diagonal in wavevector as a consequence of the translational invariance of the bath statistics (A3(i)) and the Fourier structure of the mode functions. Cross-correlations $\langle F_{\mathbf{k}} F_{\mathbf{k}'}^* \rangle$ vanish for $\mathbf{k} \neq \mathbf{k}'$. The mode-projected force has an absolutely integrable autocorrelation

$$\int_0^\infty |\langle F_{\mathbf{k}}(0) F_{\mathbf{k}}(\tau)^* \rangle| d\tau < \infty. \quad (\text{S.37})$$

By stationarity, $C_F(-\tau) = C_F(\tau)^*$, so half-axis integrability implies $C_F \in L^1(\mathbb{R})$ and the Fourier transform $S_F(\omega)$ is well defined. The physical mechanism ensuring rapid convergence is the same advective phase decorrelation discussed under A2. Sweeping at $c_g \gg u'$ suppresses long-time tails (cf. the $t^{-3/2}$ Alder-Wainwright tails of molecular fluids [23]), placing the system deep in the Markovian regime. Assumptions A1, A3(i), A5(i) and A6 are the structural inputs to the non-negativity theorem. A2, A3(ii) and A4 enter later, when we pass from the generalised Langevin equation to a Markovian damping rate and to pathwise statistics. A5(ii) enters in the cancellation of probe energy from Γ (Section C.4). None of these assumptions refers to the specific form of the bath spectrum $E_\omega(q)$. The non-negativity theorem is therefore independent of whether the turbulence is in the inertial range, the viscous range, or a transitional regime.

Remark 2 (Swell-driven Langmuir feedback and the weak-probe condition). *The weak-probe estimates in A4 show that far-field swell extracts at most a few percent of the bath TKE input. A subtler back-reaction channel is the modification of ε through swell-Stokes-drift-driven Langmuir turbulence. In moderate winds, the swell band contributes $\lesssim \mathcal{O}(10\%)$ of the total near-surface u_s [22, 24]. In light winds this fraction can be larger, and even when the surface fraction is small the swell Stokes drift penetrates to depths $\sim 1/(2k) \sim 30$ m, well below the wind-wave*

contribution. The relevant question is not whether swell modifies ε , but whether that modification depends on swell amplitude—and thereby introduces a nonlinear feedback on Γ . Since the Stokes drift scales as $u_s \propto |a_k|^2$, any such feedback enters at $\mathcal{O}(|a_k|^2)$ relative to the leading-order SVF coupling, consistent with the A_4 truncation. The observed amplitude-independence of attenuation rates [18, 19] confirms that this feedback is negligible in the far-field regime.

B. Non-equilibrium steady states and FDR-II

The Mori-Zwanzig projection starts from a stationary measure ρ_{ss} , defines an inner product

$$\langle A, B \rangle_\rho = \int A(\mathbf{X}) B^*(\mathbf{X}) \rho_{\text{ss}}(\mathbf{X}) d\mathbf{X}, \quad (\text{S.38})$$

and constructs the orthogonal projector \mathcal{P} onto the chosen slow subspace. The derivation of the generalised Langevin equation and of the second fluctuation-dissipation relation uses only the algebra of \mathcal{P} and $\mathcal{Q} = 1 - \mathcal{P}$ and the stationarity of ρ_{ss} , not its functional form or any symmetry of the Liouville operator [25, 26]. In particular, the second fluctuation-dissipation relation (FDR-II),

$$K_{\mathbf{k}}(\tau) = \frac{\langle F_{\mathbf{k}}(0) F_{\mathbf{k}}(\tau)^* \rangle}{\langle |a_{\mathbf{k}}|^2 \rangle_{\text{ref}}}, \quad (\text{S.39})$$

holds for any stationary measure, whether equilibrium or driven-dissipative. It follows from the algebra of the Mori-Zwanzig projectors alone. The construction uses only two properties. First, the self-adjointness of \mathcal{P} under $\langle \cdot, \cdot \rangle_\rho$ ($\langle \mathcal{P}A, B \rangle_\rho = \langle A, \mathcal{P}B \rangle_\rho$), which holds by construction as an orthogonal projection. Second, the time-translation invariance of correlation functions under ρ_{ss} , which requires only \mathcal{L} -invariance of the measure, not detailed balance or self-adjointness of \mathcal{L} [25, 26]. The local forcing-driven mixed layer is a mechanically forced NESS in the sense of Evans and Morriss [27]. Analogous Green-Kubo relations have been validated in mechanically driven fluids [27, 28] and active-matter systems [29, 30]. The stationarity required here is only local in time. ρ_{ss} must be time-translation invariant over the support of the memory kernel ($\sim \tau_c$), not over the full swell propagation time. Section D shows that this condition is satisfied with four orders of magnitude of margin ($\tau_c/\tau_{\text{NESS}} \sim 10^{-4}$), even in the most conservative climate zone along the ray.

C. Operational construction of the reference measure

The Mori-Zwanzig formalism requires an inner product weighted by ρ_{ss} but not its explicit functional form. For swell, three properties are sufficient. Stationarity, factorisation into wave and bath sectors, and finite second moments of the bath vorticity.

C.1. Factorisation and orthogonality

Remote swell and local turbulence are forced by independent mechanisms. The factorisation (S.34) expresses the negligible back-reaction of remote-source swell on local turbulence. Under this factorisation, the orthogonality required by the projection formalism follows directly,

$$\langle F_{\mathbf{k}} a_{\mathbf{k}}^* \rangle = \langle a_{\mathbf{k}}^* \underbrace{\langle F_{\mathbf{k}} \rangle_{\rho_{\text{bath}}}}_{=0} \rangle_{\rho_{\text{wave}}} = 0, \quad (\text{S.40})$$

since $F_{\mathbf{k}}$ is linear in $\boldsymbol{\omega}'$ and $\langle \boldsymbol{\omega}' \rangle_{\rho_{\text{bath}}} = \mathbf{0}$ (A3(iii)). Orthogonality thus reflects the physical decoupling between swell and bath, rather than an additional postulate.

C.2. Bath sector: second-order vorticity statistics

The Green-Kubo numerator involves the force autocorrelation

$$C_F(\tau) = \left\langle \int d^3\mathbf{x} \boldsymbol{\psi}_{\mathbf{k}}^* \cdot (\mathbf{u}_\phi \times \boldsymbol{\omega}')(\mathbf{x}, 0) \int d^3\mathbf{x}' \boldsymbol{\psi}_{\mathbf{k}} \cdot (\mathbf{u}_\phi \times \boldsymbol{\omega}')^*(\mathbf{x}', \tau) \right\rangle. \quad (\text{S.41})$$

Given the wave field \mathbf{u}_ϕ , this depends on ρ_{bath} only through the second-order vorticity statistics. For locally isotropic turbulence—an assumption justified within the ocean mixed layer in Section S5 G and implicit throughout the spectral evaluation of Sections S3-S5—the vorticity covariance takes the solenoidal form

$$\langle \omega'_i(\mathbf{q}) \omega'^*_j(\mathbf{q}') \rangle_{\rho_{\text{bath}}} = \frac{E_\omega(q)}{4\pi} (\delta_{ij} - \hat{q}_i \hat{q}_j) \delta(\mathbf{q} - \mathbf{q}'), \quad (\text{S.42})$$

where $E_\omega(q) = q^2 E_u(q)$ and $E_u(q) = 4\pi q^2 S_u(q)$ is the isotropic one-dimensional velocity spectrum, normalised so that $\int_0^\infty E_u(q) dq = \frac{1}{2} \langle |\mathbf{u}'|^2 \rangle$. The prediction chain therefore closes as

$$E_\omega(q) \longrightarrow C_F(\tau; \mathbf{k}) \longrightarrow S_F(0; \mathbf{k}) \longrightarrow \Gamma(\mathbf{k}), \quad (\text{S.43})$$

once $E_\omega(q)$ is specified. No higher-order vorticity statistics are needed. The full complexity of the turbulent bath is filtered through a single spectral function. Unlike the pair correlation function $g(r)$ required in the analogous Green-Kubo integral for simple-liquid viscosity [31], the turbulent vorticity spectrum $E_\omega(q)$ in the inertial range is fixed by the Kolmogorov cascade [32] to $E_\omega(q) \propto \varepsilon^{2/3} q^{1/3}$. No closure beyond the Kolmogorov inertial-range spectrum is needed (Sec. S4).

C.3. What we need from ρ_{wave} . Externally prescribed modal energy

The denominator of FDR-II (S.39) is the reference modal energy $\langle |a_{\mathbf{k}}|^2 \rangle_{\text{ref}} = 2E_{\mathbf{k}}$, prescribed by the remote storm, not by the local bath. Probe and bath are parameterised by independent energy scales— $E_{\mathbf{k}}$ and ε —so $E_{\mathbf{k}}$ cancels exactly from Γ (Section C.4).

C.4. Independence of the damping rate from probe energy

Although both numerator and denominator of (S.31) depend on $E_{\mathbf{k}}$, the dependence cancels exactly when linear coupling and statistical decoupling both hold. The stochastic vortex force is bilinear: $\mathbf{f}_{\text{svf}} = \mathbf{u}_\phi \times \boldsymbol{\omega}'$, with $\mathbf{u}_\phi \propto a_{\mathbf{k}}$. Under the linear truncation (A4), the mode-projected force inherits this linearity: $F_{\mathbf{k}} \propto a_{\mathbf{k}}$. Over the short correlation window $\tau \lesssim \tau_c$ the amplitude varies negligibly (A2 and Eq. (S.49)), so that $a_{\mathbf{k}}(0)a_{\mathbf{k}}^*(\tau) \approx |a_{\mathbf{k}}|^2$ within the Green-Kubo integral. Factorisation A5(ii) then permits the numerator to be decomposed as

$$\langle F_{\mathbf{k}}(0) F_{\mathbf{k}}^*(\tau) \rangle = \langle |a_{\mathbf{k}}|^2 \rangle \times \mathcal{G}_{\mathbf{k}}(\tau), \quad (\text{S.44})$$

where $\mathcal{G}_{\mathbf{k}}(\tau)$ depends only on the bath vorticity statistics and the mode geometry (wave polarisation $\boldsymbol{\psi}_{\mathbf{k}}$ and wavenumber k), but not on $E_{\mathbf{k}}$. Substituting (S.44) into (S.31) and noting $\langle |a_{\mathbf{k}}|^2 \rangle = 2E_{\mathbf{k}}$ gives

$$\Gamma(\mathbf{k}) = \frac{1}{2E_{\mathbf{k}}} \int_0^\infty \text{Re}[\langle |a_{\mathbf{k}}|^2 \rangle \mathcal{G}_{\mathbf{k}}(\tau)] d\tau = \int_0^\infty \text{Re}[\mathcal{G}_{\mathbf{k}}(\tau)] d\tau. \quad (\text{S.45})$$

We define

$$K_{\mathbf{k}}(\tau) \equiv \frac{\langle F_{\mathbf{k}}(0) F_{\mathbf{k}}(\tau)^* \rangle}{2E_{\mathbf{k}}} = \mathcal{G}_{\mathbf{k}}(\tau), \quad \Gamma(\mathbf{k}) = \int_0^\infty \text{Re}[K_{\mathbf{k}}(\tau)] d\tau, \quad (\text{S.46})$$

independent of the wave energy. Both assumptions are essential. If the SVF entered at second order ($F_{\mathbf{k}} \propto |a_{\mathbf{k}}|^2$), the numerator would scale as $E_{\mathbf{k}}^2$, making the memory kernel $K_{\mathbf{k}} \propto E_{\mathbf{k}}$ and the damping rate probe-dependent—the nonlinear-microrheology regime. Likewise, if the bath statistics depended on the surface wave energy, $\mathcal{G}_{\mathbf{k}}$ would carry an implicit $E_{\mathbf{k}}$ -dependence and the cancellation would be incomplete. For trans-oceanic swell both conditions hold with large margins (Remark 2).

D. Time-scale separation and local validity

The Green-Kubo formula (defined formally in Section F below, Eq. S.58) is derived under a stationary reference measure, yet the swell amplitude decays along the ray at rate Γ . As noted in A5, no joint global steady state of $(\{a_{\mathbf{k}}\}, \omega')$ exists. The resolution rests on a three-level time-scale hierarchy and on a local application of the Green-Kubo relation. The force autocorrelation $C_F(\tau)$ is supported on $\tau_c \sim 5$ s (A2). For the Green-Kubo integral to be evaluated under a locally stationary bath, the turbulent statistics—principally the dissipation rate ε —must remain approximately constant over each such window. The relevant time scale is the *persistence* time τ_{NESS} , i.e. the time over which the wind-driven mixed layer maintains its current statistical state at a fixed point on the ocean surface. A trans-oceanic swell ray typically spans 10 000–15 000 km and traverses several distinct climate zones: the mid-latitude storm belt where the swell is generated, the subtropical high-pressure belt, the trade-wind region, and possibly the opposite-hemisphere storm track. Among these, the shortest persistence arises in the mid-latitude storm tracks, where synoptic-scale weather systems have characteristic horizontal extent $L_{\text{syn}} \sim 10^3$ km and propagation speed $V_{\text{syn}} \sim 10$ m s⁻¹ [33], giving

$$\tau_{\text{NESS}} \sim \frac{L_{\text{syn}}}{V_{\text{syn}}} \sim \frac{10^6 \text{ m}}{10 \text{ m s}^{-1}} \sim 10^5 \text{ s} \sim 1 \text{ day}. \quad (\text{S.47})$$

In the trade-wind belt and subtropical highs, surface wind conditions persist on time scales of weeks or longer, so the mid-latitude estimate provides a *lower bound* on τ_{NESS} along the entire ray. Even this most conservative value yields

$$\frac{\tau_c}{\tau_{\text{NESS}}} \sim 10^{-4}, \quad (\text{S.48})$$

providing four orders of magnitude of margin. Over each short correlation window the bath may be treated as stationary, with an ε that is effectively constant on that window. The same hierarchy applied to the wave sector ensures that $E_{\mathbf{k}}$ is quasi-constant over each correlation window. The fractional energy change per window is

$$\tau_c \Gamma \lesssim 10^{-5} \quad (\text{using } \Gamma \sim 10^{-6} \text{ s}^{-1} \text{ from Sections S3-S5}), \quad (\text{S.49})$$

analogous to the Born-Oppenheimer separation of fast and slow degrees of freedom. Locally in time, we evaluate $\Gamma(\mathbf{k}; \varepsilon)$ from the instantaneous bath state and interpret it as the coefficient in a local equation

$$\frac{dE_{\mathbf{k}}}{dt} = -2\Gamma(\varepsilon(t), \mathbf{k}) E_{\mathbf{k}}(t), \quad (\text{S.50})$$

which is the starting point for the path-averaged effective dissipation constructed in Section S5. On longer times ε varies along the ray, making $\Gamma = \Gamma(\varepsilon(t), \mathbf{k})$ slowly time-dependent. At each instant the local Green-Kubo construction applies, and the cumulative effect is obtained by integrating Eq. (S.50) (Section S5).

E. Projected dynamics and identification of the stochastic vortex force

We construct the projected dynamics and identify the microscopic force entering Eq. (S.31).

E.1. Generalised Langevin equation

In the Hilbert space $\mathcal{H} = L^2(\rho_{\text{ss}})$ with inner product (S.38), where elements are phase-space observables $A(\mathbf{X})$, the orthogonal projection onto the swell subspace is

$$\mathcal{P}A = \sum_{\mathbf{k} \in \mathcal{B}} \frac{\langle A, a_{\mathbf{k}} \rangle_{\rho}}{\langle a_{\mathbf{k}}, a_{\mathbf{k}} \rangle_{\rho}} a_{\mathbf{k}}, \quad \mathcal{Q} = 1 - \mathcal{P}. \quad (\text{S.51})$$

By factorisation (A5(ii)), $\langle a_{\mathbf{k}}, a_{\mathbf{k}} \rangle_{\rho} = \langle |a_{\mathbf{k}}|^2 \rangle = 2E_{\mathbf{k}}$. The microscopic amplitude equation can be written schematically as

$$\dot{a}_{\mathbf{k}}(t) = i \sum_{\mathbf{k}'} \Omega_{\mathbf{k}\mathbf{k}'} a_{\mathbf{k}'}(t) + \mathcal{F}_{\mathbf{k}}(t), \quad (\text{S.52})$$

where $\Omega_{\mathbf{k}\mathbf{k}'}$ is the linear frequency matrix (intrinsic dispersion plus Craik-Leibovich mean-flow corrections) and $\mathcal{F}_{\mathbf{k}}$ collects all remaining nonlinear coupling terms. The Mori-Zwanzig projection converts this into an exact generalised Langevin equation

$$\dot{a}_{\mathbf{k}}(t) = i \sum_{\mathbf{k}'} \Omega_{\mathbf{k}\mathbf{k}'} a_{\mathbf{k}'}(t) - \int_0^t K_{\mathbf{k}}(t-s) a_{\mathbf{k}}(s) ds + F_{\mathbf{k}}(t), \quad (\text{S.53})$$

where $F_{\mathbf{k}}(t) = e^{i\mathcal{Q}\mathcal{L}t} \mathcal{Q}\mathcal{F}_{\mathbf{k}}(0)$ is the fluctuating force propagated entirely in the orthogonal subspace. The memory kernel is diagonal in wavevector, $K_{\mathbf{k}\mathbf{k}'}(\tau) = K_{\mathbf{k}}(\tau) \delta_{\mathbf{k}\mathbf{k}'}$, as a consequence of the spatial homogeneity assumed in A3: the ρ_{ss} -weighted cross-correlations between distinct \mathbf{k} -modes vanish, so the Mori-Zwanzig memory matrix reduces to a scalar kernel for each mode. By construction and the factorisation A5(ii), the fluctuating force satisfies

$$\mathcal{P}F_{\mathbf{k}}(t) = 0, \quad \langle F_{\mathbf{k}}, a_{\mathbf{k}} \rangle_{\rho} = 0, \quad \langle F_{\mathbf{k}}(t) a_{\mathbf{k}}^*(s) \rangle = 0 \quad (s \leq t). \quad (\text{S.54})$$

E.2. Stochastic vortex force as the microscopic coupling

In Section S1 the physical wave-vorticity coupling was decomposed into three pieces: $\mathbf{u}_{\phi} \times \bar{\boldsymbol{\Omega}}$ (coupling to the ensemble-mean vorticity), $\mathbf{u}_{\phi} \times \boldsymbol{\omega}_{\text{wave}}$ (wave self-interaction via the wave-slaved vorticity), and $\mathbf{u}_{\phi} \times \boldsymbol{\omega}'$ (coupling to the turbulent vorticity fluctuation). The energy-budget analysis there showed that only the last term, the stochastic vortex force

$$\mathbf{f}_{\text{svf}} = \mathbf{u}_{\phi} \times \boldsymbol{\omega}', \quad (\text{S.55})$$

permits irreversible energy transfer from swell to turbulence. The mean-vorticity term is reactive and does not enter the dissipative Green-Kubo real part. The wave-slaved term carries spectral support only at zero and double frequency and therefore does not project onto the swell mode. The Mori-Zwanzig noise $F_{\mathbf{k}}(t)$, defined by the \mathcal{Q} -projector, satisfies three defining properties. Zero projection onto the wave subspace, zero correlation with the wave amplitudes, and propagation entirely within the orthogonal subspace (Eq. S.54). At the field level, the SVF \mathbf{f}_{svf} satisfies the same three properties under A1-A5. Zero ensemble mean (A3(iii)), zero correlation with $a_{\mathbf{k}}$ (A5(ii)), and autonomous temporal evolution governed by the turbulent cascade (A3(i)). Under the scale-separation and factorisation assumptions (A2-A5), the two selection procedures, Hilbert-space orthogonal projection and Navier-Stokes three-term decomposition, therefore isolate the same physical degrees of freedom. Fast, bath-dominated fluctuations orthogonal to the resolved wave amplitudes. The abstract noise can accordingly be written as the mode projection of the physical field,

$$F_{\mathbf{k}}(t) = \int d^3\mathbf{x} \psi_{\mathbf{k}}^*(\mathbf{x}) \cdot \mathbf{f}_{\text{svf}}(\mathbf{x}, t), \quad (\text{S.56})$$

where $\psi_{\mathbf{k}}(\mathbf{x})$ is the linear velocity eigenfunction of mode \mathbf{k} , with the normalisation convention $E_{\mathbf{k}} = \frac{1}{2}|a_{\mathbf{k}}|^2$ (Eq. S.32). Operationally, $\boldsymbol{\omega}'$ is obtained in a turbulence-resolving simulation by subtracting the wave-slaved vorticity $\boldsymbol{\omega}_{\text{wave}} = \nabla \times (\boldsymbol{\xi} \times \boldsymbol{\Omega}_{\text{s}})$ and the ensemble-mean $\bar{\boldsymbol{\Omega}}$ from the total vorticity. The SVF is then formed as $\mathbf{u}_{\phi} \times \boldsymbol{\omega}'$ and projected onto mode \mathbf{k} via (S.56). This identification is a *physical equivalence under A2-A5*, not an algebraic identity. The \mathcal{Q} -projector acts in observable space while \mathbf{f}_{svf} is defined at the field level, but the assumptions guarantee that both yield the same force autocorrelation $C_F(\tau; \mathbf{k})$ and hence the same $\Gamma(\mathbf{k})$.

F. Green-Kubo relation and non-negativity of Γ

With $F_{\mathbf{k}}$ identified as the mode-projected SVF, FDR-II (S.39) can be written as

$$K_{\mathbf{k}}(\tau) = \frac{\langle F_{\mathbf{k}}(0) F_{\mathbf{k}}(\tau)^* \rangle}{2E_{\mathbf{k}}}. \quad (\text{S.57})$$

The Green-Kubo damping coefficient is then

$$\Gamma(\mathbf{k}) \equiv \int_0^\infty \text{Re}[K_{\mathbf{k}}(\tau)] d\tau = \frac{1}{2E_{\mathbf{k}}} \int_0^\infty \text{Re}[\langle F_{\mathbf{k}}(0) F_{\mathbf{k}}(\tau)^* \rangle] d\tau. \quad (\text{S.58})$$

The integral is convergent (A6). Stationarity here refers to the bath process conditional on quasi-frozen $a_{\mathbf{k}}$ over $\tau \lesssim \tau_c$ (A5(i)), not to the globally evolving coupled system. Because $F_{\mathbf{k}}(t)$ is stationary with finite variance under this conditional measure, its autocorrelation is positive-definite in the sense of Bochner,

$$\sum_{j,\ell} \alpha_j \alpha_\ell^* C_F(t_j - t_\ell) \geq 0 \quad \text{for any finite set } \{t_j\}, \{\alpha_j\}, \quad (\text{S.59})$$

where $C_F(\tau) = \langle F_{\mathbf{k}}(0) F_{\mathbf{k}}(\tau)^* \rangle$. Bochner's theorem then implies that the power spectral density

$$S_F(\omega) = \int_{-\infty}^\infty C_F(\tau) e^{i\omega\tau} d\tau \quad (\text{S.60})$$

(we adopt the convention without 2π prefactors) is non-negative for all ω . By stationarity, $C_F(-\tau) = C_F(\tau)^*$, so $S_F(0)$ is real,

$$S_F(0)^* = \int_{-\infty}^\infty C_F(\tau)^* d\tau = \int_{-\infty}^\infty C_F(-\tau) d\tau = S_F(0). \quad (\text{S.61})$$

The same symmetry allows the half-line integral in Eq. (S.58) to be extended to negative times: $\text{Re}[C_F(-\tau)] = \text{Re}[C_F(\tau)]$, hence $\int_0^\infty \text{Re}[C_F(\tau)] d\tau = \frac{1}{2} S_F(0)$, giving

$$\Gamma(\mathbf{k}) = \frac{S_F(0)}{4E_{\mathbf{k}}} \geq 0. \quad (\text{S.62})$$

Because $C_F \in L^1(\mathbb{R})$ (A6, Section A), its Fourier transform $S_F(\omega)$ is a bounded continuous function, so $S_F(0)$ is finite. The autocorrelation of any second-order stationary process is positive-definite in the sense of (S.59). Since additionally $\langle F_{\mathbf{k}} \rangle = 0$ (A3(iii)), C_F is a centred autocorrelation. The non-negativity of $S_F(0)$, and hence of Γ , then follows from Bochner's theorem.

Theorem 1 (Non-negativity of Γ). *Under A1, A3(i, iii), A5(i) and A6,*

$$\boxed{\Gamma(\mathbf{k}) \geq 0 \quad \text{for all } \mathbf{k} \in \mathcal{B}.} \quad (\text{S.63})$$

The stochastic vortex force cannot, on average, amplify swell. Individual propagation paths can exhibit apparent growth due to fluctuations (Section H), but the Markovian coarse-grained decay rate is non-negative. In the Markovian limit (A2), $\langle E_{\mathbf{k}}(t) \rangle$ decays monotonically for $t \gg \tau_c$ (Section G, Eq. S.70).

The sign $\Gamma \geq 0$ is a purely kinematic property of stationary fluctuations. The Navier-Stokes content of the theory lies in identifying the correct microscopic force $F_{\mathbf{k}}$ and in evaluating its zero-frequency spectrum $S_F(0)$. The proof uses the following assumptions. A1 defines the wave amplitudes $a_{\mathbf{k}}$. A3(i) (stationarity and homogeneity of ω') and A5(i) (local stationarity of the bath reference measure at fixed $a_{\mathbf{k}}$) guarantee that $C_F(\tau)$ is time-translation invariant. A3(iii) (zero ensemble mean under the bath measure) ensures $\langle F_{\mathbf{k}} \rangle = 0$, so that $C_F(\tau)$ is a centred

autocorrelation. A6 ensures that $S_F(0)$ is finite. The non-negativity then follows from Bochner's theorem alone.

The following assumptions are *not* invoked in the sign proof. A2 (time-scale separation) enters only in the Markovian reduction (Section G). A3(ii) (phase decoupling) and A5(ii) (factorisation) enter only in the factorisation of ρ_{ss} and in the cancellation of $E_{\mathbf{k}}$ from the denominator (Section C.4). A4 (linear truncation) affects the amplitude dependence of Γ but not its sign. The non-negativity theorem is both spectrum-agnostic (the form of $E_\omega(q)$ does not enter the proof) and wave-type-agnostic (it applies equally to wind waves and young seas). What changes across wave types is the value of Γ and whether the SVF damping can be isolated from competing processes (Section S9). The degeneracy $\Gamma(\mathbf{k}) = 0$ would require a fine-tuned cancellation $S_F(0) = 0$ between positive and negative lobes of $C_F(\tau)$. For a propagating wave packet that samples independent eddies, such cancellation is non-generic. The finite parameter $\delta = u'/c_g > 0$ ensures that each eddy evolves during the encounter time, breaking microscopic time-reversal symmetry and producing a strictly positive zero-frequency spectral density (Section I).

G. Markovian limit and monotonic energy decay

Under A2 the memory kernel $K_{\mathbf{k}}(\tau)$ decays on $\tau_c \ll \Gamma^{-1}$. On times $t \gg \tau_c$ the amplitude varies negligibly over the support of K , so

$$\int_0^t K_{\mathbf{k}}(\tau) a_{\mathbf{k}}(t - \tau) d\tau \approx \Gamma(\mathbf{k}) a_{\mathbf{k}}(t) + i \Delta\omega_{\mathbf{k}} a_{\mathbf{k}}(t), \quad (\text{S.64})$$

where we have split the integral into real and imaginary parts,

$$\Gamma(\mathbf{k}) = \int_0^\infty \text{Re}[K_{\mathbf{k}}(\tau)] d\tau, \quad \Delta\omega_{\mathbf{k}} = \int_0^\infty \text{Im}[K_{\mathbf{k}}(\tau)] d\tau. \quad (\text{S.65})$$

The frequency shift $\Delta\omega_{\mathbf{k}}$ can be absorbed into the dispersion relation. For swell, $|\Delta\omega|/\omega \sim \delta^2 \sim 10^{-6}$ - 10^{-4} , undetectable in practice. Substituting (S.64) into the GLE (S.53) yields

$$\dot{a}_{\mathbf{k}} = i(\omega_{\mathbf{k}} + \Delta\omega_{\mathbf{k}}) a_{\mathbf{k}} - \Gamma(\mathbf{k}) a_{\mathbf{k}} + F_{\mathbf{k}}(t), \quad (\text{S.66})$$

where for clarity we have suppressed the coupling to nearby \mathbf{k}' in the intrinsic dispersion. Multiplying (S.66) by $a_{\mathbf{k}}^*$, adding the complex conjugate, and ensemble-averaging gives

$$\begin{aligned} \frac{d}{dt} \langle |a_{\mathbf{k}}|^2 \rangle &= 2 \text{Re} \langle a_{\mathbf{k}}^* \dot{a}_{\mathbf{k}} \rangle \\ &= 2 \text{Re} \left[i(\omega_{\mathbf{k}} + \Delta\omega_{\mathbf{k}}) \langle |a_{\mathbf{k}}|^2 \rangle - \Gamma(\mathbf{k}) \langle |a_{\mathbf{k}}|^2 \rangle + \langle a_{\mathbf{k}}^* F_{\mathbf{k}} \rangle \right]. \end{aligned} \quad (\text{S.67})$$

The first term is purely imaginary, so its real part vanishes. The third term vanishes by the orthogonality $\langle a_{\mathbf{k}}^* F_{\mathbf{k}} \rangle = 0$ (Eq. S.54). Using $\langle |a_{\mathbf{k}}|^2 \rangle = 2E_{\mathbf{k}}$ we obtain

$$\frac{d}{dt} \langle E_{\mathbf{k}}(t) \rangle = -2\Gamma(\mathbf{k}) \langle E_{\mathbf{k}}(t) \rangle, \quad (\text{S.68})$$

with solution

$$\langle E_{\mathbf{k}}(t) \rangle = E_{\mathbf{k}}(0) e^{-2\Gamma(\mathbf{k})t}. \quad (\text{S.69})$$

Since $\Gamma \geq 0$,

$$\frac{d}{dt} \langle E_{\mathbf{k}}(t) \rangle \leq 0 \quad \text{for all } t \gg \tau_c. \quad (\text{S.70})$$

The Markov approximation is controlled by the ratio τ_c/Γ^{-1} . With $\tau_c \sim \ell/c_g \sim 5$ s (Section A), the small parameter

$$\delta = \frac{u'}{c_g} \sim \frac{\tau_c}{\tau_q} \Big|_{q \sim k} \sim 10^{-3} \text{--} 10^{-2} \quad (\text{S.71})$$

simultaneously gives the turbulence-to-wave velocity ratio and, by the Kolmogorov relation $\varepsilon \sim u'^3/\ell$, the ratio of the advective decorrelation time to the eddy turnover time $\tau_q \sim (\varepsilon q^2)^{-1/3}|_{q \sim k}$. The finite but small value of δ has a dual role. It ensures that the Markov approximation is accurate, with $\tau_c/\Gamma^{-1} \lesssim 10^{-3}$ even in extreme conditions (the explicit dependence $\Gamma(\delta, \varepsilon, k)$ is derived in Sections S3-S5), and it provides the causal phase lag responsible for strict positivity $\Gamma > 0$ (Section I). Beyond the Markov limit, the GLE and FDR-II remain exact and define a frequency-dependent damping $\hat{\Gamma}(\omega) = \text{Re} \int_0^\infty K_{\mathbf{k}}(\tau) e^{i\omega\tau} d\tau$. For trans-oceanic swell the extreme smallness of δ makes any departure from pure exponential decay negligible.

The non-negativity theorem holds for surface gravity waves propagating through turbulence. The closed-form scaling law requires additionally the weak-coupling and phase-decoupling conditions that characterise remote swell. A detailed analysis of the three dissipation channels and the domain of validity is given in Section S9.

H. Dual-line prediction structure

The Mori-Zwanzig projection fixes both the mean damping and the residual noise. For the band-integrated swell energy $E_w = \sum_{\mathbf{k} \in \mathcal{B}} E_{\mathbf{k}}$, the Markovian coarse-grained dynamics can be written as

$$\frac{dE_w}{dt} = -2\Gamma E_w + \tilde{\eta}(t), \quad (\text{S.72})$$

where $\tilde{\eta}(t)$ is a zero-mean stochastic forcing inherited from $F_{\mathbf{k}}$. FDR-II constrains its autocorrelation: the noise diffusivity $D_E = 4\Gamma E_w^2$ is locked to the same Green-Kubo kernel that fixes the mean decay, so no additional parameter enters. Ensemble averaging removes $\tilde{\eta}$ and recovers Eq. (S.68). Converting to a spatial decay rate gives $\mu_E(\omega) = 2\Gamma/c_g$. Along a single satellite track, however, the integrated noise produces order-one relative fluctuations in the apparent rate $\hat{\mu}$. Because $\hat{\mu}$ is a log-energy regression slope while the dynamics are multiplicative, the pathwise estimator acquires an Itô correction, $\langle \hat{\mu} \rangle = 2\mu_E$. In the idealised near-independent-encounter limit (Section S6),

$$\text{Var}(\hat{\mu}) = \frac{2\mu_E}{L}, \quad c_0 \equiv \frac{\text{Var}(\hat{\mu})}{\langle \hat{\mu} \rangle / L} = 1, \quad (\text{S.73})$$

with L the path length, and the fraction of tracks with apparent negative attenuation is $P(\hat{\mu} < 0) = \Phi(-\sqrt{2\mu_E L})$, where Φ is the standard normal CDF. For trans-oceanic swell $\mathcal{S} = \mathcal{O}(1)$, predicting a substantial minority of negative pathwise estimates-consistent with 13.3% (19) and $\sim 24\%$ (34). The full derivation, including the passage from the mode-sum to a scalar noise and the explicit evaluation of the constants 2, 2 and 1, is given in Section S6.

I. Physical origin of irreversibility: the single wave-eddy encounter

Bochner's theorem guarantees $\Gamma \geq 0$ whenever the force process is stationary (Section F). That $\Gamma > 0$ strictly requires a physical argument. The bath element must possess internal degrees of freedom that prevent the wave-eddy interaction from being elastic.

I.1. Encounter kinematics and modal energy exchange

The modal energy change during a single wave-eddy encounter of duration $\tau_{\text{adv}} \sim \ell/c_g \sim 1/(q c_g)$ is

$$\Delta E_{\mathbf{k}} = \text{Re} \int_0^{\tau_{\text{adv}}} a_{\mathbf{k}}^*(t) F_{\mathbf{k}}(t) dt, \quad (\text{S.74})$$

which can be positive or negative for any given encounter, depending on the instantaneous configuration of ω' .

I.2. Frozen-eddy limit and the physical origin of irreversibility

In the quasi-frozen limit where ω' does not evolve during the encounter ($\tau_{\text{adv}} \ll \tau_{\text{eddy}}$ with $\delta \rightarrow 0$), a frozen but spatially inhomogeneous vorticity field can still exert a nonzero instantaneous force on the propagating wave packet. Along a given realisation, $F_{\mathbf{k}}(t)$ need not vanish, and the packet may undergo conservative redistribution of wave action among neighbouring wavevectors. That process is a within-wave-sector rearrangement, not the irreversible dissipation rate $\Gamma(\mathbf{k})$ defined by the Green-Kubo projection. The quantity $\Gamma(\mathbf{k})$ in Eq. (S.58) measures irreversible energy transfer from the wave field to the rotational bath, as enforced by the energy budget (Eq. S.9). In the strictly frozen-bath limit, the bath has no internal evolution during the encounter and therefore cannot absorb and retain net energy from the wave. Conservative mode-to-mode redistribution within the wave sector does not contribute to the positive-definite friction coefficient. Irreversibility requires the eddy to evolve during the encounter, providing the microscopic mechanism by which energy absorbed from the wave is redistributed among internal bath degrees of freedom before the wave phase returns. The characteristic evolution time of an inertial-range eddy is the Kolmogorov turnover time

$$\tau_{\text{eddy}}(q) \sim (\varepsilon_{\text{eff}} q^2)^{-1/3}, \quad (\text{S.75})$$

which measures how long it takes for the eddy to lose memory of its initial configuration through the turbulent cascade. For far-field conditions with $\varepsilon_{\text{eff}} \sim 5 \times 10^{-7} \text{ m}^2 \text{ s}^{-3}$ (Section S5 E, wall-law profile under $U_{10} \approx 10 \text{ m s}^{-1}$) and $q \sim k \approx 0.02 \text{ rad m}^{-1}$, $\tau_{\text{eddy}} \sim 1.7 \times 10^3 \text{ s}$ ($\approx 30 \text{ min}$). The ratio of the two time scales defines the key small parameter, recalling the key small parameter (Eq. S.71), $\delta \equiv \tau_{\text{adv}}/\tau_{\text{eddy}} \sim u'/c_g \sim 10^{-3}$ - 10^{-2} .

Here $u'(q) \sim (\varepsilon_{\text{eff}}/q)^{1/3}$ is the Kolmogorov velocity at the swell-selected eddy scale. Since ε_{eff} varies along the swell ray with local forcing conditions (Section S5 E), the small parameter spans from $\delta \sim 2 \times 10^{-3}$ in light-wind regions ($\varepsilon_{\text{eff}} \sim 5 \times 10^{-7}$) to $\delta \sim 10^{-2}$ in moderate-wind regions ($\varepsilon_{\text{eff}} \sim 10^{-5}$).

I.3. Encounter-level energy statistics and the bias-to-fluctuation ratio

The modal energy change $\Delta E_{\mathbf{k}}$ fluctuates from encounter to encounter. To estimate its magnitude we scale the mode-projected force $F_{\mathbf{k}} \sim U_0 |\omega'| \sim U_0 u'/\ell$ (orbital speed times vorticity at scale ℓ) and multiply by the amplitude times the advective decorrelation time $\tau_{\text{adv}} \sim \ell/c_g$. The resulting fluctuation amplitude of the energy change per encounter is

$$\sigma_{\Delta E} \sim U_0 \frac{u'^2}{\ell} \frac{\ell}{c_g} = \frac{U_0 u'^2}{c_g}, \quad (\text{S.76})$$

where $U_0 = a\omega$ is the surface orbital speed. In the quasi-frozen limit $\langle \Delta E_{\mathbf{k}} \rangle = 0$ and the encounter is elastic. During the advective decorrelation time τ_{adv} , however, the eddy's vorticity evolves by a fraction $\Delta\omega'/\omega' \sim \tau_{\text{adv}}/\tau_{\text{eddy}} = \delta$: the configuration sampled at the end of the interval differs from that at the beginning by $\mathcal{O}(\delta)$. This breaks the temporal symmetry of the force history, so the energy returned during the second half of the encounter falls short of that absorbed during the first half by a fraction δ , and the systematic (mean) energy change per encounter is

$$|\langle \Delta E_{\mathbf{k}} \rangle| \sim \delta \sigma_{\Delta E} \sim \frac{U_0 u'^3}{c_g^2}. \quad (\text{S.77})$$

Equivalently, in terms of fractional modal energy, the mean loss per encounter is $|\bar{\epsilon}| \sim E_{\mathbf{k}} \delta^2$ and the standard deviation is $\sigma \sim E_{\mathbf{k}} \delta$. The bias-to-fluctuation ratio per encounter is therefore

$$\boxed{\frac{|\langle \Delta E_{\mathbf{k}} \rangle|}{\sigma_{\Delta E}} \sim \delta = \frac{u'}{c_g} \sim 10^{-3}\text{-}10^{-2}}, \quad (\text{S.78})$$

confirming that each wave-eddy encounter is nearly symmetric. The systematic energy loss is suppressed relative to the fluctuations by the ratio of advective decorrelation time to eddy turnover time. That the sign of the bias is negative-energy flows from the wave to the turbulence follows from causality and is guaranteed by the non-negativity of the force power spectral density $S_F(\omega) \geq 0$ (Section F). The two distinct roles of the time-scale hierarchy are worth emphasising: *advective decorrelation* ($c_g \gg u'$) controls the *magnitude* of dissipation by setting τ_{eff} , while the bath's *internal dynamics* (τ_{eddy} finite) guarantee its *sign* by providing the causal phase lag. Neither alone suffices. Advection without internal evolution gives an elastic encounter ($\langle \Delta E_k \rangle = 0$). Internal evolution without advection gives an autocorrelation that does not decay along the ray, so the Green-Kubo integral does not converge.

S3. Evaluating the force autocorrelation in wavenumber space

Since we consider isotropic turbulence interacting with a unidirectional swell, we write $k = |\mathbf{k}|$ and suppress bold face on the swell wavevector throughout Sections S3 and S4. The turbulent wavevector \mathbf{q} remains three-dimensional until angular integration is performed. Every turbulent eddy that overlaps with the wave orbital layer exerts a random force on the swell mode. The damping rate $\Gamma(k)$ is therefore a weighted integral over all turbulent scales, with the vorticity spectrum, the coupling geometry, and the decorrelation time along the ray setting the weight at each q .

Three facts convert the Green-Kubo time integral (S.58) into a time-free scaling law. First, advective sweeping at $c_g \gg u'$ dominates eddy turnover, so the effective correlation time is purely kinematic, $\tau_{\text{eff}}(q; k) = C_\tau / (q c_g)$. Second, the Kolmogorov spectrum fixes the force variance at each shell through the vorticity spectrum $E_\omega(q) = q^2 E_u(q) \propto \varepsilon^{2/3} q^{1/3}$, windowed by the scale-selection function $\mathcal{S}(q/k)$. Third, deep-water kinematics absorb the remaining scales. Amplitude dependence cancels by linearity of the SVF, and the dispersion relation $\omega^2 = gk$ converts $\Gamma(k) \propto \varepsilon^{2/3} k^{1/3} / c_g$ into $\mu_E(\omega) = C_{\text{tot}} \varepsilon^{2/3} g^{-7/3} \omega^{8/3}$, with no microscopic time scale remaining.

A. The Green-Kubo starting point

The Green-Kubo relation derived in Section S2 gives the amplitude damping rate for a swell mode with wavenumber k as

$$\Gamma(k) = \frac{1}{2E_k} \int_0^\infty \Re[\langle F_k(0) F_k^*(t) \rangle] dt, \quad (\text{S.79})$$

where $E_k = \frac{1}{2}|a_k|^2$ (convention of A1) and $F_k(t)$ is the projection of the stochastic vortex force onto the swell mode,

$$F_k(t) = \int d^3\mathbf{x} \psi_k^*(\mathbf{x}) \cdot \mathbf{f}_{\text{svf}}(\mathbf{x}, t). \quad (\text{S.80})$$

Here $\psi_k(\mathbf{x})$ is the normalised eigenfunction of the linear wave mode, with vertical structure $\propto e^{kz}$ for deep-water waves. Throughout this section, $a_k(t)$ denotes the slowly varying complex envelope of a narrowband wave packet centred at wavenumber k , not a global Fourier coefficient of the entire ocean surface. The mode function ψ_k is correspondingly understood as a wave-packet eigenfunction whose horizontal Fourier transform $\tilde{\psi}_k(\mathbf{p})$ is sharply peaked at $\mathbf{p} = \mathbf{k}$ with spectral width $\Delta k \sim 1/L_{\text{env}} \ll k$ (where L_{env} is the packet length). The projection (S.80) therefore acts as a local spatial filter. It extracts the force component within the spectral bandwidth of the wave packet, not a single plane-wave Fourier coefficient that would enforce a strict $\delta(\mathbf{q}_h)$ selection in the wavenumber convolution. This local-envelope interpretation is consistent with the Mori-Zwanzig framework of Section S2 and with the standard WKB/Wigner representation used in wave-action transport theory [6, 35]. The turbulent field is modelled as a homogeneous,

stationary random process characterised by its two-point spectrum $S_u(q, \Omega)$. Since $\Gamma(k)$ depends only on the two-point forcing correlation, higher-order cumulants do not enter at leading order.

Because $F_k \propto a_k$ (Section S2 C), the wave-energy factors in the numerator and denominator of (S.79) cancel exactly, making $\Gamma(k)$ independent of the modal normalisation (Eq. S.46). The explicit Fourier-space calculations below are carried out in terms of F_k , retaining the $1/(2E_k)$ prefactor. The cancellation of the modal amplitude is tracked via the dimensionless overlap factor $C_E(k)$ defined in Section F.

B. Force autocorrelation in wavenumber-frequency space

The fluctuating turbulent velocity admits the Fourier representation [36, 37]

$$\mathbf{u}'(\mathbf{x}, t) = \int \frac{d^3q}{(2\pi)^3} \int \frac{d\Omega}{2\pi} \hat{\mathbf{u}}'(\mathbf{q}, \Omega) e^{i(\mathbf{q}\cdot\mathbf{x} - \Omega t)}. \quad (\text{S.81})$$

For a statistically homogeneous and stationary field, the two-point correlation is

$$\langle \hat{u}'_i(\mathbf{q}, \Omega) \hat{u}'_j^*(\mathbf{q}', \Omega') \rangle = (2\pi)^4 \delta(\mathbf{q} - \mathbf{q}') \delta(\Omega - \Omega') P_{ij}(\hat{\mathbf{q}}) S_u(q, \Omega), \quad (\text{S.82})$$

where $P_{ij}(\hat{\mathbf{q}}) = \delta_{ij} - \hat{q}_i \hat{q}_j$ enforces incompressibility and $S_u(q, \Omega)$ is the four-dimensional velocity spectrum (energy density per unit $d^3q d\Omega$). Integrating over frequency gives the three-dimensional spectrum $S_u(q) = \int S_u(q, \Omega) d\Omega$ (energy density per unit d^3q , normalised so that $\int S_u(q) d^3q = \frac{1}{2} \langle |\mathbf{u}'|^2 \rangle$). The corresponding isotropic one-dimensional spectrum is $E_u(q) = 4\pi q^2 S_u(q)$. In the inertial range, $S_u(q, \Omega) = S_u(q) \chi(\Omega; q)$, where χ has width $\omega_q \sim (\varepsilon q^2)^{1/3}$ and unit area. The SVF $\mathbf{f}_{\text{svf}} = \mathbf{u}_\phi \times \boldsymbol{\omega}'$ couples the swell to every turbulent mode simultaneously. Under Fourier transform, the vorticity becomes $\hat{\boldsymbol{\omega}}' = i\mathbf{q} \times \hat{\mathbf{u}}'$. To expose the convolution structure we adopt a simplified linearly polarised orbital velocity,

$$\mathbf{u}_\phi(\mathbf{x}, t) = U_0 \hat{\mathbf{k}} e^{i(\mathbf{k}\cdot\mathbf{x} - \omega t)} + \text{c.c.}, \quad (\text{S.83})$$

where $U_0 = a\omega$. This monochromatic form is a controlled schematic representation of the overlap structure. It isolates the wavenumber-convolution geometry that determines which turbulent scales couple to the swell. The complete phase-averaged treatment with circularly polarised deep-water orbits (Section S5 A) yields the same geometric factor $\tilde{G}_{\text{geom}} = 2/3$ for isotropic turbulence. Multiplying by the Fourier expansion of $\boldsymbol{\omega}'$ and retaining the co-rotating contribution gives

$$\hat{\mathbf{f}}_{\text{svf}}(\mathbf{q}, \Omega) = iU_0 \hat{\mathbf{k}} \times (\mathbf{q} \times \hat{\mathbf{u}}'(\mathbf{q}, \Omega)), \quad (\text{S.84})$$

where the vortex-force mode resides at $(\mathbf{k} + \mathbf{q}, \omega + \Omega)$. Expanding via $\mathbf{a} \times (\mathbf{b} \times \mathbf{c}) = \mathbf{b}(\mathbf{a} \cdot \mathbf{c}) - \mathbf{c}(\mathbf{a} \cdot \mathbf{b})$,

$$\hat{\mathbf{f}}_{\text{svf}}(\mathbf{q}, \Omega) = iU_0 [\mathbf{q}(\hat{\mathbf{k}} \cdot \hat{\mathbf{u}}') - \hat{\mathbf{u}}'(\hat{\mathbf{k}} \cdot \mathbf{q})]. \quad (\text{S.85})$$

The projected force (S.80) in Fourier space is

$$F_k(t) = \int \frac{d^3q}{(2\pi)^3} \int \frac{d\Omega}{2\pi} \tilde{\psi}_k^*(\mathbf{k} + \mathbf{q}) \cdot \hat{\mathbf{f}}_{\text{svf}}(\mathbf{q}, \Omega) e^{-i(\omega + \Omega)t}, \quad (\text{S.86})$$

where $\tilde{\psi}_k(\mathbf{p})$ is sharply peaked at $\mathbf{p} = \mathbf{k}$ in the horizontal, but has broad vertical support set by the depth eigenfunction e^{kz} . Because $a_k(t)$ is a narrow-band envelope (not a strict plane-wave coefficient), the projection acts as a local spectral filter with finite horizontal bandwidth $\Delta k \sim L_{\text{env}}^{-1} \ll k$. The along-ray phase factor $e^{-i(\Omega - \mathbf{q} \cdot \mathbf{c}_g)t}$ therefore weights the full range of locally overlapping eddy wavenumbers, not just $\mathbf{q}_h = \mathbf{0}$. As the wave packet advances at c_g , it sequentially samples turbulent structures at every horizontal wavenumber q_h . The residence time within each structure is $\sim 1/(q_h c_g)$, and the temporal memory window \mathcal{W}_Ω (Eq. S.90 below) performs the resulting frequency selection. The overlap integral that emerges after the time

integration therefore runs over the full three-dimensional \mathbf{q} space, weighted by the depth overlap e^{2kz} , the temporal memory kernel, and the geometric vertex-not by the horizontal envelope bandwidth. A turbulent mode evaluated along the wave-packet trajectory $\mathbf{x}(t) = \mathbf{x}_0 + \mathbf{c}_g t$ acquires the advected phase

$$e^{i(\mathbf{q}\cdot\mathbf{x}-\Omega t)}\Big|_{\mathbf{x}=\mathbf{x}_0+\mathbf{c}_g t} = e^{i\mathbf{q}\cdot\mathbf{x}_0} e^{-i(\Omega-\mathbf{q}\cdot\mathbf{c}_g)t}, \quad (\text{S.87})$$

so the effective frequency seen by the packet is $\Omega_{\text{eff}} = \Omega - \mathbf{q} \cdot \mathbf{c}_g$. The force autocorrelation $\langle F_k(0) F_k^*(t) \rangle$ involves two integrals over (\mathbf{q}, Ω) . The turbulent correlation (S.82) collapses one via the delta functions, and the tensor contraction defines a scalar vertex $|V(\mathbf{q}; k)|^2$,

$$\langle F_k(0) F_k^*(t) \rangle = \int d^3q \int d\Omega |V(\mathbf{q}; k)|^2 S_u(q, \Omega) e^{-i(\Omega-\mathbf{q}\cdot\mathbf{c}_g)t}. \quad (\text{S.88})$$

Inserting into the Green-Kubo relation (S.79) and performing the time integral-which converges because the force autocorrelation has finite memory (A6)-yields

$$\boxed{\Gamma(k) = \frac{1}{2E_k} \int d^3q \int d\Omega S_u(q, \Omega) |V(\mathbf{q}; k)|^2 \mathcal{W}_\Omega(\Omega - \mathbf{q} \cdot \mathbf{c}_g)}, \quad (\text{S.89})$$

where the *temporal memory window*

$$\mathcal{W}_\Omega(\Delta\Omega) \equiv \text{Re} \int_0^\infty e^{-t/\tau_{\text{eff}}} e^{-i\Delta\Omega t} dt = \frac{\tau_{\text{eff}}^{-1}}{\tau_{\text{eff}}^{-2} + \Delta\Omega^2} \quad (\text{S.90})$$

is a Lorentzian peaked at $\Delta\Omega = 0$ with width $\sim \tau_{\text{eff}}^{-1}$. In the idealised infinite-memory limit $\tau_{\text{eff}} \rightarrow \infty$, the window reduces to the distributional form $\pi\delta(\Delta\Omega)$. The finite correlation time of the force process broadens this selection, concentrating contributions near the advective Doppler frequency without excluding any turbulent scale. Equation (S.89) sums contributions from every turbulent mode, weighted by the available energy $S_u(q, \Omega)$, the coupling geometry $|V(\mathbf{q}; k)|^2$, and the decorrelation weight \mathcal{W}_Ω . Equation (S.89) therefore weights all locally overlapping turbulent modes through the same Doppler-shifted temporal memory kernel, rather than through a strict resonant matching rule. In the sections that follow, angular integrations over \mathbf{q} are absorbed into a geometric factor \tilde{G}_{geom} and a scale-selection window $\mathcal{S}(q/k)$. The remaining spectral integrals use the one-dimensional spectrum $E_u(q) = 4\pi q^2 S_u(q)$.

C. Vortex-force vertex and angular integration

The vertex $|V(\mathbf{q}; k)|^2$ governs the coupling strength between a turbulent Fourier mode and the swell. Choose coordinates with $\hat{\mathbf{k}} = \mathbf{e}_x$ and let \mathbf{q} make angle θ with the swell direction. Incompressibility requires $\mathbf{q} \cdot \hat{\mathbf{u}}' = 0$, so $\hat{\mathbf{u}}'$ lies in the plane perpendicular to $\hat{\mathbf{q}}$. Constructing an orthonormal basis $\{\hat{\mathbf{q}}, \mathbf{e}_1, \mathbf{e}_2\}$ with \mathbf{e}_1 in the plane of $\hat{\mathbf{k}}$ and $\hat{\mathbf{q}}$,

$$\mathbf{e}_x = \cos\theta \hat{\mathbf{q}} + \sin\theta \mathbf{e}_1, \quad (\text{S.91})$$

and $\hat{\mathbf{u}}' = u'_1 \mathbf{e}_1 + u'_2 \mathbf{e}_2$. Applying the BAC-CAB identity to $\hat{\mathbf{f}}_{\text{svf}} = \mathbf{u}_\phi \times (i\mathbf{q} \times \hat{\mathbf{u}}')$ and evaluating the inner products gives

$$|\hat{\mathbf{f}}_{\text{svf}}|^2 = U_0^2 q^2 [u_1'^2 + u_2'^2 \cos^2 \theta]. \quad (\text{S.92})$$

For isotropic turbulence, $\langle u_1'^2 \rangle = \langle u_2'^2 \rangle = \frac{1}{2} u'^2(q)$, so the vertex is

$$|V(\mathbf{q}; k)|^2 \propto U_0^2 q^2 g(\cos\theta), \quad g(\cos\theta) = \frac{1}{2}(1 + \cos^2 \theta). \quad (\text{S.93})$$

Integrating over solid angle, $\int d\Omega_q g = \frac{1}{2}(4\pi + \frac{4\pi}{3}) = \frac{8\pi}{3}$, gives the direction-averaged vertex

$$\int d\Omega_q |V(\mathbf{q}; k)|^2 = U_0^2 q^2 G_{\text{geom}}, \quad G_{\text{geom}} = \frac{8\pi}{3}. \quad (\text{S.94})$$

We define the normalised geometric factor

$$\tilde{G}_{\text{geom}} \equiv \frac{G_{\text{geom}}}{4\pi} = \frac{2}{3}, \quad (\text{S.95})$$

which enters C_{tot} as an order-unity prefactor. The derivation above uses a linearly polarised orbital velocity as a pedagogical device. The full phase-averaged calculation with circularly polarised deep-water orbits (Section S5 A) yields the same value $\tilde{G}_{\text{geom}} = 2/3$ for isotropic turbulence.

D. Scale-selection window

The kinematic vertex derived above shows that every turbulent Fourier mode couples to the swell with strength proportional to q^2 , reflecting the curl in the vorticity definition. The net contribution of each mode to the damping rate, however, also depends on the spatial overlap between the eddy and the wave orbital layer. This depth-overlap geometry is captured by a dimensionless scale-selection window $\mathcal{S}(q/k)$, defined as the ratio of the depth-integrated mode-projected force variance to the bare kinematic vertex,

$$\mathcal{S}\left(\frac{q}{k}\right) \equiv \frac{\text{depth-integrated } |F_k(\mathbf{q})|^2}{U_0^2 q^2 \tilde{G}_{\text{geom}}}. \quad (\text{S.96})$$

By construction \mathcal{S} depends only on $x \equiv q/k$ and satisfies $\mathcal{S}(x) \propto x^2$ for $x \ll 1$, $\mathcal{S}(x) = \mathcal{O}(1)$ near $x \sim 1$, and $\mathcal{S}(x) \lesssim C x^{-1}$ for $x \gg 1$. These asymptotic behaviours ensure convergence of the Green-Kubo integral at both ends. The effective vertex including depth overlap is

$$|V(\mathbf{q}; k)|_{\text{eff}}^2 = U_0^2 q^2 \tilde{G}_{\text{geom}} \mathcal{S}\left(\frac{q}{k}\right). \quad (\text{S.97})$$

Ultraviolet suppression from vertical penetration mismatch. The wave orbital energy decays as $|\mathbf{u}_\phi(z)|^2 \propto e^{2kz}$ with penetration depth $\sim (2k)^{-1}$. The depth-projection integral is

$$I(k, q_z) = \int_{-\infty}^0 dz e^{2kz} e^{iq_z z} = \frac{1}{2k - iq_z}, \quad |I|^2 = \frac{1}{4k^2 + q_z^2}. \quad (\text{S.98})$$

This suppresses eddies with $q_z \gg k$. Averaging $|I|^2$ over the turbulent-wavenumber sphere, only a polar cap of angular width $\Delta\theta \sim k/q$ contributes efficiently for $q \gg k$, yielding a floor $\mathcal{S}(x) \lesssim C x^{-1}$. In the oceanic mixed layer, turbulent enstrophy is further concentrated toward the surface by wave-breaking injection and Langmuir circulation [38, 39], steepening the suppression beyond this floor.

To establish unconditional convergence of the Green-Kubo integral, suppose $|\mathbf{u}_\phi|^2 \propto e^{2kz}$, the turbulence follows the Kolmogorov spectrum $E_u \propto q^{-5/3}$, and the effective decorrelation time satisfies $\tau_{\text{eff}} \leq C_\tau (\varepsilon q^2)^{-1/3}$. The three-dimensional integrand then has three factors. Spectrum $S_u \propto q^{-11/3}$, bare vertex $\propto q^2$, and depth projection $|I|^2 = (4k^2 + q_z^2)^{-1}$. The polar-angle integral $\int_{-1}^1 d\zeta / (4k^2 + q^2 \zeta^2) \leq \pi / (2kq)$ bounds the radial integrand by $\lesssim q^{-4/3}$, which is integrable on $[Q, \infty)$. Comparing with the one-dimensional form identifies $\mathcal{S}(x) \sim x^{-1}$ as the floor from depth projection alone. The parametric family $\widehat{W}_\alpha(x) = x^2 / (1 + x^2)^\alpha$ with $\alpha \in [2, 5/2]$ used in Section S5 B for sensitivity analysis incorporates environmental effects beyond the floor. The baseline $\alpha = 2$ gives $C_S = \pi/6 \approx 0.52$, and C_S varies by a factor of 2.7 across the range, translating into only a factor of 1.4 in the predicted attenuation rate.

Infrared suppression from Galilean invariance. The behaviour $\mathcal{S}(x) \propto x^2$ as $x \rightarrow 0$ is not a modelling choice but a structural consequence of two conservation laws.

At $\mathbf{q} = \mathbf{0}$ the turbulent velocity is spatially uniform and its vorticity vanishes, so $F_k = 0$. Galilean invariance ensures that a uniform current produces only a Doppler shift without changing the wave energy. This zeroth-order vanishing is already encoded in the bare vertex factor q^2 .

At $\mathcal{O}(q/k)$ the vorticity is nonzero and the vortex force is finite. Denoting by $F_k^{(1)}$ the $\mathcal{O}(q/k)$ component of the mode-projected force, a linearly varying current refracts the wave while conserving wave action at leading order [40]. The $\mathcal{O}(q/k)$ force therefore drives only a reactive frequency shift along the ray—it enters the imaginary part of the self-energy, contributing to $\Delta\omega_k$, but not the dissipative real part Γ ,

$$\text{Re} \int_0^\infty \langle F_k^{(1)}(0) F_k^{(1)*}(t) \rangle dt = 0. \quad (\text{S.99})$$

At $\mathcal{O}(q^2/k^2)$ the curvature of the current field induces genuine scattering that does not reverse upon transit, so

$$\boxed{\mathcal{S}(x) = \mathcal{O}(x^2) \quad \text{as} \quad x = q/k \rightarrow 0, \quad \text{i.e.} \quad \mathcal{S}(0) = \mathcal{S}'(0) = 0.} \quad (\text{S.100})$$

The total effective coupling for $q \ll k$ therefore scales as $|V_{\text{eff}}|^2 \propto q^4/k^2$, with the bare vertex q^2 and the window suppression $(q/k)^2$ contributing equally to infrared convergence. Large eddies, despite their abundant Kolmogorov energy, contribute negligibly to swell dissipation.

To the authors' knowledge, the scale-selection window has not been derived explicitly in prior wave-turbulence interaction theories. Rapid distortion theory [41] treats $\ell \ll \lambda_w$, implicitly confirming ultraviolet convergence but not identifying $\mathcal{S}(x)$. The quasi-linear theory of McWilliams [6] evaluates the vortex force for a deterministic current at a single wavenumber, so spectral integration does not arise. WKB ray tracing [35] assumes $q \ll k$, where ultraviolet convergence is moot. The present analysis fills this gap.

E. Frequency integration and the effective correlation time

For homogeneous, stationary turbulence the four-dimensional spectrum factors as [42]

$$S_u(q, \Omega) = S_u(q) \chi(\Omega; q), \quad \int_{-\infty}^\infty \chi(\Omega; q) d\Omega = 1. \quad (\text{S.101})$$

Inserting into Eq. (S.89) and performing the frequency integral yields

$$\Gamma(k) = \frac{1}{2E_k} \int d^3q S_u(q) |V(\mathbf{q}; k)|^2 \tau_{\text{eff}}(q; k), \quad (\text{S.102})$$

with

$$\tau_{\text{eff}}(q; k) = \int_{-\infty}^\infty \chi(\Omega; q) \mathcal{W}_\Omega(\Omega - \mathbf{q} \cdot \mathbf{c}_g) d\Omega. \quad (\text{S.103})$$

Equation (S.103) is the exact definition of the effective memory time. The Lorentzian parametrisation used for \mathcal{W}_Ω in Eq. (S.90) is a convenient approximation whose width is set *a posteriori* by the dominant decorrelation mechanism, not assumed in advance. Two timescales compete inside this integral. The intrinsic eddy turnover time $\tau_{\text{eddy}}(q) \sim (\varepsilon q^2)^{-1/3}$ measures how fast the eddy forgets its initial configuration through the cascade. The advective decorrelation time

$$\tau_{\text{adv}}(q) \sim \frac{1}{q c_g} \quad (\text{S.104})$$

is the time for the advected phase $\exp(i\mathbf{q} \cdot \mathbf{c}_g t)$ in the force autocorrelation to accumulate an $\mathcal{O}(1)$ shift as the wave-energy trajectory traverses one correlation length q^{-1} . This is the

wave-propagation analogue of the Kraichnan-Tennekes random sweeping hypothesis [43, 44]. For oceanic swell, $c_g \sim 10\text{-}30 \text{ m s}^{-1}$ exceeds $u' \sim 0.01\text{-}0.1 \text{ m s}^{-1}$ by two to three orders of magnitude, so $\tau_{\text{adv}} \ll \tau_{\text{eddy}}$ at every scale and advective sweeping governs the decorrelation throughout. The effective correlation time therefore reduces to

$$\tau_{\text{eff}}(q; k) \simeq \frac{C_\tau}{q c_g(k)}, \quad (\text{S.105})$$

where $C_\tau = \int_0^\infty \mathcal{R}(s) ds$ is a dimensionless shape factor of order unity determined by the spatial correlation function of inertial-range eddies (Section C). The crossover wavenumber at which τ_{eddy} and τ_{adv} become comparable is $q_* \sim \varepsilon/c_g^3 \sim 10^{-9} \text{ m}^{-1}$, seven orders of magnitude below the swell wavenumber $k \sim 10^{-2} \text{ m}^{-1}$. The advective limit therefore holds at all scales that contribute to the Green-Kubo integral.

At the dominant coupling scale $q \sim k$, the eddy diameter $\ell \sim \lambda$ is much smaller than the wave-packet envelope $L_{\text{env}} \sim \mathcal{O}(10\lambda)$, so the geometric overlap time $\tau_{\text{transit}} \sim L_{\text{env}}/c_g$ far exceeds the wave period. The decorrelation time is set not by this overlap duration but by phase decorrelation. As the energy trajectory advances by one eddy diameter, the advected phase $\exp(i\mathbf{q}_h \cdot \mathbf{c}_g t)$ completes an $\mathcal{O}(1)$ rotation, and successive patches contribute to the Green-Kubo integral with randomised phases (Section A).

Two limiting models for the force decorrelation illuminate the physics. In the frozen-turbulence limit ($\delta \ll 1$), the eddy does not evolve during the encounter and the force autocorrelation at scale q reduces to a spatial correlation sampled at rate c_g , $C_{F,q}(t) \approx C_{F,q}(0) \mathcal{R}(qc_g t)$. The Green-Kubo integral then gives $\tau_{\text{eff}} = C_\tau/(qc_g)$ directly. This is the model adopted throughout. An alternative retains the intrinsic temporal decay $R(q, t) = \exp[-t/\tau_{\text{eddy}}(q)]$, giving a Lorentzian weight

$$\int_0^\infty dt R(q, t) \cos(\mathbf{q}_h \cdot \mathbf{c}_g t) = \frac{\tau_{\text{eddy}}(q)}{1 + (\mathbf{q}_h \cdot \mathbf{c}_g)^2 \tau_{\text{eddy}}^2(q)}. \quad (\text{S.106})$$

In the sweep-dominated regime $|\mathbf{q}_h \cdot \mathbf{c}_g| \tau_{\text{eddy}} \gg 1$, this reduces to $\propto \varepsilon^{1/3} q^{-4/3} c_g^{-2}$, carrying a different q -scaling from the spatial-correlation result $\propto q^{-1} c_g^{-1}$. The two models describe different physics. The temporal-decay model treats the eddy as decaying exponentially, with advection modulating the phase. The spatial model treats the eddy as frozen, with decorrelation arising entirely from spatial sampling. For swell ($\delta \sim 10^{-3}\text{-}10^{-2}$), the eddy barely evolves during the encounter and the frozen-field model is accurate to $\mathcal{O}(\delta)$. The temporal-decay model would apply in the opposite slow-probe limit $\tau_{\text{adv}} \gg \tau_{\text{eddy}}$, which does not hold for ocean swell.

F. Reduced one-dimensional integral and modal normalisation

Combining the direction-averaged vertex (Eqs. (S.94) and (S.97)), the advection-dominated correlation time $\tau_{\text{eff}} \simeq C_\tau/(q c_g)$ (Eq. (S.105)), and converting to the one-dimensional spectrum $E_u(q) = 4\pi q^2 S_u(q)$, the Green-Kubo expression (S.102) reduces to

$$\Gamma(k) = \frac{C_\tau \tilde{G}_{\text{geom}} C_E(k)}{2 c_g(k)} \int_0^\infty dq E_u(q) q \mathcal{S}\left(\frac{q}{k}\right). \quad (\text{S.107})$$

The dimensionless depth-overlap coefficient $C_E(k)$ collects the dependence on the vertical structure and modal normalisation of the swell eigenfunction. For deep-water linear orbits $\mathbf{u}_\phi(z) \propto e^{kz}$, the depth-integrated orbital kinetic energy per unit horizontal area is

$$\int_{-\infty}^0 \langle |\mathbf{u}_\phi(z)|^2 \rangle_t dz = \frac{(a\omega)^2}{2k} = \frac{1}{2} a^2 g = E_k, \quad (\text{S.108})$$

using $\omega^2 = gk$ and the convention $E_k = \frac{1}{2}ga^2$ (equivalently $\frac{1}{2}|a_k|^2$ under A1). The depth-overlap coefficient is defined as

$$C_E(k) \equiv \frac{\int_{-\infty}^0 \langle |\mathbf{u}_\phi(z)|^2 \rangle_t dz}{E_k} = 1 \quad (\text{deep-water linear orbits}). \quad (\text{S.109})$$

The cancellation works as follows. The surface-value ratio $U_0^2/(2E_k) = \omega^2/g = k$ from the Green-Kubo normalisation and vertex is exactly compensated by the k^{-1} from the depth integral, leaving no residual k -dependence in the prefactor. Departures from the ideal exponential profile (finite depth, finite mixed-layer thickness, or modified orbital structure) renormalise C_E to an $\mathcal{O}(1)$ value absorbed into C_{tot} in Section S5.

S4. From the force autocorrelation to the swell attenuation law

In the inertial subrange the velocity spectrum takes the Kolmogorov form [32]

$$E_u(q) = C_K \varepsilon_{\text{eff}}^{2/3} q^{-5/3}, \quad (\text{S.110})$$

with $C_K \approx 1.5$ [37, 45]. For 14 s swell ($k \approx 0.021 \text{ rad m}^{-1}$) in a typical mixed layer ($L_0 \sim 10\text{-}100 \text{ m}$, Kolmogorov microscale $\eta \sim 1 \text{ mm}$), the separation $\eta \ll k^{-1} \lesssim L_0$ places the swell-interacting eddies within the inertial subrange (Section S5 G). Inserting Eq. (S.110) into the one-dimensional Green-Kubo form (S.107) and changing variables $x = q/k$ yields

$$\int_0^\infty dq q^{-2/3} \mathcal{S}\left(\frac{q}{k}\right) = k^{1/3} \int_0^\infty x^{-2/3} \mathcal{S}(x) dx \equiv k^{1/3} C_S, \quad (\text{S.111})$$

where C_S depends only on the shape of the scale-selection window. For the baseline model $\mathcal{S}(x) = x^2/(1+x^2)^2$, $C_S = \pi/6 \approx 0.52$ (Table S1 in Section S5 B gives other choices). Collecting all order-unity constants into $C_\Gamma \equiv C_\tau C_K C_S \tilde{G}_{\text{geom}} C_E/2$, with $C_E = 1$ for deep-water exponential orbits (Eq. S.109), the temporal damping rate becomes

$$\Gamma(k) \simeq C_\Gamma \frac{\varepsilon_{\text{eff}}^{2/3}}{c_g(k)} k^{1/3}. \quad (\text{S.112})$$

Converting to spatial decay via $\mu_E = 2\Gamma/c_g$ (the factor 2 reflects energy \propto amplitude²) and using $c_g = \frac{1}{2}\sqrt{g/k}$ gives $c_g^{-2} = 4k/g$, so

$$\mu_E(k) = 8C_\Gamma \varepsilon_{\text{eff}}^{2/3} \frac{k^{4/3}}{g}. \quad (\text{S.113})$$

Substituting $k = \omega^2/g$ yields the scaling law announced in the main text,

$$\mu_E(\omega) \simeq C_{\text{tot}} \varepsilon_{\text{eff}}^{2/3} g^{-7/3} \omega^{8/3}, \quad C_{\text{tot}} = 8C_\Gamma = 4C_K \tilde{G}_{\text{geom}} C_S C_\tau C_E. \quad (\text{S.114})$$

The $\omega^{8/3}$ exponent combines $k^{1/3}$ from the Kolmogorov spectrum at the swell-selected scale, k^1 from the temporal-to-spatial conversion $c_g^{-2} \propto k$, and the deep-water dispersion relation $k = \omega^2/g$. The decomposition of C_{tot} into individually constrained factors is given in Section S5. The effective dissipation rate entering the law is the mode-weighted average over the wave-turbulence interaction layer,

$$\varepsilon_{\text{eff}}(k) \equiv \frac{\int_{-H_{\text{int}}}^0 \varepsilon(z) e^{2kz} dz}{\int_{-H_{\text{int}}}^0 e^{2kz} dz}, \quad (\text{S.115})$$

where $H_{\text{int}}(k) = \min\{1/k, H_{\text{ml}}\}$. The weights e^{2kz} reflect the decay of orbital energy with depth. ε_{eff} is therefore dominated by the upper $\sim (2k)^{-1} \approx 15\text{-}40$ m of the water column. In Section S5 E the wall-law dissipation profile is substituted explicitly, with the depth coordinate measured downward ($z \geq 0$) and kernel e^{-2kz} ; the two conventions are equivalent under $z \rightarrow -z$. Equation (S.114) is the closed-form consequence of the factorised Green-Kubo closure developed in this section. The $\omega^{8/3}$ exponent is fixed by the Kolmogorov power counting, deep-water dispersion, and the advection-dominated memory time. Section S5 quantifies the order-unity uncertainty associated with the window shape, temporal correlator, and vertical structure, which affects only the prefactor.

S5. Order-of-magnitude of the prefactor C_{tot} and robustness of the Kolmogorov closure

The total prefactor in the swell attenuation coefficient decomposes as

$$C_{\text{tot}} = 4 C_K \tilde{G}_{\text{geom}} C_S C_\tau C_E. \quad (\text{S.116})$$

Each factor is evaluated in the subsections below. Under baseline assumptions the product evaluates to $C_{\text{tot}} = 2\pi/3 \approx 2.09$. Propagating the physically constrained ranges yields $C_{\text{tot}} \in [1.10, 3.34]$ (assembled in Section H). The decomposition into C_S , C_τ , C_E and ε_{eff} is a controlled factorised closure rather than an exact theorem when the depth structure of enstrophy depends explicitly on turbulent wavenumber. The purpose of this section is therefore twofold: to assign physically constrained order-unity ranges to each factor, and to show that the resulting uncertainty affects only the prefactor, not the $\omega^{8/3}$ scaling exponent.

A. The geometric vertex factor \tilde{G}_{geom}

The force-autocorrelation expression for the swell attenuation rate (Eq. (S.89)) contains the squared vortex-force vertex

$$|V(\mathbf{q}; k)|^2 \equiv \frac{1}{8\pi^2} \int_0^{2\pi} d\phi \int d\Omega_{\hat{\mathbf{q}}} |\mathbf{u}_\phi(\phi) \times \boldsymbol{\omega}'(\mathbf{q})|^2, \quad (\text{S.117})$$

where the two integrations represent, respectively, an average over the wave phase $\phi = kx - \omega t$ (one full cycle, normalised by 2π) and an average over the direction of the turbulent wavenumber $\hat{\mathbf{q}}$ on the unit sphere (normalised by 4π , appropriate for isotropic turbulence). The geometric vertex factor \tilde{G}_{geom} collects all purely kinematic contributions, so that

$$|V|^2 = \tilde{G}_{\text{geom}} U_0^2 \langle |\boldsymbol{\omega}'|^2 \rangle, \quad (\text{S.118})$$

with $U_0 = a_k \omega_k$ the surface orbital speed and $\langle |\boldsymbol{\omega}'|^2 \rangle$ the local enstrophy. Consider a monochromatic deep-water wave propagating along $+\hat{\mathbf{x}}$ with wavenumber k and frequency ω . At depth $z \geq 0$ (measured downward from the surface) the orbital velocity is

$$\mathbf{u}_\phi(z, \phi) = U_0 e^{-kz} (\cos \phi \hat{\mathbf{x}} + \sin \phi \hat{\mathbf{z}}), \quad \phi = kx - \omega t. \quad (\text{S.119})$$

The motion is circularly polarised in the x - z plane. Horizontal and vertical amplitudes are equal at every depth. The phase-averaged second-moment tensor is

$$M_{ij} \equiv \langle u_{\phi,i} u_{\phi,j} \rangle_\phi = \frac{U_0^2}{2} (\hat{x}_i \hat{x}_j + \hat{z}_i \hat{z}_j) = \frac{U_0^2}{2} (\delta_{ij} - \hat{y}_i \hat{y}_j), \quad (\text{S.120})$$

whose trace is $M_{ii} = U_0^2$. The vanishing of M_{yy} reflects the absence of any $\hat{\mathbf{y}}$ component in deep-water orbits. This asymmetry is the root cause of the $\{1, \frac{1}{2}, \frac{1}{2}\}$ vorticity weights derived

next. Let $\boldsymbol{\omega}' = (\omega'_x, \omega'_y, \omega'_z)$ denote the turbulent vorticity. The vortex force $\mathbf{F} = \mathbf{u}_\phi \times \boldsymbol{\omega}'$ has components

$$\mathbf{F} = U_0 \begin{pmatrix} -\sin \phi \omega'_y \\ \sin \phi \omega'_x - \cos \phi \omega'_z \\ \cos \phi \omega'_y \end{pmatrix}. \quad (\text{S.121})$$

Since $\langle \mathbf{u}_\phi \rangle_\phi = \mathbf{0}$ for a monochromatic wave, the phase-averaged force vanishes identically,

$$\langle \mathbf{u}_\phi \times \boldsymbol{\omega}' \rangle_\phi = \langle \mathbf{u}_\phi \rangle_\phi \times \boldsymbol{\omega}' = \mathbf{0}, \quad (\text{S.122})$$

consistent with the identification of \mathbf{f}_{svf} as a zero-mean stochastic force (Section S1). The Green-Kubo relation (S.79), however, involves the autocorrelation $\langle F_k(0) F_k^*(t) \rangle$, a second-order quantity whose zero-lag value is set by the phase-averaged squared amplitude $\langle |\mathbf{F}|^2 \rangle_\phi$, which we evaluate. Expanding the squared norm gives

$$|\mathbf{F}|^2 = U_0^2 [\omega_y'^2 + \sin^2 \phi \omega_x'^2 + \cos^2 \phi \omega_z'^2 - 2 \sin \phi \cos \phi \omega_x' \omega_z']. \quad (\text{S.123})$$

The phase averages $\langle \sin^2 \phi \rangle_\phi = \langle \cos^2 \phi \rangle_\phi = \frac{1}{2}$ and $\langle \sin \phi \cos \phi \rangle_\phi = 0$ then give the central intermediate result,

$$\langle |\mathbf{u}_\phi \times \boldsymbol{\omega}'|^2 \rangle_\phi = U_0^2 \left[\omega_y'^2 + \frac{1}{2} (\omega_x'^2 + \omega_z'^2) \right]. \quad (\text{S.124})$$

Equation (S.124) holds for arbitrary turbulence statistics. It depends only on the deep-water dispersion relation through the polarisation of \mathbf{u}_ϕ . The origin of the unequal weights $\{1, \frac{1}{2}, \frac{1}{2}\}$ for the components $\{\omega_y', \omega_x', \omega_z'\}$ is purely geometric. The out-of-plane component ω_y' is perpendicular to the orbital plane $\text{span}\{\hat{\mathbf{x}}, \hat{\mathbf{z}}\}$ at every phase, so it always produces a force and enters with full weight. The component ω_x' , by contrast, is parallel to \mathbf{u}_ϕ when $\phi = 0$ (no cross product) and perpendicular when $\phi = \pi/2$ (maximal cross product). Averaging over the wave cycle yields a factor of one half. The same argument with $x \leftrightarrow z$ applies to ω_z' . For later use we note the equivalent tensor form obtained from the identity $|\mathbf{a} \times \mathbf{b}|^2 = |\mathbf{a}|^2 |\mathbf{b}|^2 - (\mathbf{a} \cdot \mathbf{b})^2$,

$$\langle |\mathbf{u}_\phi \times \boldsymbol{\omega}'|^2 \rangle_\phi = M_{ii} \omega_j' \omega_j' - M_{ij} \omega_i' \omega_j' = U_0^2 |\boldsymbol{\omega}'|^2 - \frac{U_0^2}{2} (\omega_x'^2 + \omega_z'^2), \quad (\text{S.125})$$

which recovers Eq. (S.124) upon expanding $|\boldsymbol{\omega}'|^2 = \omega_x'^2 + \omega_y'^2 + \omega_z'^2$. For homogeneous, isotropic turbulence $\langle \omega_x'^2 \rangle = \langle \omega_y'^2 \rangle = \langle \omega_z'^2 \rangle = \frac{1}{3} \langle |\boldsymbol{\omega}'|^2 \rangle$. Substituting into Eq. (S.124),

$$\langle |\mathbf{u}_\phi \times \boldsymbol{\omega}'|^2 \rangle_{\phi, \text{iso}} = U_0^2 \langle |\boldsymbol{\omega}'|^2 \rangle \left[\frac{1}{3} + \frac{1}{2} \left(\frac{1}{3} + \frac{1}{3} \right) \right] = \frac{2}{3} U_0^2 \langle |\boldsymbol{\omega}'|^2 \rangle, \quad (\text{S.126})$$

and comparing with Eq. (S.118) immediately yields

$$\tilde{G}_{\text{geom}}^{(\text{iso})} = \frac{2}{3}. \quad (\text{S.127})$$

As an independent check we re-derive the isotropic result in wavenumber space. For an isotropic vorticity field the spectral tensor is

$$\Phi_{ij}(\mathbf{q}) \equiv \langle \omega_i'(\mathbf{q}) \omega_j'^*(\mathbf{q}) \rangle = \frac{E_\omega(q)}{4\pi} (\delta_{ij} - \hat{q}_i \hat{q}_j), \quad (\text{S.128})$$

where $E_\omega(q) = q^2 E_u(q)$ is the enstrophy spectrum. Combining Eq. (S.125) with (S.128), the phase-averaged vertex at a fixed turbulent-wavenumber direction $\hat{\mathbf{q}}$ is $g(\hat{\mathbf{q}}) = M_{ii} \Phi_{jj} - M_{ij} \Phi_{ij}$. Writing $A \equiv E_\omega/(4\pi)$, we obtain

$$g(\hat{\mathbf{q}}) = AU_0^2 \left(\frac{3}{2} - \frac{1}{2} \hat{q}_y^2 \right). \quad (\text{S.129})$$

Integrating over the unit sphere ($\int d\Omega_q = 4\pi$, $\int \hat{q}_y^2 d\Omega_q = 4\pi/3$) and normalising by the spectral enstrophy $\langle |\omega'|^2 \rangle_q = 4\pi \text{Tr } \Phi = 8\pi A$ gives $\tilde{G}_{\text{geom}} = (16\pi/3)/(8\pi) = 2/3$, confirming the physical-space value (S.127). Mixed-layer turbulence is not perfectly isotropic. Vertical motions are suppressed relative to horizontal ones by buoyancy and the free surface [46, 47]. We model this through an axisymmetric vorticity variance tensor,

$$\langle \omega'_x{}^2 \rangle = \langle \omega'_y{}^2 \rangle \equiv \sigma_h^2, \quad \langle \omega'_z{}^2 \rangle \equiv \sigma_v^2, \quad \langle \omega'_i \omega'_j \rangle = 0 \quad (i \neq j), \quad (\text{S.130})$$

with the anisotropy ratio $R_u \equiv u'_h/u'_v \approx \sigma_h/\sigma_v$ [48]. Inserting into Eq. (S.124) and normalising by $\langle |\omega'|^2 \rangle = 2\sigma_h^2 + \sigma_v^2$ gives

$$\tilde{G}_{\text{geom}}(R_u) = \frac{3R_u^2 + 1}{2(2R_u^2 + 1)}. \quad (\text{S.131})$$

As an independent verification we parametrise the directional enstrophy spectrum by $S_\omega(\mathbf{q}) = [E_\omega(q)/(4\pi)][1 + \beta P_2(\cos \theta_q)]$ with $P_2(x) = (3x^2 - 1)/2$. The velocity anisotropy relates to the spectral parameter via

$$\beta = \frac{10(R_u^2 - 1)}{2R_u^2 + 1}. \quad (\text{S.132})$$

Evaluating the weighted solid-angle integral with the four angular moments ($\int d\Omega = 4\pi$, $\int P_2 d\Omega = 0$, $\int \hat{q}_y^2 d\Omega = 4\pi/3$, $\int \hat{q}_y^2 P_2 d\Omega = -4\pi/15$) and normalising recovers exactly Eq. (S.131). At $R_u = 1$ (isotropy) we recover $\tilde{G}_{\text{geom}} = 2/3$. As $R_u \rightarrow \infty$ (purely horizontal turbulence) the factor saturates at 3/4, while $R_u \rightarrow 0$ (purely vertical turbulence) gives 1/2. Circular polarisation therefore confines \tilde{G}_{geom} to the narrow interval [1/2, 3/4]. For comparison, a hypothetical linearly polarised wave gives a wider range [1/2, 1]. In the upper ocean, $R_u \sim 1$ -2 [46, 47], over which \tilde{G}_{geom} varies from 0.667 to $\simeq 0.722$, an $\mathcal{O}(8\%)$ shift. Two further effects, finite-depth elliptical polarisation and wind-swell obliquity, can each perturb \tilde{G}_{geom} by $\sim 10\%$ for a single realisation, but average out over trans-basin propagation. We adopt $\tilde{G}_{\text{geom}} = 2/3$ with a physical range [2/3, 3/4] for deep-water swell.

B. The scale-selection constant C_S

The scale-selection window $\mathcal{S}(q/k)$ derived in Section D enters the scaling law only through the dimensionless integral $C_S = \int_0^\infty x^{-2/3} \mathcal{S}(x) dx$ (Eq. S.111). Its shape-peak at $q \sim k$, infrared growth $\propto x^2$, ultraviolet roll-off-is fixed by wave-eddy geometry. Its amplitude depends on the vertical distribution of mixed-layer enstrophy, parameterised here by a single exponent. Because every admissible window shares the same infrared ($\mathcal{S} \propto x^2$) and ultraviolet ($\mathcal{S} \lesssim Cx^{-1}$) asymptotics, the integrand $x^{-2/3} \mathcal{S}(x)$ is unconditionally convergent at both ends and the change of variables $x = q/k$ always extracts the factor $k^{1/3}$ that produces the $\omega^{8/3}$ exponent (Eq. S.111). Varying the window shape therefore changes only the numerical value of C_S , not the scaling law itself. We adopt the rational family

$$\widehat{W}_\alpha(x) = \frac{x^2}{(1+x^2)^\alpha}, \quad \alpha \geq \frac{3}{2}, \quad (\text{S.133})$$

whose ultraviolet behaviour is $\widehat{W}_\alpha \sim x^{2-2\alpha}$ as $x \rightarrow \infty$. The constraint $\alpha \geq 3/2$ ensures convergence, matching the theorem-level floor $\mathcal{S} \lesssim Cx^{-1}$ proved in Section D. Each value of α corresponds to a distinct assumption about turbulent enstrophy depth structure. At $\alpha = 3/2$ the enstrophy profile $\chi_q(z)$ is independent of q , corresponding to a local-equilibrium cascade with depth-independent spectral shape ($\chi_q \propto \varepsilon(z)^{2/3} \propto z^{-2/3}$, so q and z separate completely and UV suppression arises solely from the angular-cap geometry). At $\alpha = 2$ the profile acquires q -dependent depth confinement, $\chi_q(z) \propto e^{-qz}$, as expected when turbulence is injected at the surface by wave breaking and wind stress rather than locally by shear [38]. At $\alpha = 5/2$ the

surface concentration is stronger still, as may arise, for example, from Langmuir circulations [10, 39].

Table S1: Scale-selection window comparison. Each row lists the ultraviolet behaviour, the physical assumption, the coupling constant C_S , the fraction captured by the band $x \in [0.5, 2]$, and the peak of the spectral contribution density $x^{1/3}\widehat{W}(x)$.

Window	UV decay	Physical assumption	C_S	$[k/2, 2k]$	x_{peak}
$\alpha = 3/2$ (floor)	x^{-1}	Local-equilibrium cascade; χ_q independent of q	1.40	35%	1.9
$\alpha = 2$ (baseline)	x^{-2}	Surface-injected turbulence; $\chi_q \propto e^{-qz}$	$\pi/6 \approx 0.52$	58%	1.2
$\alpha = 5/2$	x^{-3}	Strong surface concentration	0.31	66%	0.9
Top-hat $[\frac{1}{2}, 2]$	cutoff	Artificial (no UV tail)	1.40	-	~ 1

Analytical evaluation for $\alpha = 2$. The substitution $t = x^2$ converts the baseline integral to a Beta function,

$$C_S^{(\alpha=2)} = \int_0^\infty \frac{x^{4/3}}{(1+x^2)^2} dx = \frac{1}{2} B\left(\frac{7}{6}, \frac{5}{6}\right). \quad (\text{S.134})$$

With $a + b = 2$ and the reflection formula $\Gamma(z)\Gamma(1-z) = \pi/\sin(\pi z)$,

$$B\left(\frac{7}{6}, \frac{5}{6}\right) = \frac{1}{6} \Gamma\left(\frac{1}{6}\right) \Gamma\left(\frac{5}{6}\right) = \frac{\pi}{3 \sin(\pi/6)} = \frac{\pi}{3}, \quad (\text{S.135})$$

giving the exact result

$$C_S^{(\alpha=2)} = \frac{\pi}{6} \approx 0.5236. \quad (\text{S.136})$$

Between $\alpha = 3/2$ (floor) and $\alpha = 2$ (baseline), C_S varies by a factor of 2.7. Between the two physically motivated shapes $\alpha = 2$ and $5/2$ it varies by only a factor of 1.7. The near-coincidence $C_S^{(\alpha=3/2)} \approx C_S^{(\text{top-hat})} = 1.40$ is accidental. The top-hat concentrates all weight inside $[k/2, 2k]$, while $\alpha = 3/2$ has a modest peak ($\widehat{W}(1) \approx 0.35$) but a fat UV tail—fully 65% of its integral comes from $x > 2$. The theorem floor therefore overestimates the UV contribution by attributing full inertial-range vorticity to depths where surface-injected turbulence has not penetrated.

The spectral contribution density $x^{1/3}\widehat{W}_\alpha(x)$ peaks at $x_{\text{peak}} = \sqrt{7/(6\alpha - 7)}$, confirming that the dominant coupling shifts toward $q \sim k$ as α increases. For the physically motivated choices ($\alpha \geq 2$), the band $x \in [0.5, 2]$ captures 58-66% of the integral, confirming that wave-scale eddies dominate the energy transfer.

C. The advective correlation factor C_τ

After angular averaging and factorisation of the geometric vertex, the damping rate contains the effective correlation time

$$\tau_{\text{eff}}(q; k) \equiv \frac{C_\tau}{q c_g(k)}, \quad (\text{S.137})$$

where $c_g(k)$ is the swell group velocity and C_τ is dimensionless and of order unity. Remote swell propagates at $c_g \sim 10\text{-}20 \text{ ms}^{-1}$, far exceeding the turbulent velocity $u'(q) \sim 0.01\text{-}0.1 \text{ ms}^{-1}$. The wave-energy trajectory traverses one spatial period of each turbulent Fourier mode long before the eddy turns over ($\tau_{\text{adv}}/\tau_{\text{eddy}} \sim 10^{-3}\text{-}10^{-2}$), so decorrelation is controlled by relative advection—the wave-propagation analogue of Kraichnan-Tennekes random sweeping [43, 44].

The correlation function for wavenumber shell q is $C_{F,q}(t) \approx C_{F,q}(0) \mathcal{R}(q c_g t)$, where $\mathcal{R}(s)$ is a self-similar normalised spatial correlation with $\mathcal{R}(0) = 1$. Changing variables gives

$$C_\tau = \int_0^\infty \mathcal{R}(s) ds, \quad (\text{S.138})$$

which is necessarily of order unity. An exponential $\mathcal{R}(s) = e^{-s}$ gives $C_\tau = 1$. A Gaussian e^{-s^2} gives $C_\tau = \sqrt{\pi}/2 \approx 0.89$. The broader Gaussian $e^{-s^2/2}$ gives $C_\tau \approx 1.25$. The physical range is $C_\tau \in [0.89, 1.25]$, contributing $\sim 20\%$ variation compared with the order-of-magnitude uncertainty in ε_{eff} . We adopt $C_\tau = 1$ as the baseline.

D. The vertical-weighting factor C_E

The factor C_E relates the depth-integrated orbital kinetic energy to the modal energy per unit density,

$$C_E \equiv \frac{\int_{-\infty}^0 |\mathbf{u}_\phi(z)|^2 dz}{E_k} = 1 \quad (\text{deep water}). \quad (\text{S.139})$$

This is exact for $\mathbf{u}_\phi(z) \propto e^{kz}$ with $E_k = \frac{1}{2}ga^2$. For the far-field deep-water swell regime considered throughout this work, deviations from the ideal exponential eigenfunction are negligible.

E. Effective dissipation rate and numerical baseline

Collecting all prefactors (Eq. S.114), the baseline values $C_S = \pi/6$, $C_\tau = 1$, $C_E = 1$, $\tilde{G}_{\text{geom}} = 2/3$ and $C_K = 1.5$ give

$$C_\Gamma = \frac{C_\tau C_K C_S \tilde{G}_{\text{geom}} C_E}{2} \simeq 0.26, \quad C_{\text{tot}} = 8C_\Gamma = \frac{2\pi}{3} \simeq 2.09. \quad (\text{S.140})$$

The effective dissipation rate entering the scaling law is the depth-weighted average of $\varepsilon(z)$ over the orbital layer. Equation (S.115) in Section S4 gives the formal definition over the full interaction layer; the operational form below restricts the lower limit to z_0 (the breaking-layer exclusion depth) and works in the depth-downward convention used for dissipation profiles. With $z \geq 0$ measured downward from the surface (equivalent to the $z \leq 0$ convention of Sections S3-S4 under $z \rightarrow -z$),

$$\varepsilon_{\text{eff}}(k) = \frac{\int_{z_0}^{H_{\text{ml}}} \varepsilon(z) e^{-2kz} dz}{\int_{z_0}^{H_{\text{ml}}} e^{-2kz} dz}, \quad (\text{S.141})$$

where the kernel e^{-2kz} reflects the orbital-energy decay with e -folding depth $\delta_E = 1/(2k)$. For 14 s swell ($k \approx 0.021 \text{ m}^{-1}$), $\delta_E \approx 24 \text{ m}$. When $H_{\text{ml}} \gg \delta_E$ and $2kz_0 \ll 1$,

$$\varepsilon_{\text{eff}}(k) \approx 2k \int_{z_0}^\infty \varepsilon(z) e^{-2kz} dz \quad (\text{S.142})$$

to within a few percent. Since $\varepsilon_{\text{eff}} \propto u_*^{(w)3} \propto C_D^{3/2}$ and $\Gamma \propto \varepsilon_{\text{eff}}^{2/3}$, the exponents cancel to give $\Gamma \propto C_D$. A fractional error in the drag coefficient translates one-to-one into Γ . Stress continuity across the air-sea interface gives

$$u_*^{(w)} = U_{10} \sqrt{C_D} \sqrt{\rho_a/\rho_w} \approx U_{10} \sqrt{C_D} \times 0.035, \quad (\text{S.143})$$

with $\rho_a/\rho_w \approx 1.2 \times 10^{-3}$. We adopt the COARE 3.5 parameterisation [49] as the baseline. At $U_{10} = 10 \text{ m s}^{-1}$, COARE 3.5 gives $C_D \approx 1.15 \times 10^{-3}$ and $u_*^{(w)} \approx 1.17 \times 10^{-2} \text{ m s}^{-1}$. Alternative

bulk-flux formulations [50–52] give C_D from 1.08 to 1.47×10^{-3} , corresponding to $\Delta\Gamma/\Gamma$ between -6% and $+28\%$. For moderate winds ($5 \leq U_{10} \leq 20 \text{ m s}^{-1}$), COARE 3.5 is well approximated by $C_D \approx (0.065 U_{10} + 0.49) \times 10^{-3}$. Below the wave-breaking layer ($z > z_0$), the dissipation rate follows the law of the wall,

$$\varepsilon(z) = \frac{u_*^{(w)3}}{\kappa z}, \quad z > z_0 = c_b H_{s,w}, \quad (\text{S.144})$$

with $\kappa = 0.4$ and $c_b \approx 0.6$ ($z_0 \approx 0.9 \text{ m}$ for $H_s = 1.5 \text{ m}$). Substituting into (S.142) gives

$$\varepsilon_{\text{eff}}(k) = 2k \frac{u_*^{(w)3}}{\kappa} E_1(2k z_0), \quad (\text{S.145})$$

where $E_1(x) = \int_x^\infty t^{-1} e^{-t} dt$. For 14 s swell with $z_0 = 0.9 \text{ m}$, $2k z_0 \approx 0.037$ and $E_1(0.037) \approx 2.76$, giving

$$\varepsilon_{\text{eff}} \approx 2 \times 0.021 \times \frac{(1.17 \times 10^{-2})^3}{0.4} \times 2.76 \approx 4.6 \times 10^{-7} \text{ m}^2 \text{ s}^{-3}. \quad (\text{S.146})$$

The logarithmic approximation $E_1(x) \approx -\gamma_E - \ln x$ for $x \ll 1$ gives the closed form

$$\varepsilon_{\text{eff}} \approx 2k \frac{u_*^{(w)3}}{\kappa} [-\gamma_E - \ln(2k z_0)], \quad (\text{S.147})$$

with error less than 2% for $2k z_0 < 0.1$. The result is insensitive to z_0 . A fourfold variation from 0.5 to 2.0 m changes ε_{eff} by a factor of ~ 1.7 , following from the logarithmic dependence. The drag coefficient is typically the dominant source of uncertainty in large-scale applications.

Near-surface dissipation rates under active wind-wave breaking exceed the wall-law prediction by up to an order of magnitude. The Craig-Banner and Terray models [20, 21] parametrise the breaking-layer TKE flux as $F_0 = \alpha u_*^{(w)3}$ with $\alpha \sim 50\text{-}150$, producing a three-layer vertical structure (Extended Data Fig. 2a). A constant-dissipation layer at $z < z_b \approx 0.6 H_{s,w}$, a power-law decay layer $\varepsilon \propto z^{-\lambda}$ ($\lambda \approx 1.5\text{-}2$) extending to $z_t \approx c_1 H_{s,w}$, and an asymptotic return to wall-law scaling at greater depth [21, 53]. Here $H_{s,w}$ is the significant height of the *local wind-wave* field that generates the breaking. For $U_{10} = 10 \text{ m s}^{-1}$ the Pierson-Moskowitz limit gives $H_{s,w} \approx 2.2 \text{ m}$, $z_b \approx 1.3 \text{ m}$ and $z_t \approx 9 \text{ m}$ (taking $c_1 \approx 4$ from the wave-following observations of Thomson et al. 53, Sutherland and Melville 54). The resulting surface enhancement is a factor ~ 7 relative to the wall-law.

The question is whether this enhancement should be included in ε_{eff} . Within the present factorised closure, doing so would effectively double-count the spectral filtering already performed by the scale-selection integral C_S . The full Green-Kubo damping coefficient is a coupled integral over eddy wavenumber q and depth z (Eq. S.148). The factored form $\Gamma \propto C_S \varepsilon_{\text{eff}}^{2/3}$ is valid when the depth-weighted dissipation entering ε_{eff} is produced by eddies at wavenumbers $q \sim k$ that receive full weight from the window $\widehat{W}(q/k)$. The wall-law profile, having no characteristic depth scale, satisfies this condition. The Kolmogorov inertial range at every depth feeds all wavenumbers q equally per unit log-interval, and the spectral integral C_S correctly selects the swell-scale contribution.

The breaking-generated eddies violate this condition. Their injection scales are set by the local wind-wave geometry: $\ell_b \sim \mathcal{O}(H_{s,w}) \sim 2 \text{ m}$, corresponding to wavenumbers $q_b \sim 2\pi/\ell_b \sim 1\text{-}6 \text{ rad m}^{-1}$. Relative to the swell wavenumber $k \sim 0.02 \text{ rad m}^{-1}$, this gives $q_b/k \sim 50\text{-}300$, deep in the ultraviolet tail of the window where $\widehat{W}(q_b/k) \sim 4 \times 10^{-4}$ (Extended Data Fig. 2b). The scale-selection integral has already assigned these eddies a negligible weight. Including the same eddies a second time via a breaking-enhanced ε_{eff} -while retaining the baseline C_S derived from the full spectral window-would effectively count their contribution twice. An independent argument reinforces this conclusion. The eddy-turnover time in the breaking layer, $\tau_b \sim \ell_b/u'_b \sim \mathcal{O}(T_{\text{wind wave}}) \sim 3\text{-}6 \text{ s}$, is comparable to the swell period, so these eddies do not

satisfy the frozen-field condition $\tau_{\text{eddy}} \gg T_{\text{swell}}$ underlying the SVF framework (Assumption A2). They lie outside the theory's domain of validity.

To bound the residual sensitivity we nevertheless apply the physical-space coupling filter $\mathcal{E}(\ell k) = (\ell k)^2/[1 + (\ell k)^2]$ to both the wall-law and Terray profiles, integrate with the orbital weight e^{-2kz} , and take the ratio. The result ranges from $1.10\times$ at $T = 12\text{ s}$ to $1.02\times$ at $T = 20\text{ s}$ (Extended Data Fig. 2c)-a residual bias of at most 10%, far smaller than the C_{tot} uncertainty ($\times 3$). The wall-law baseline therefore provides the consistent baseline adopted here across the entire far-field swell band. The full three-panel analysis is presented in Extended Data Fig. 2.

F. Self-consistency of window shape and dissipation profile

The factored form $\Gamma = C_{\Gamma} \varepsilon_{\text{eff}}^{2/3} k^{1/3}/|c_g|$ is exact only when the depth and spectral integrals factorise, which requires the normalised enstrophy profile $\chi_q(z)$ to be q -independent. When $\chi_q(z) \propto e^{-qz}$ (as in the real ocean), the full Green-Kubo structure involves a coupled integral

$$\Gamma \propto \int dq q^{-2/3} \underbrace{\int dz e^{-2kz} \varepsilon(z)^{2/3} \chi_q(z)}_{\mathcal{I}(k,q)}, \quad (\text{S.148})$$

and $\mathcal{I}(k, q)$ cannot be cleanly separated into a q -independent depth factor and a spectral window. The current treatment assigns the depth-mismatch effect to the window ($\alpha = 2$) while computing ε_{eff} from the q -independent wall-law profile. Two approximation errors arise but partially compensate. First, by Jensen's inequality the linear depth-average $\langle \varepsilon \rangle^{2/3}$ overestimates the correct $\langle \varepsilon^{2/3} \rangle$ by a factor $\lesssim 1.2$ for the wall-law profile. Second, the physical premise of $\alpha = 2$ (surface-injected turbulence) implies near-surface ε exceeding the wall-law by a factor of ~ 2 -3 [39], which would increase $\varepsilon_{\text{eff}}^{2/3}$ by ~ 1.6 , partially offsetting the window reduction from $C_S = 1.40$ ($\alpha = 3/2$) to $\pi/6$ ($\alpha = 2$). The net effect places the baseline within a factor of ~ 2 of the self-consistent Langmuir-enhanced alternative, and the $\omega^{8/3}$ exponent is unaffected. The wall-law baseline is conservative. It underestimates ε itself, and this dominates the Jensen overestimate, so our predictions represent a lower bound on the attenuation rate.

G. Validity of Kolmogorov scaling at swell-selected eddy scales

The $\omega^{8/3}$ scaling exponent requires Kolmogorov scaling $E_u(q) \propto \varepsilon^{2/3} q^{-5/3}$ only at eddy wavenumbers $q \sim k$, where the dissipation kernel peaks. The spectral contribution density $d\Gamma/d\ln q$ peaks near $q/k \approx 1$, where the eddy horizontal scale matches the orbital penetration depth and geometric overlap is maximised. The half-decade band $0.5 \leq q/k \leq 2$ captures the majority of the total attenuation rate (58-66% depending on window shape). For swell wavelengths $\lambda \approx 200$ -500 m, the selected eddy scales are $\ell_h \approx 30$ -80 m. What must be justified is not a universal $k^{-5/3}$ law for all mixed-layer motions at these scales, but the use of $E_u(q) \propto \varepsilon^{2/3} q^{-5/3}$ over the narrow swell-selected band $q \sim k$ that carries most of the Green-Kubo weight. For typical upper-ocean conditions ($\varepsilon \sim 10^{-8}$ - $10^{-7} \text{ m}^2 \text{ s}^{-3}$, $N \sim 10^{-3} \text{ s}^{-1}$), the Ozmidov wavenumber $k_O = (N^3/\varepsilon)^{1/2} \approx 0.1$ -0.3 rad m^{-1} . The swell-selected wavenumbers $q \sim k \approx (1$ -3) $\times 10^{-2} \text{ rad m}^{-1}$ fall below k_O by roughly one decade. However, the *horizontal* energy spectrum maintains an approximately continuous $\varepsilon^{2/3} k_h^{-5/3}$ form across k_O , without evidence for an order-one break over the swell-selected band. The unified framework of Kunze [55] provides the theoretical basis. This spectral continuity is confirmed by towed ocean microstructure measurements [56], atmospheric data [57], and DNS of stratified turbulence [58, 59]. The orbital penetration depth $1/k \approx 30$ -80 m is comparable to or smaller than the mixed-layer depth, so the interaction occurs predominantly within the surface mixed layer, where the buoyancy frequency is $N_{\text{ml}} \sim 10^{-4} \text{ s}^{-1}$. The local Ozmidov length scale is then $L_O = (\varepsilon/N_{\text{ml}}^3)^{1/2} \approx 300 \text{ m}$, exceeding the orbital penetration depth by a factor of 3-10. The swell-selected eddies therefore reside within the locally isotropic regime

where the standard Kolmogorov spectrum applies without appeal to the Kunze framework. The turbulent Reynolds number

$$\text{Re}_\ell \equiv \frac{\varepsilon^{1/3}}{\nu k^{4/3}} \quad (\text{S.149})$$

is of order 10^6 for 14-s swell, confirming a well-developed inertial subrange at the relevant scales [37]. Within the mixed layer, local isotropy is assured. Below it, the horizontal spectrum maintains the same $\varepsilon^{2/3} k_h^{-5/3}$ form continuously across k_O .

H. Assembly of the total prefactor

Factor	Baseline	Physical range	Source
Numerical coefficient	4	-	deep-water dispersion
C_K	1.5	1.5-1.7	experiments/DNS
\tilde{G}_{geom}	2/3	2/3-3/4	Section A
C_S	$\pi/6 \approx 0.52$	0.31- $\pi/6$	Section B
C_τ	1	0.89-1.25	Section C
C_E	1	1 (deep-water baseline)	Section D
C_{tot}	$2\pi/3 \approx 2.09$	[1.10, 3.34]	Eq. (S.116)

The standard value $C_K = 1.5$ [45] is adopted as the baseline. High-resolution DNS compilations report values up to 1.7 [60]. For circularly polarised deep-water waves with $R_u \sim 1$ -2, the geometric factor is $\tilde{G}_{\text{geom}} \in [2/3, 3/4]$. The coupling constant ranges from $C_S = \pi/6$ (surface-injected turbulence, $\alpha = 2$) to 0.31 (strong surface concentration, $\alpha = 5/2$). The $\alpha = 3/2$ case ($C_S = 1.40$) is retained in Section B as a theorem-level UV-convergence floor, not as the physical upper bound. For the far-field mixed layer the prefactor range is restricted to $\alpha \in [2, 5/2]$. Together with $C_\tau \in [0.89, 1.25]$ and $C_E = 1$,

$$C_{\text{tot}}^{(\text{phys})} \in [4 \times 1.5 \times \frac{2}{3} \times 0.31 \times 0.89, 4 \times 1.7 \times \frac{3}{4} \times \frac{\pi}{6} \times 1.25] \approx [1.10, 3.34]. \quad (\text{S.150})$$

The baseline value $C_{\text{tot}} = 4 \times 1.5 \times (2/3) \times (\pi/6) \times 1 \times 1 = 2\pi/3 \approx 2.09$ sits near the geometric mean of this range. The wider uncertainty compared with the geometric and correlation factors (\tilde{G}_{geom} and C_τ together contribute $< 30\%$ variation) is dominated by the coupling constant C_S , which reflects the physical ambiguity in the UV exponent α .

The distinction between the scaling exponent and the prefactor is central to the theory's predictive status. The $\omega^{8/3}$ exponent follows from the power-counting $-5/3 + 2 - 1 = -2/3$ and the deep-water dispersion relation alone. It is independent of the window shape α , the turbulent correlator, the depth profile of ε , and any $\mathcal{O}(1)$ prefactor. The prefactor $C_{\text{tot}} \in [1.10, 3.34]$ is a controlled parametrisation of the remaining geometric and environmental uncertainties, not a free parameter. Each factor is independently constrained by turbulence measurements, wave kinematics, or analytical integration. The residual prefactor uncertainty is dwarfed by the order-of-magnitude environmental variability in ε_{eff} along real propagation paths (Section E).

S6. Random-walk theory and intrinsic variance closure

Satellite retrievals resolve individual rays and return a finite-length attenuation estimator $\hat{\mu}_i$, rather than the local ensemble-mean rate $\mu_E(\omega)$ that enters the Green-Kubo theory. The distinction matters. μ_E is controlled only by the *integral* of the mode-projected force autocorrelation (equivalently the zero-frequency spectral density $S_F(0)$), whereas the variance of $\hat{\mu}_i$ depends on the *shape* of the autocorrelation through a long-run variance factor (Section B).

Because wave-eddy encounters act multiplicatively on the wave energy and are nearly symmetric ($|\bar{\varepsilon}|/\sigma \sim \delta \ll 1$, Section I), $N \sim 10^5$ encounters accumulate along a trans-oceanic path,

producing a log-energy random walk. Under weak dependence (short-memory mixing), the central-limit statistics yield

$$\hat{\mu}_i \sim \mathcal{N}\left(2\mu_{E,i}, \frac{2\mu_{E,i}}{L_i} \mathcal{R}_i + \sigma_{\text{meas}}^2\right), \quad (\text{S.151})$$

where L_i is the propagation distance, σ_{meas}^2 is an estimator-level additive variance accounting for observational methodology noise (not encounter-level stochastic forcing), and $\mathcal{R}_i = 1$ recovers the near-independent-encounter baseline (with $\mathcal{R}_i \neq 1$ capturing inter-encounter correlations). For homogeneous along-ray conditions the observable mean reduces to $2\mu_{E,i}$. In the data-facing formulation used in the main text and in Section A it is replaced by the path-averaged observable mean $\mu_{\text{model},i}$. The remainder of this section derives the factor of 2 in the mean, the intrinsic variance coefficient c_0 , and its renormalisation by inter-encounter correlations.

A. Random walk in logarithmic energy

Let $E_k(x)$ denote the modal energy of the swell component with wavenumber k along a ray parametrised by distance x . The logarithmic spatial attenuation rate is defined as

$$\hat{\mu} = -\frac{1}{L} \ln \frac{E_k(L)}{E_k(0)}. \quad (\text{S.152})$$

The logarithmic definition retains exact additivity. Multiplicative energy changes along successive segments become additive increments in $\ln E_k$, making it the natural variable for a random-walk formulation. We partition the ray into N segments of length ℓ_{corr} , the advective decorrelation length of the projected vorticity field along the ray ($\ell_{\text{corr}} \sim \tau_c c_g$, comparable to the force correlation length). This length serves as the baseline coarse-graining step. The observable ratio c_0 is independent of this choice (see the coarse-graining remark below Eq. (S.167)). The distinct *integral correlation length* ℓ_{int} of the increment process is introduced in Section B and governs the variance renormalisation when successive increments are not independent.

$$N = \frac{L}{\ell_{\text{corr}}}. \quad (\text{S.153})$$

For swell wavelengths of a few hundred metres and upper-ocean turbulence with integral scales of order tens of metres, $N \sim 10^4$ - 10^5 over a trans-oceanic path. Let

$$\Delta\varepsilon_n \equiv \ln \frac{E_n}{E_{n-1}} \quad (\text{S.154})$$

denote the logarithmic energy increment in the n th segment, so that

$$\hat{\mu} = -\frac{1}{L} \sum_{n=1}^N \Delta\varepsilon_n. \quad (\text{S.155})$$

To connect the random-walk increments to the microscopic force statistics, we introduce the *fractional energy change* per encounter,

$$\xi_n \equiv \frac{\Delta E_n}{E_{n-1}} = \frac{E_n - E_{n-1}}{E_{n-1}}, \quad (\text{S.156})$$

where ΔE_n is the energy change accumulated in the n th segment. The log-energy increment is then

$$\Delta\varepsilon_n = \ln(1 + \xi_n) = \xi_n - \frac{1}{2}\xi_n^2 + \mathcal{O}(\xi_n^3). \quad (\text{S.157})$$

In the weak-coupling limit $\delta \ll 1$, each ξ_n is $\mathcal{O}(\delta)$, so the expansion is well controlled. We compute the mean and variance of ξ through complementary steps. The variance uses only bath

statistics (no FDR), while the mean requires FDR-II from Section S2. Both are then linked through the common integral I_F . During the n th encounter, the wave-energy trajectory traverses one spatial period of the dominant turbulent Fourier mode in the advective decorrelation time $\tau_{\text{adv}} = \ell_{\text{corr}}/c_g$. The modal energy $E_k = \frac{1}{2}|a_k|^2$ (the same convention as Section S2) evolves under the GLE derived in Section S2 (Eq. (S.53)). In the weak-probe limit (A4, $\delta \ll 1$), the mode amplitude varies negligibly during τ_{adv} , and the instantaneous rate of energy change due to the mode-projected stochastic vortex force F_k is

$$\dot{W}_k(t) = \left. \frac{dE_k}{dt} \right|_{\text{SVF}} = \text{Re}[a_k^* F_k(t)]. \quad (\text{S.158})$$

Here $F_k(t) = \int \psi_k^*(\mathbf{x}) \cdot \mathbf{f}_{\text{svf}}(\mathbf{x}, t) d^3x$ is the mode-projected force (Eq. (S.36)), ψ_k is the normalised mode function, and Eq. (S.158) follows from $dE_k/dt = \text{Re}[a_k^* da_k/dt]$ restricted to the SVF contribution. The fractional energy change per encounter is then

$$\xi_n = \frac{1}{E_k} \int_0^{\tau_{\text{adv}}} \dot{W}_k(t) dt = \frac{1}{E_k} \int_0^{\tau_{\text{adv}}} \text{Re}[a_k^* F_k(t)] dt. \quad (\text{S.159})$$

We first compute the variance of ξ_n using only bath statistics (assumptions A3, A5-no FDR-II required). The variance is

$$\text{Var}(\xi) = \frac{1}{E_k^2} \int_0^{\tau_{\text{adv}}} \int_0^{\tau_{\text{adv}}} C_{\dot{W}}(t-t') dt dt', \quad (\text{S.160})$$

where $C_{\dot{W}}(\tau) \equiv \langle \dot{W}_k(0) \dot{W}_k(\tau) \rangle$ is the autocorrelation of the energy transfer rate. We express $C_{\dot{W}}$ in terms of the mode-projected force autocorrelation

$$C_F(\tau) \equiv \langle F_k(0) F_k^*(\tau) \rangle. \quad (\text{S.161})$$

From (S.158),

$$C_{\dot{W}}(\tau) = \langle \text{Re}[a_k^* F_k(0)] \text{Re}[a_k^* F_k(\tau)] \rangle. \quad (\text{S.162})$$

To evaluate this, we use the identity $\text{Re}(z_1) \text{Re}(z_2) = \frac{1}{2} \text{Re}(z_1 z_2^*) + \frac{1}{2} \text{Re}(z_1 z_2)$ with $z_1 = a_k^* F_k(0)$ and $z_2 = a_k^* F_k(\tau)$,

$$z_1 z_2^* = |a_k|^2 F_k(0) F_k^*(\tau), \quad \langle z_1 z_2^* \rangle = 2E_k C_F(\tau), \quad (\text{S.163})$$

$$z_1 z_2 = (a_k^*)^2 F_k(0) F_k(\tau), \quad \langle z_1 z_2 \rangle = 0. \quad (\text{S.164})$$

The vanishing of the second average requires care because F_k itself is proportional to a_k (through the orbital velocity $\mathbf{u}_\phi \propto a_k$ in the SVF). Writing $F_k(t) = a_k \eta_k(t)$ where η_k depends only on the bath, one has $z_1 z_2 = |a_k|^4 \eta_k(0) \eta_k(\tau)$, and the question reduces to whether the pseudo-correlation $\langle \eta_k(0) \eta_k(\tau) \rangle$ vanishes. It does, as a hard symmetry consequence of real-valuedness and translational invariance of a homogeneous bath field, not as an assumption about the wave phase. Specifically, η_k is the Fourier coefficient at wavevector $\mathbf{k} \neq \mathbf{0}$ of a real, statistically homogeneous field along the ray. For an ideal plane-wave mode in a strictly homogeneous bath, $\langle \hat{X}_{\mathbf{k}} \hat{X}_{\mathbf{k}'} \rangle \propto \delta(\mathbf{k} + \mathbf{k}')$ (pseudo-spectrum), whereas $\langle \hat{X}_{\mathbf{k}} \hat{X}_{\mathbf{k}'}^* \rangle \propto \delta(\mathbf{k} - \mathbf{k}')$ (Hermitian spectrum). Setting $\mathbf{k}' = \mathbf{k} \neq \mathbf{0}$ yields $\delta(2\mathbf{k}) = 0$ and hence $\langle \eta_k(0) \eta_k(\tau) \rangle = 0$. For a finite-bandwidth wave packet, the pseudo-correlation is not identically zero but is suppressed by the spectral bandwidth ratio $\Delta k/k \ll 1$ (narrow-band assumption A1). It therefore contributes only at higher order in the weak-coupling expansion. The complex process η_k is therefore *proper* (circularly symmetric) to leading order, and the pseudo-correlation is negligible as a consequence of translational invariance and narrow bandwidth-not as an assumption about the wave phase.³ Substituting (S.163)-(S.164)

³In the ideal plane-wave limit, the pseudo-spectral density $S_{\eta\eta}(\omega) = \int \langle \eta_k(0) \eta_k(\tau) \rangle e^{i\omega\tau} d\tau$ vanishes identically for $k \neq 0$, which is the standard properness condition for complex Fourier modes of a real homogeneous field. For finite bandwidth, the residual scales as $\mathcal{O}(\Delta k/k)$ and is therefore negligible at leading order in the joint narrow-band ($\Delta k/k \ll 1$) and weak-coupling ($\delta \ll 1$) approximation adopted throughout.

into (S.162),

$$\boxed{C_{\dot{W}}(\tau) = E_k \operatorname{Re} C_F(\tau)}. \quad (\text{S.165})$$

This is the key bridge equation. $\dot{W}_k = \operatorname{Re}[a_k^* F_k]$ is bilinear in the mode amplitude and the bath force. The properness identity contributes $|a_k|^2 = 2E_k$ from $\langle z_1 z_2^* \rangle$, while the factor $\frac{1}{2}$ from $\operatorname{Re}(z_1) \operatorname{Re}(z_2) = \frac{1}{2} \operatorname{Re}(z_1 z_2^*) + \dots$ gives the net coefficient E_k . Inserting (S.165) into (S.160) and applying the Green-Kubo long-time approximation (see the coarse-graining remark below),

$$\begin{aligned} \operatorname{Var}(\xi) &= \frac{1}{E_k^2} 2\tau_{\text{adv}} \int_0^\infty C_{\dot{W}}(\tau) \, d\tau \\ &= \frac{1}{E_k^2} 2\tau_{\text{adv}} E_k \underbrace{\int_0^\infty \operatorname{Re} C_F(\tau) \, d\tau}_{\equiv I_F} \\ &= \frac{2\tau_{\text{adv}} I_F}{E_k}. \end{aligned} \quad (\text{S.166})$$

Writing $\operatorname{Var}(\xi) = \beta_\xi \delta^2$,

$$\beta_\xi = \frac{2\tau_{\text{adv}} I_F}{E_k \delta^2}. \quad (\text{S.167})$$

Independence of the coarse-graining scale. The identification of one step with ℓ_{corr} is a coarse-graining convenience. More generally, define a mesoscale step of length $L_0 \gg c_g \tau_c$, with duration $\Delta t = L_0/c_g \gg \tau_c$. Both the mean and variance of the cumulative increment scale linearly with Δt , so in the observable ratio $c_0 = \sigma_{\delta\mu}^2 L / \langle \hat{\mu} \rangle$ the arbitrary length L_0 cancels identically. Hence $c_0 = D/\Gamma$ is a property of the force-autocorrelation shape, not of the chosen step size. We may set $L_0 = \ell_{\text{corr}}$ without affecting the result.

So far, only stationarity (A3 (i)), factorisation (A5), and rapid decorrelation (A6) have been used. The mean of ξ requires FDR-II (Eq. (S.39)) and the Markov limit (Section S2 G). The ensemble-mean energy evolution in the Markov limit is (Eq. (S.68)),

$$\frac{d}{dt} \langle E_k \rangle = -2\Gamma(k) \langle E_k \rangle, \quad (\text{S.168})$$

where the Green-Kubo damping coefficient is (Eq. (S.58)),

$$\Gamma(k) = \int_0^\infty \operatorname{Re} K_k(\tau) \, d\tau = \frac{1}{2E_k} \int_0^\infty \operatorname{Re} C_F(\tau) \, d\tau = \frac{I_F}{2E_k}. \quad (\text{S.169})$$

Equation (S.169) gives the important relation

$$I_F = 2E_k \Gamma. \quad (\text{S.170})$$

Over one encounter of duration τ_{adv} , the mean energy change is

$$\langle \Delta E \rangle = -2\Gamma E_k \tau_{\text{adv}} + \mathcal{O}(\delta^3 / \sqrt{N_{\text{mode}}}) + \mathcal{O}(\delta^4), \quad (\text{S.171})$$

so that

$$\langle \xi \rangle = \frac{\langle \Delta E \rangle}{E_k} = -2\Gamma \tau_{\text{adv}}. \quad (\text{S.172})$$

Writing $\langle \xi \rangle = -\alpha \delta^2$,

$$\alpha = \frac{2\Gamma \tau_{\text{adv}}}{\delta^2}. \quad (\text{S.173})$$

Combining the two results and using (S.170) to eliminate I_F from (S.167),

$$\beta_\xi = \frac{2\tau_{\text{adv}}}{E_k \delta^2} \cdot 2E_k \Gamma = \frac{4\Gamma \tau_{\text{adv}}}{\delta^2}. \quad (\text{S.174})$$

Comparing with (S.173),

$$\boxed{\frac{\alpha}{\beta_\xi} = \frac{2\Gamma\tau_{\text{adv}}/\delta^2}{4\Gamma\tau_{\text{adv}}/\delta^2} = \frac{1}{2}}. \quad (\text{S.175})$$

This ratio is fixed entirely by FDR-II and the multiplicative coupling structure. It is independent of δ , ℓ_{corr} , the specific form of $C_F(\tau)$, and the wave energy E_k . The factor 1/2 can be traced as follows. FDR-II gives $\Gamma = I_F/(2E_k)$ (Eq. S.169), so the mean obeys $|\langle\xi\rangle| = 2\Gamma\tau_{\text{adv}}$. The power autocorrelation $C_{\dot{W}} = E_k \text{Re} C_F$ (Eq. S.165) carries a factor of E_k . Substituting $I_F = 2E_k\Gamma$ into the variance gives $\text{Var}(\xi) = 2\tau_{\text{adv}}I_F/E_k = 4\Gamma\tau_{\text{adv}}$. Hence $\alpha \propto 2\Gamma$ and $\beta_\xi \propto 4\Gamma$, giving $\alpha = \beta_\xi/2$: FDR-II links the mean and variance of the encounter-level fractional loss through the same force autocorrelation.

With the ξ -level statistics in hand, we pass to the log-energy increment $\Delta\varepsilon = \ln(1 + \xi)$ using the expansion (S.157). To leading order in δ ,

$$\begin{aligned} \langle\Delta\varepsilon\rangle &= \langle\xi\rangle - \frac{1}{2}\langle\xi^2\rangle + \mathcal{O}(\delta^3/\sqrt{N_{\text{mode}}}) + \mathcal{O}(\delta^4) \\ &= -\alpha\delta^2 - \frac{1}{2}\beta_\xi\delta^2 + \mathcal{O}(\delta^3/\sqrt{N_{\text{mode}}}) + \mathcal{O}(\delta^4), \end{aligned} \quad (\text{S.176})$$

where we used $\langle\xi^2\rangle = \text{Var}(\xi) + \langle\xi\rangle^2 = \beta_\xi\delta^2 + \mathcal{O}(\delta^4)$. The variance is

$$\text{Var}(\Delta\varepsilon) = \text{Var}(\xi) + \mathcal{O}(\delta^3/\sqrt{N_{\text{mode}}}) + \mathcal{O}(\delta^4) = \beta_\xi\delta^2 + \mathcal{O}(\delta^3/\sqrt{N_{\text{mode}}}) + \mathcal{O}(\delta^4). \quad (\text{S.177})$$

The remainder is small because ξ is the sum of contributions from $\mathcal{O}(N_{\text{mode}}) \gg 1$ weakly dependent turbulent Fourier components of the mode-projected force. Under A6 (finite memory) this sum is asymptotically Gaussian by the central limit theorem. In particular the third cumulant $\kappa_3(\xi) = \mathcal{O}(\delta^3/\sqrt{N_{\text{mode}}})$ is negligible and the leading cross-covariance $\text{Cov}(\xi, \xi^2)$ is parametrically suppressed, so non-Gaussian corrections are smaller than the retained $\mathcal{O}(\delta^2)$ terms. Writing $\langle\Delta\varepsilon\rangle = -A\delta^2$ and $\text{Var}(\Delta\varepsilon) = B\delta^2$, we identify,

$$A = \alpha + \frac{1}{2}\beta_\xi, \quad B = \beta_\xi. \quad (\text{S.178})$$

The coefficient A receives two contributions: α , the *physical drift* through the FDR-II linear-response mechanism, and $\frac{1}{2}\beta_\xi$, the *Itô correction*-the geometric effect of noise in multiplicative dynamics, analogous to the $-\frac{1}{2}\sigma^2$ correction in geometric Brownian motion. The ratio of the physical drift to the Itô correction is $\alpha/(\beta_\xi/2) = 1$. Half of the total log-energy decay comes from the noise-induced correction and half from the physical damping. The pathwise estimator (S.155) has mean

$$\langle\hat{\mu}(\omega)\rangle = \frac{A\delta^2}{\ell_{\text{corr}}} \quad (\text{S.179})$$

and variance

$$\text{Var}(\hat{\mu}) = \frac{B\delta^2}{L\ell_{\text{corr}}} + \mathcal{O}(\delta^4). \quad (\text{S.180})$$

Because the coarse-graining scale is chosen as $\ell_{\text{corr}} \sim \tau_c c_g$ (comparable to the force correlation length), the coefficients A and B each absorb an $\mathcal{O}(1)$ shape-dependent factor from the Green-Kubo integral replacement (see the coarse-graining remark above). These shape factors cancel identically in any ratio of B to A , so the predictions that follow ($c_0 = B/A$, the signal-to-noise ratio, and the negative-attenuation probability) are all independent of this approximation. Dividing (S.180) by (S.179) eliminates both δ and ℓ_{corr} ,

$$\text{Var}(\hat{\mu}) = \frac{B}{A} \frac{\langle\hat{\mu}(\omega)\rangle}{L} + \mathcal{O}(\delta^2). \quad (\text{S.181})$$

Defining $c_0 \equiv B/A$,

$$\boxed{\text{Var}(\hat{\mu}) = c_0 \frac{\langle\hat{\mu}(\omega)\rangle}{L}, \quad c_0 = \frac{B}{A} = \frac{\beta_\xi}{\alpha + \frac{1}{2}\beta_\xi} + \mathcal{O}(\delta^2)}. \quad (\text{S.182})$$

The same microscopic force autocorrelation that fixes the ensemble-mean attenuation $\mu_E(\omega)$ also determines the pathwise variance. No new degrees of freedom enter at the level of scatter. The cancellation of ℓ_{corr} between numerator and denominator in (S.181) is structurally significant. The ratio $\text{Var}(\hat{\mu})/\langle\hat{\mu}\rangle$ does not depend on the poorly constrained spatial correlation scale of the vorticity field. Both the mean and the variance per unit length scale as ℓ_{corr}^{-1} . Their ratio depends only on c_0 and the propagation distance L . Substituting $\alpha = \beta_\xi/2$ (Eq. S.175) into (S.178),

$$A = \frac{\beta_\xi}{2} + \frac{\beta_\xi}{2} = \beta_\xi, \quad B = \beta_\xi, \quad (\text{S.183})$$

so that

$$c_0 = \frac{B}{A} = \frac{\beta_\xi}{\beta_\xi} = 1 + \mathcal{O}(\delta^2). \quad (\text{S.184})$$

The logical chain is. The variance of ξ uses only bath statistics (A3, A5, A6) and gives $\text{Var}(\xi) = 2\tau_{\text{adv}}I_F/E_k$, the mean uses FDR-II and gives $|\langle\xi\rangle| = 2\Gamma\tau_{\text{adv}}$, FDR-II bridges the two via $I_F = 2E_k\Gamma$, fixing $\alpha = \beta_\xi/2$. The Itô correction from passing to $\Delta\varepsilon = \ln(1 + \xi)$ yields $A = \beta_\xi$, hence $c_0 = B/A = 1$. This result requires no specific parametric form for $C_F(\tau)$. It follows from FDR-II and the multiplicative coupling structure alone. Because F_k is bilinear in a_k (via $\mathbf{u}_\varphi \propto a_k$), the force autocorrelation factorises as $C_F(\tau) = 2E_k G_k(\tau)$ (Eq. (S.44)), where G_k depends only on the bath statistics. Hence $c_0 = 1$ is independent of wave amplitude.

The coefficients 2 (mean), 2 (variance), and 1 (their ratio) are analytic results at leading nontrivial order in the weak-coupling expansion $\delta = u'/c_g \ll 1$. They are not empirical fits, not large- L approximations, and not assumptions. They follow from FDR-II, the bilinear coupling structure, and the Ito correction, with corrections entering at $\mathcal{O}(\delta^2) \sim 10^{-6}$ - 10^{-4} . The fixed-design Monte Carlo simulations of Section D provide a numerical consistency check of this leading-order prediction.

The baseline $c_0 = 1$ applies to the finite-length log-endpoint estimator $\hat{\mu} = -[\ln E(L) - \ln E(0)]/L$. Satellite retrievals typically fit an OLS regression slope through M distance- H_s measurements along the track. For a Brownian log-energy process observed at M equally spaced points over length L , the intrinsic variance of the OLS slope is

$$\text{Var}(\hat{\mu}_{\text{OLS}} \mid \text{intrinsic}) = f(M) \frac{2\mu_E}{L}, \quad f(M) = \frac{6}{5} \frac{M^2 + 1}{M(M + 1)}, \quad (\text{S.185})$$

with $f(2) = f(3) = 1$ and $f(M) \rightarrow 6/5$ as $M \rightarrow \infty$. The inflation in the dense-sampling limit arises because intermediate points of a random walk add correlated noise without proportionate signal gain. The relevant M is the number of *effectively independent distance measurements* along the regression, not the total number of along-track H_s samples. In the Jiang et al. altimeter method [34, 61], each satellite overpass contributes one effective distance point (possibly averaged from several 7 km along-track samples), and a typical event is tracked over $M \sim 3$ -6 overpasses, giving $f(M) \approx 1.00$ -1.06. The Stopa et al. SAR analysis [19] requires at least 15 imagerettes from 5 satellite passes per track, giving effective $M \sim 5$ -15 and $f(M) \approx 1.04$ -1.13. In the present 241-track dataset, n_{points} ranges from 13 to 609 (median 117), but these are densely sampled along-track H_s values from ~ 3 -5 independent overpasses, so the effective M for the regression is of the same order as in the Jiang sample. At these low effective M values $f(M)$ lies between 1.00 and 1.13, corresponding to at most a 13% variance inflation over the endpoint baseline. This correction is an order of magnitude smaller than the width of the $c_{0,\text{MLE}}$ 95% confidence interval (0.60) and is absorbed into the empirical c_0 . The measurement-noise contribution to the regression variance scales as $\sigma_{\ln E}^2/S_{xx}$ and decreases with increasing M , remaining subdominant for $M \gtrsim 5$ (Section C).

B. Variance renormalisation from inter-encounter correlations

The baseline prediction $c_0 = 1$ (Eq. S.184) was obtained under the idealisation that the log-energy increments $\{\Delta\varepsilon_n\}$ over successive decorrelation segments are independent and identically distributed. Here we relax this assumption and quantify how weak dependence along the ray modifies the intrinsic estimator variance while leaving the ensemble-mean drift unchanged. It is essential to distinguish two objects.

(i) The *ensemble-mean* damping rate $\Gamma(k)$ (and the corresponding spatial attenuation rate $\mu_E = 2\Gamma/c_g$) is defined by the Green-Kubo relation

$$\Gamma(k) = \frac{1}{2E_k} \int_0^\infty \text{Re} \langle F_k(0) F_k^*(t) \rangle dt = \frac{S_F(0)}{4E_k} \geq 0, \quad (\text{S.186})$$

where $F_k(t)$ is the mode-projected stochastic vortex force and S_F is its power spectral density. Equation (S.186) depends only on the *integral* of the force autocorrelation (equivalently the zero-frequency spectral weight $S_F(0)$) and thus already incorporates the full temporal/spatial correlation structure of the turbulent bath. No discretisation into “encounters” is required to define Γ .

(ii) The *pathwise* satellite estimator $\hat{\mu}$ is a finite-length average of a fluctuating quantity and therefore has a nontrivial variance. The variance depends not only on the integral of an autocorrelation function but also on its *shape* through a long-run variance (integrated correlation length/time). This is where inter-encounter dependence enters. Let L denote the effective propagation distance and write the log-energy change as

$$\Delta\varepsilon(L) \equiv \ln E(L) - \ln E(0) = \int_0^L \dot{\varepsilon}(s) ds, \quad \hat{\mu} \equiv -\frac{\Delta\varepsilon(L)}{L}, \quad (\text{S.187})$$

where $\dot{\varepsilon}(s) = d \ln E / ds$ is the instantaneous log-energy decay rate along the ray. For a stationary, short-memory process $\dot{\varepsilon}$ with autocovariance $C_{\dot{\varepsilon}}(r) = \text{Cov}(\dot{\varepsilon}(s), \dot{\varepsilon}(s+r))$, the variance of $\hat{\mu}$ admits the exact representation

$$\text{Var}(\hat{\mu}) = \frac{1}{L^2} \int_0^L \int_0^L C_{\dot{\varepsilon}}(s-s') ds ds'. \quad (\text{S.188})$$

If L is large compared with the correlation length of $C_{\dot{\varepsilon}}$, the standard long-run variance reduction gives

$$\text{Var}(\hat{\mu}) \simeq \frac{1}{L} \int_{-\infty}^\infty C_{\dot{\varepsilon}}(r) dr. \quad (\text{S.189})$$

Equation (S.189) is the continuous analogue of the central-limit scaling for weakly dependent sequences. To connect with the encounter-level derivation of Eq. (S.184), partition the ray into segments of length ℓ_{corr} (the advective decorrelation length) and define

$$\Delta\varepsilon_n \equiv \int_{(n-1)\ell_{\text{corr}}}^{n\ell_{\text{corr}}} \dot{\varepsilon}(s) ds, \quad N \equiv L/\ell_{\text{corr}}. \quad (\text{S.190})$$

Then $\Delta\varepsilon(L) = \sum_{n=1}^N \Delta\varepsilon_n$ and

$$\text{Var}(\hat{\mu}) = \frac{1}{L^2} \text{Var}\left(\sum_{n=1}^N \Delta\varepsilon_n\right). \quad (\text{S.191})$$

Let

$$\rho_m \equiv \frac{\text{Cov}(\Delta\varepsilon_n, \Delta\varepsilon_{n+m})}{\text{Var}(\Delta\varepsilon_n)}, \quad m \geq 1, \quad (\text{S.192})$$

and assume short-memory mixing $\sum_{m \geq 1} |\rho_m| < \infty$ so that the long-run variance exists. A standard calculation yields

$$\text{Var}(\hat{\mu}) = \frac{\text{Var}(\Delta\varepsilon_n)}{L \ell_{\text{corr}}} \left(1 + 2 \sum_{m=1}^{\infty} \rho_m\right) \equiv \frac{\text{Var}(\Delta\varepsilon_n)}{L \ell_{\text{corr}}} \mathcal{R}, \quad (\text{S.193})$$

where

$$\mathcal{R} \equiv 1 + 2 \sum_{m=1}^{\infty} \rho_m \quad (\text{S.194})$$

is the discrete long-run variance renormalisation factor. In the near-independent-encounter limit, $\rho_m = 0$ for $m \geq 1$ and $\mathcal{R} = 1$. In the leading-order FDR-II/Ito framework (Section S6, Methods),

$$\langle \hat{\mu} \rangle = 2\mu_E, \quad \text{Var}(\hat{\mu}) = \frac{2\mu_E}{L} \quad (\text{near-independent encounters}), \quad (\text{S.195})$$

so that the intrinsic noise-to-signal coefficient is $c_0 = \sigma_{\hat{\mu}}^2 / (\langle \hat{\mu} \rangle / L) = 1$. With weak dependence the mean remains unchanged (linearity of expectation), but the variance is multiplied by \mathcal{R} ,

$$\text{Var}(\hat{\mu}) = \frac{2\mu_E}{L} \mathcal{R}, \quad \boxed{c_0 = \mathcal{R}}. \quad (\text{S.196})$$

Thus correlations renormalise the *second moment* only. The first-moment prediction μ_E is unaffected because it is fixed by the Green-Kubo coefficient Γ in Eq. (S.186).

A simple closure expresses \mathcal{R} in terms of an integral correlation length along the ray. Inter-encounter dependence of the increments $\Delta\varepsilon_n$ is inherited from the spatial organisation of the mode-projected SVF along the trajectory. Because $\dot{\varepsilon}$ is bilinear in the swell mode and the mode-projected force, its covariance generally involves fourth-order bath statistics. Under a Gaussian or quasi-Gaussian closure for the turbulent field (consistent with the leading-order Green-Kubo framework, Sections S2-S4), the increment correlations can be parametrised by a normalised spatial correlation function $R(r)$ of an appropriate projected bath field along the ray, giving the approximation $\rho_m \approx R(m\ell_{\text{corr}})$ for $m \geq 1$.

Using $R(-r) = R(r)$ and $\rho_0 \equiv 1$, we may rewrite $\mathcal{R} \simeq \sum_{m=-\infty}^{\infty} R(m\ell_{\text{corr}})$ and approximate the sum by a Riemann integral,

$$\mathcal{R} \simeq \frac{1}{\ell_{\text{corr}}} \int_{-\infty}^{\infty} R(r) dr \equiv \frac{\ell_{\text{int}}}{\ell_{\text{corr}}}, \quad (\text{S.197})$$

where

$$\ell_{\text{int}} \equiv \int_{-\infty}^{\infty} R(r) dr \quad (\text{S.198})$$

is the integral correlation length along the ray. Hence

$$\boxed{c_0 = \frac{\ell_{\text{int}}}{\ell_{\text{corr}}}}. \quad (\text{S.199})$$

This closure makes explicit that the remaining uncertainty in c_0 is controlled by an integrated correlation length, i.e. by the *shape* of the relevant correlation function, not by its value at zero lag. The sign and magnitude of the correction are controlled by the ratio $\mathcal{R} = \ell_{\text{int}}/\ell_{\text{corr}}$:

(i) $\mathcal{R} = 1$ ($c_0 = 1$): $R(r)$ decays rapidly and the chosen coarse-graining scale ℓ_{corr} matches the integral scale. Successive encounters are effectively independent.

(ii) $\mathcal{R} > 1$ ($c_0 > 1$): $R(r)$ has a slowly decaying positive tail, so $\ell_{\text{int}} > \ell_{\text{corr}}$. Physically, this occurs when the ray remains within a coherent large-scale structure for many consecutive segments, producing positively correlated increments. Large-scale intermittency of the dissipation rate can act similarly.

(iii) $\mathcal{R} < 1$ ($c_0 < 1$): $R(r)$ crosses zero and develops a negative lobe, reducing ℓ_{int} by cancellation. Along a one-dimensional transect through a vorticity-dominated field, rapid sign alternation can produce such negative lobes even when the velocity field itself remains positively correlated.

The integral scale ℓ_{int} is controlled primarily by the low-wavenumber rollover and by any sign changes of $R(r)$, rather than by inertial-range power laws alone. In particular, for the relevant

stationary along-ray process with one-dimensional spectrum $\Phi(q)$, ℓ_{int} is proportional to $\Phi(0^+)$ via the Wiener-Khinchin theorem. Hence the value of ℓ_{int} is set by the energy-injection range and by cancellation in $R(r)$, not by the inertial-subrange exponent. Our inferred negative-rate fractions are consistent with $c_0 = \mathcal{O}(1)$ and in fact suggest $c_0 \lesssim 1$, i.e. a modest variance reduction relative to the near-independent-encounter baseline.

All distribution-level predictions can be written in terms of c_0 : the signal-to-noise ratio $\mathcal{S} = \sqrt{\langle \hat{\mu} \rangle L / c_0}$, the negative-rate fraction $P(\hat{\mu} < 0) = \Phi(-\mathcal{S})$, and the deterministic emergence scale $L_{\text{det}} = c_0 / \langle \hat{\mu} \rangle$. The FDR-II baseline $c_0 = 1$ provides a reference value. The factor \mathcal{R} parametrises the remaining uncertainty associated with spatial organisation and weak dependence along the ray. Direct measurement of \mathcal{R} (equivalently ℓ_{int}) from wave-resolving DNS or high-resolution ocean simulations would close this last degree of freedom and yield a fully *a priori* prediction of the intrinsic estimator variance.

At the adopted observational lower bound $\sigma_{\text{meas}} = 0.63 \times 10^{-7} \text{ m}^{-1}$, the two-parameter likelihood analysis (Extended Data Fig. 7) yields $c_{0,\text{MLE}} = 0.78$ with a 95% confidence interval [0.56, 1.16], corresponding to

$$\mathcal{R} = c_0 \approx 0.78, \quad \mathcal{R} \in [0.56, 1.16] \text{ (95\% CI)}. \quad (\text{S.200})$$

This value is conditional on the assumed σ_{meas} . Because c_0 and σ_{meas} are partially degenerate in the likelihood—they trade off along a ridge that preserves the total predictive variance (Extended Data Fig. 8a in the main text)—a joint profile over both parameters at $\beta = 1$ yields a data-driven $\sigma_{\text{meas}} \approx 1.2 \times 10^{-7} \text{ m}^{-1}$ with c_0 near zero. The adopted $\sigma_{\text{meas}} = 0.63 \times 10^{-7} \text{ m}^{-1}$ is a lower bound reflecting observational errors alone. The excess in the data-driven estimate is attributable to residual ε_{eff} prediction error. The reported $c_{0,\text{MLE}} = 0.78$ should therefore be interpreted, within the adopted additive variance decomposition and the lower-bound choice of σ_{meas} , as a conditional upper bound on the true intrinsic variance coefficient, since it absorbs whatever non-intrinsic scatter is not captured by σ_{meas} . The first-moment prediction $\beta = 1$ is unaffected: it lies within the 95% CI regardless of how the variance budget is partitioned (Extended Data Fig. 8b,c).

If the true intrinsic c_0 does lie below 1, a physical mechanism is needed. Along-ray encounter correlations provide one. The renormalisation $c_0 = \mathcal{R}$ with $\mathcal{R} < 1$ (by construction $\mathcal{R} \geq 0$, since it is a long-run variance ratio) does not require anomalous variance suppression. It only implies that the along-ray correlation function is not a purely monotonic positive kernel, so that partial cancellation in the correlation integral reduces ℓ_{int} below ℓ_{corr} . This is plausible in the wave-driven upper ocean, where Langmuir turbulence can organise into counter-rotating vortical structures [10]. Depending on ray orientation, along-ray transects may then exhibit alternating-sign contributions and partial cancellation in the correlation integral. Large-eddy simulations show irregular cell patterns with finite spatial and temporal correlation scales rather than a single universal correlation shape [62]. Reviews of upper-ocean turbulence likewise emphasise that surface-wave effects drive substantial departures from the classical shear-only picture of boundary-layer mixing [22, 63].

A simple illustration is provided by an oscillatory correlation model, for example $R(r) \propto e^{-|r|/\ell_c} \cos(\kappa r)$, whose negative side-lobes reduce the correlation integral and can therefore produce $\mathcal{R} < 1$. At the conditional value $c_0 \approx 0.78$, only a modest oscillatory component is required; stronger cancellation would yield smaller \mathcal{R} , but the qualitative picture is unchanged.

C. Signal-to-noise ratio and deterministic emergence scale

The Green-Kubo theory determines the *ensemble-mean* energy decay rate μ_E through $d\langle E \rangle/dx = -2\mu_E \langle E \rangle$. Satellite altimeters, however, do not observe μ_E directly. They return a finite-length *log-endpoint* attenuation estimator

$$\hat{\mu} \equiv -\frac{1}{L} \ln \frac{E(L)}{E(0)}, \quad (\text{S.201})$$

whose mean differs from μ_E by the leading-order Itô correction. In the weak-coupling Markov limit (Section A),

$$\langle \hat{\mu} \rangle = 2\mu_E, \quad \text{Var}(\hat{\mu}) = \frac{2\mu_E}{L} c_0 \quad (c_0 = 1 \text{ for near-independent encounters}), \quad (\text{S.202})$$

so that the *detectability* of single-track decay is naturally quantified at the estimator level by the signal-to-noise ratio

$$\mathcal{S} \equiv \frac{\langle \hat{\mu} \rangle}{\sqrt{\text{Var}(\hat{\mu})}} = \sqrt{\frac{\langle \hat{\mu} \rangle L}{c_0}} = \frac{2\mu_E}{\sqrt{2\mu_E/L}} = \sqrt{2\mu_E L}. \quad (\text{S.203})$$

The appearance of $2\mu_E$ is therefore not a redefinition of the physical damping rate. It reflects the mapping from the underlying energy-space drift μ_E to the observed log-endpoint estimator $\hat{\mu}$ under multiplicative noise.

Setting $\mathcal{S} = 1$ defines the *deterministic emergence scale* L_{det} at which the cumulative regression signal becomes comparable to the cumulative intrinsic scatter,

$$L_{\text{det}} = \frac{c_0}{\langle \hat{\mu} \rangle} = \frac{c_0}{2\mu_E} \xrightarrow{c_0=1} \frac{1}{2\mu_E}. \quad (\text{S.204})$$

Thus L_{det} is an estimator-level detectability threshold. It should not be conflated with the ensemble-mean energy e -folding distance μ_E^{-1} . For $c_0 = 1$, L_{det} is half the energy e -folding distance because $\hat{\mu}$ is defined in log-energy and inherits the Itô drift. From the encounter-level scalings of Section I, $|\bar{\epsilon}| \sim E\delta^2$ and $\sigma \sim E\delta$, so $\mathcal{S} = 1$ requires $N^* = c_0\delta^{-2}$ encounters and hence $L_{\text{det}} = c_0 \ell_{\text{corr}} \delta^{-2}$. Using $\langle \hat{\mu} \rangle \sim \delta^2/\ell_{\text{corr}}$ (Eq. S.179) recovers identically

$$L_{\text{det}} = \frac{c_0 \ell_{\text{corr}}}{\delta^2} = \frac{c_0}{\langle \hat{\mu} \rangle}. \quad (\text{S.205})$$

For deep-water swell of period $T = 15$ s: $k \approx 0.018$ rad m $^{-1}$, $\ell_{\text{corr}} \sim 1/k \approx 60$ m. A trans-oceanic ray of length $L \sim 10^4$ km traverses

$$N \approx \frac{10^7 \text{ m}}{60 \text{ m}} \approx 1.7 \times 10^5 \quad (\text{S.206})$$

near-independent encounters. Inserting $\bar{\mu}_{\text{obs}} = 0.8 \times 10^{-7}$ m $^{-1}$ (corresponding to $\mu_E \approx 0.40 \times 10^{-7}$ m $^{-1}$) and $c_0 = 1$,

$$L_{\text{det}} = \frac{c_0}{\bar{\mu}_{\text{obs}}} \sim \frac{1}{0.8 \times 10^{-7}} \approx 1.25 \times 10^7 \text{ m} = 12,500 \text{ km}, \quad (\text{S.207})$$

and the signal-to-noise ratio for a 10 000 km path is

$$\mathcal{S} = \sqrt{\frac{\bar{\mu}_{\text{obs}} L}{c_0}} \approx \sqrt{\frac{0.8 \times 10^{-7} \times 10^7}{1}} \approx 0.89. \quad (\text{S.208})$$

This places typical trans-oceanic swell in the marginal-detection regime ($\mathcal{S} \lesssim 1$). The predicted negative-estimate fraction is

$$P(\hat{\mu}_i < 0) = \Phi(-\mathcal{S}) \approx \Phi(-0.89) \approx 19\%, \quad (\text{S.209})$$

consistent with the observed ranges of 24% [34] and 13% [19]. Because the scaling law links μ_E to independently measurable environmental quantities, the SNR can be written explicitly as

$$\mathcal{S}(\varepsilon_{\text{eff}}, \omega, L) = \sqrt{2C_{\text{tot}} \varepsilon_{\text{eff}}^{2/3} g^{-7/3} \omega^{8/3} L}, \quad (\text{S.210})$$

making transparent three routes to higher detectability, stronger turbulence, shorter-period swell, and longer paths, each explored in Extended Data Fig. 5. Note that \mathcal{S} here is the intrinsic SNR under spatially uniform ε_{eff} . Environmental variability along individual tracks inflates the effective variance, so the realised $\mathcal{S}_{\text{obs}} \leq \mathcal{S}$ and $P_{\text{obs}}(\hat{\mu} < 0) \geq \Phi(-\mathcal{S})$. Over the far-field wind range $u_{10} \approx 3\text{-}8 \text{ m s}^{-1}$ ($\varepsilon_{\text{eff}} \sim 10^{-8}\text{-}10^{-6} \text{ m}^2 \text{ s}^{-3}$), the 15 s swell SNR rises from $\mathcal{S} \approx 0.4$ to ≈ 1.2 and the intrinsic negative-estimate fraction decreases from $\sim 34\%$ to $\sim 11\%$. Both the Jiang and Stopa datasets fall on or below the theoretical curves, consistent with additional scatter from along-path environmental variability. At fixed turbulence and path length, the $\omega^{8/3}$ dependence gives $\mathcal{S} \propto \omega^{4/3}$, so 12 s swell has roughly double the SNR of 18 s swell. The small parameter $\delta = u'/c_g$ spans $10^{-3}\text{-}10^{-2}$ across the swell band (Extended Data Fig. 5c). The $\mathcal{S} \sim \mathcal{O}(1)$ regime is therefore not an artefact of any particular dataset but a robust feature of the parameter space occupied by remote oceanic swell. The full four-panel SNR analysis is presented in Extended Data Fig. 5.

D. Variance decomposition and error budget

Taking the logarithm of the scaling law, $\ln \mu_E = \ln C_{\text{tot}} + \frac{2}{3} \ln \varepsilon_{\text{eff}} - \frac{7}{3} \ln g + \frac{8}{3} \ln \omega$, gives logarithmic response coefficients $+2/3$ for ε_{eff} , $+8/3$ for ω , and $+1$ for C_{tot} . The ordering is fortunate. Swell frequency, the best-measured quantity, enters with the largest exponent, while ε_{eff} , uncertain by factors of 2-3, enters with the weakest. In addition to these three parametric uncertainties, two further sources enter. The significant wave height H_s , which controls the roughness depth $z_0 = c_b H_{s,w}$ in the wall-law profile (S.144) and thereby affects ε_{eff} through $E_1(2kz_0)$. The ray-path geometry, whose uncertainty arises from great-circle deviations due to refraction and current advection. Because $\mu_E \propto \varepsilon_{\text{eff}}^{2/3}$, the H_s uncertainty propagates with the same response coefficient $2/3$ as ε_{eff} itself, while σ_{ray} enters additively in log-space as a path-length error. Assuming independent, log-normally distributed errors, the environmental prediction uncertainty propagates as

$$\sigma_{\ln \mu, \text{env}}^2 = \left(\frac{2}{3}\right)^2 \sigma_{\ln \varepsilon}^2 + \sigma_{\ln C}^2 + \left(\frac{2}{3}\right)^2 \sigma_{\ln H_s}^2 + \left(\frac{8}{3}\right)^2 \sigma_{\ln \omega}^2 + \sigma_{\text{ray}}^2, \quad (\text{S.211})$$

giving $\sigma_{\ln \mu, \text{env}} \approx 0.57$, corresponding to a factor-of- $e^{0.57} \approx 1.8$ uncertainty in μ_E (and equivalently in $\langle \hat{\mu} \rangle = 2\mu_E$, since the factor of 2 holds at leading order),

$$\sigma_{\text{env}}^{(\mu)} \approx \sqrt{\exp(\sigma_{\ln \mu, \text{env}}^2) - 1} \bar{\mu}_{\text{obs}} \approx 0.62 \bar{\mu}_{\text{obs}}. \quad (\text{S.212})$$

Here $\bar{\mu}_{\text{obs}}$ denotes the observed ensemble-mean estimator value $\langle \hat{\mu} \rangle_{\text{obs}}$. This environmental error budget moves $\langle \hat{\mu} \rangle$ along the positive half-axis but cannot change its sign. The non-negativity theorem guarantees $\mu_E \geq 0$. The total variance of the single-path estimator $\hat{\mu}$ decomposes into three independent contributions,

$$\sigma_{\hat{\mu}}^2 = \underbrace{\sigma_{\text{int}}^2}_{\text{intrinsic}} + \underbrace{[\sigma_{\text{env}}^{(\mu)}]^2}_{\text{environmental}} + \underbrace{\sigma_{\text{obs}}^2}_{\text{observational}}. \quad (\text{S.213})$$

For a representative trans-oceanic swell track with $\bar{\mu}_{\text{obs}} = 0.8 \times 10^{-7} \text{ m}^{-1}$ (corresponding to $\mu_E = \bar{\mu}_{\text{obs}}/2 \approx 0.40 \times 10^{-7} \text{ m}^{-1}$), $L = 10^7 \text{ m}$ and $c_0 = 1$: $\sigma_{\text{int}} \approx \sqrt{2\mu_E/L} = \sqrt{c_0 \bar{\mu}_{\text{obs}}/L} \approx 0.89 \times 10^{-7} \text{ m}^{-1}$ (from Eq. (S.195)), $\sigma_{\text{env}}^{(\mu)} \approx 0.50 \times 10^{-7} \text{ m}^{-1}$ (from Eq. (S.212)), $\sigma_{\text{obs}} \approx 0.63 \times 10^{-7} \text{ m}^{-1}$ (root sum of squares of the four altimetric error sources identified in the altimetric error analysis [34], see Section C for the breakdown). In units of 10^{-7} m^{-1} ,

$$\sigma_{\text{int}} \approx 0.89, \quad \sigma_{\text{env}}^{(\mu)} \approx 0.50, \quad \sigma_{\text{obs}} \approx 0.63, \quad (\text{S.214})$$

giving variance fractions of approximately 55%, 17%, and 28% respectively (Extended Data Fig. 6a). The predicted total scatter $\sigma_{\text{total}} = \sqrt{0.89^2 + 0.50^2 + 0.63^2} \approx 1.3 \times 10^{-7} \text{ m}^{-1}$ is within

$\sim 9\%$ of the reported $1.2 \times 10^{-7} \text{ m}^{-1}$ [34], well inside the rounding uncertainty of the component estimates. The three variance components are estimated from independent information. Intrinsic from the Green-Kubo kernel, environmental from reanalysis uncertainties, and observational from the altimeter error analysis. Ensemble-averaging over M independent events reduces the intrinsic and observational contributions as $1/\sqrt{M}$, while the environmental bias remains fixed,

$$\sigma_{\hat{\mu}}^2 \approx \frac{\sigma_{\text{int}}^2 + \sigma_{\text{obs}}^2}{M} + [\sigma_{\text{env}}^{(\mu)}]^2. \quad (\text{S.215})$$

The crossover scale

$$M_{\times} \equiv \frac{\sigma_{\text{int}}^2 + \sigma_{\text{obs}}^2}{[\sigma_{\text{env}}^{(\mu)}]^2} \approx \frac{0.89^2 + 0.63^2}{0.50^2} \approx 5 \quad (\text{S.216})$$

separates the random-scatter-limited regime ($M < M_{\times}$) from the environment-limited regime ($M > M_{\times}$) (Extended Data Fig. 6b). The altimeter dataset [34] ($M = 202$) is firmly environment-limited. The random contribution to the ensemble-mean uncertainty is only $\approx 1/(\mathcal{S}\sqrt{M}) \sim 8\%$. The full four-panel variance anatomy is presented in Extended Data Fig. 7.

E. Negative attenuation rates and discriminating tests

The three sources of scatter in Eq. (S.213) contribute to the probability of observing $\hat{\mu} < 0$ through physically distinct mechanisms. Environmental variability does not challenge the theorem-level non-negativity of the local physical rate μ_E . The Green-Kubo coefficient is $\Gamma \geq 0$ for any stationary bath. However, because different tracks sample different ε_{eff} environments, the environmental term does contribute to the spread of the finite-length estimator $\hat{\mu}$ across the ensemble of tracks. In the variance decomposition (S.213) it enters as a between-track contribution to the positive part of the distribution. It does not by itself generate a negative tail for any individual track whose true $\mu_E > 0$, but it broadens the population from which the intrinsic and observational channels can push individual estimates below zero. Observational methodology noise alone, with $\sigma_{\text{obs}} \approx 0.63 \times 10^{-7}$, would give $P_{\text{neg}}^{(\text{obs})} = \Phi(-\bar{\mu}_{\text{obs}}/\sigma_{\text{obs}}) \approx 10\%$. Combining intrinsic and observational contributions *conditioned on a representative track mean* $\bar{\mu}_{\text{obs}}$ (environmental variability shifts the mean from track to track but does not itself generate negative estimates for tracks with $\mu_E > 0$),

$$P_{\text{neg}}^{(\text{cond})} \approx \Phi\left(\frac{-\bar{\mu}_{\text{obs}}}{\sqrt{\sigma_{\text{int}}^2 + \sigma_{\text{obs}}^2}}\right) \approx \Phi(-0.73) \approx 23\%, \quad (\text{S.217})$$

consistent with the observed 24%. The intrinsic SNR depends on frequency through $\mu_E(\omega) \propto \omega^{8/3}$,

$$\mathcal{S}_{\text{int}}(\omega) \propto \omega^{4/3} \sqrt{L}. \quad (\text{S.218})$$

At fixed L , low-frequency swell has smaller \mathcal{S} and a larger intrinsic negative fraction than high-frequency swell. Taking $\bar{\mu}_{\text{obs}} = 0.8 \times 10^{-7} \text{ m}^{-1}$ at $T = 15$ s with $\mathcal{S}_{\text{int}} \approx 0.89$ as a reference, $\mathcal{S}_{\text{int}}(T) \propto T^{-4/3}$ gives $\mathcal{S}_{\text{int}} \approx 1.04$ at $T = 12$ s and ≈ 0.57 at $T = 19$ s, corresponding to intrinsic negative fractions

$$P_{\text{neg}}^{(\text{int})}(T) = \Phi(-\mathcal{S}_{\text{int}}(T)) \sim 15\% \text{ at } T = 12 \text{ s}, \quad \sim 29\% \text{ at } T = 19 \text{ s}. \quad (\text{S.219})$$

Including observational noise, the total negative fraction rises from $\sim 17\%$ at $T = 12$ s to $\sim 33\%$ at $T = 19$ s—roughly a factor-of-two increase across the swell band. By contrast, the observational methodology noise has no strong frequency dependence, so $P_{\text{neg}}^{(\text{obs})}(T)$ would be nearly flat. The discriminating test is therefore: *Bin the swell tracks by period and compute $P_{\text{neg}}(T)$ in each bin. A steep increase toward long periods ($P_{\text{neg}} \propto \Phi(-\omega^{4/3}\sqrt{L})$) confirms the intrinsic encounter mechanism. A nearly frequency-independent P_{neg} is consistent with observational noise alone.*

A complementary test bins by propagation distance L and checks whether $P_{\text{neg}}(L)$ decreases with L , as predicted by $\mathcal{S} \propto \sqrt{L}$ for the intrinsic component. These tests form a natural hierarchy ranked by discriminating power. The 8/3 frequency exponent is the most robust, assembled entirely from kinematics and turbulence scaling and insensitive to the environmental error budget. Satellite data yield $b = 3.07$ with 95% CI [2.11, 4.04] [34], and the theoretical 8/3 ≈ 2.67 lies within this interval. The frequency-resolved negative-rate function At fixed ε_{eff} , path length and prefactor normalisation, the period dependence of $P_{\text{neg}}(T)$ is controlled by the $\omega^{8/3}$ scaling through $\mathcal{S} \propto \omega^{4/3}$. The absolute level of P_{neg} still depends on $C_{\text{tot}}\varepsilon_{\text{eff}}^{2/3}$ through the overall signal-to-noise ratio. This period trend discriminates against both observational noise (flat in T) and environmental uncertainty (non-negative). The absolute magnitude of $\bar{\mu}_{\text{obs}}$ is the least discriminating test. It depends on the full error budget. Agreement to within a factor of ~ 2 is consistent with that budget but has limited discriminating power. The analysis reveals a three-tier spatial structure,

$$\underbrace{\ell_{\text{corr}} \sim 60 \text{ m}}_{\text{encounter scale}} \ll \underbrace{L_{\text{det}} \sim 1.25 \times 10^4 \text{ km}}_{\text{emergence / regression } e\text{-folding}} \sim \underbrace{L_{\text{ocean}} \sim 10^4 \text{ km}}_{\text{trans-basin path}}. \quad (\text{S.220})$$

The encounter scale and the emergence scale are separated by $1/\delta^2 \sim 10^5$, reflecting the enormous number of nearly symmetric interactions needed to produce an $O(1)$ fractional energy loss. That $L_{\text{det}} \sim L_{\text{ocean}}$ is not a coincidence. The turbulence dissipation rates prevailing in the remote mixed layer yield attenuation rates whose regression e -folding distances match the scale of Earth's ocean basins. Single-ray observations therefore occupy a regime of marginal detectability- $\mu_E(\omega)$ is strictly positive and well-defined, but $\hat{\mu}$ carries relative uncertainties of order unity and negative estimates occur with probability $\Phi(-\mathcal{S}) \sim 15\text{-}25\%$. Ensemble averages converge rapidly. For $M \sim 200$ events the sample-mean uncertainty is $(\mathcal{S}\sqrt{M})^{-1} \sim 8\%$.

S7. Comparison with satellite observations

The scaling law and the CLT bridge (Eq. S.151) imply order-unity single-track scatter for basin-scale remote-swell paths, so a non-negligible fraction of finite-length regression estimates should satisfy $\hat{\mu} < 0$. This section places that prediction in the context of two published satellite data sets. The 202-event altimeter-WW3 analysis [34] and the 10-year Envisat SAR analysis [19]. The former is best viewed as a historical benchmark and methodological precursor of the 241-track sample used in the main text, whereas the latter provides a distinct SAR-based product. Because the two studies report different subsets of $\{\bar{\mu}_{\text{obs}}, \sigma_{\hat{\mu}}, P_{\text{neg}}\}$, the comparisons below combine direct tests with consistency checks rather than a single uniform likelihood analysis. Section C then uses the Monte Carlo error analysis of the tracking pipeline to quantify the non-intrinsic variance floor.

Signal-to-noise ratios used in this section. Different observational products report different subsets of $\{\bar{\mu}_{\text{obs}}, \sigma_{\hat{\mu}}, P_{\text{neg}}\}$. To prevent ambiguity we explicitly distinguish three SNRs:

1. **Intrinsic SNR** (physics-only, encounter noise),

$$\mathcal{S}_{\text{int}} \equiv \frac{\langle \hat{\mu} \rangle}{\sigma_{\text{int}}} = \sqrt{\frac{\langle \hat{\mu} \rangle L_{\text{eff}}}{c_0}} \approx \sqrt{\frac{\bar{\mu}_{\text{obs}} L_{\text{eff}}}{c_0}}, \quad (\text{S.221})$$

using $\sigma_{\text{int}}^2 = c_0 \langle \hat{\mu} \rangle / L_{\text{eff}}$ (Eq. S.213) with $c_0 = 1$ (Eq. S.73).

2. **Total SNR** (dataset-implied when both sample mean and sample SD are reported),

$$\mathcal{S}_{\text{tot}} \equiv \frac{\bar{\mu}_{\text{obs}}}{\sigma_{\hat{\mu}}}, \quad (\text{S.222})$$

which folds encounter noise together with observational methodology noise and environmental variability.

3. **Effective SNR** (when only the negative fraction is available),

$$\mathcal{S}_{\text{eff}} \equiv -\Phi^{-1}(P_{\text{neg,obs}}) \quad \text{so that} \quad P_{\text{neg,obs}} = \Phi(-\mathcal{S}_{\text{eff}}). \quad (\text{S.223})$$

This is a *back-calculated summary statistic* and therefore supports only a *consistency check* on plausible SNR levels, not an independent test of the functional form $P(\hat{\mu} < 0) = \Phi(-\mathcal{S})$.

A. Altimeter tracking dataset

A historical benchmark is the far-field altimeter-WW3 analysis [34], which contains 202 swell events with periods 12-18s and wavelengths 250-500m. The reported ensemble statistics are $\bar{\mu}_{\text{obs}} = 0.8 \times 10^{-7} \text{ m}^{-1}$, $\sigma_{\hat{\mu}} = 1.2 \times 10^{-7} \text{ m}^{-1}$, and 49/202 negative estimates (24.3%). The same study also notes that the dissipation-rate histogram is approximately normal-like and that most negative values are not statistically significant once their estimated methodology errors are taken into account.

To set the physical scale, take a representative basin-scale path with $L_{\text{eff}} = 10^7 \text{ m}$. This is not a fit to the Jiang sample, only a scale-setting estimate for a trans-oceanic path. Using $\bar{\mu}_{\text{obs}} = 0.8 \times 10^{-7} \text{ m}^{-1}$ and $c_0 = 1$ gives

$$\mathcal{S}_{\text{int}} = \sqrt{\frac{\bar{\mu}_{\text{obs}} L_{\text{eff}}}{c_0}} = \sqrt{\frac{0.8 \times 10^{-7} \times 10^7}{1}} \approx 0.89, \quad (\text{S.224})$$

placing typical basin-scale swell tracks in the marginal-detection regime ($\mathcal{S}_{\text{int}} \lesssim 1$). The intrinsic model therefore predicts

$$P_{\text{neg}}^{(\text{int})} = \Phi(-\mathcal{S}_{\text{int}}) = \Phi(-0.89) \approx 19\%, \quad (\text{S.225})$$

close to the observed 24.3% and slightly below, as expected when non-intrinsic variance contributions are included (Section C).

From the reported sample mean and sample standard deviation,

$$\mathcal{S}_{\text{tot}} = \frac{\bar{\mu}_{\text{obs}}}{\sigma_{\hat{\mu}}} = \frac{0.8}{1.2} \approx 0.67. \quad (\text{S.226})$$

Under the Gaussian approximation suggested by the normal-like histogram reported in that study,

$$P(\hat{\mu} < 0) = \Phi(-\mathcal{S}_{\text{tot}}) = \Phi(-0.67) \approx 25\%, \quad (\text{S.227})$$

in close agreement with the observed 24.3%. The Jiang dataset therefore already exhibits the key qualitative signature of the theory. Broad, near-Gaussian single-track scatter with a substantial negative tail. The sharper path-length and frequency discriminating tests are carried out using the 241-track sample analysed in the main text and in Section E.

B. SAR tracking dataset

A distinct satellite product is the 10-year Envisat SAR wave-mode analysis [19], which reports 1050 swell tracks from 460 storm events. Of these, 910 fitted dissipation rates are positive and 140 are negative. The statement that 423 cases are “not statistically different from zero” refers to a subset of the same 1050 tracks, not to an additional set of fitted rates. After imposing a 95% confidence criterion, the retained subset contains 606 positive and 21 negative cases.

Because this product does not report $\bar{\mu}_{\text{obs}}$ and $\sigma_{\hat{\mu}}$ in a form directly comparable to the altimeter statistics, we characterise it via the effective SNR inferred from the negative fraction. For the full sample,

$$P_{\text{neg,obs}} = \frac{140}{1050} \approx 0.133 \quad \implies \quad \mathcal{S}_{\text{eff}} \approx 1.11. \quad (\text{S.228})$$

This is a back-calculated consistency check on plausible SNR levels (Eq. S.223), not an independent validation of $P(\hat{\mu} < 0) = \Phi(-\mathcal{S})$.

For the 95% significant subset,

$$P_{\text{neg,obs}} = \frac{21}{627} \approx 0.034 \implies \mathcal{S}_{\text{eff}} \approx 1.82, \quad (\text{S.229})$$

because $\Phi(-1.82) \approx 3.4\%$. The drop from 13.3% to 3.4% under stricter quality control is qualitatively consistent with preferential removal of low-SNR tracks. The SAR dataset therefore supports the same broad picture: order-unity pathwise scatter, a non-negligible negative tail before strict filtering, and a strong sensitivity of that tail to data-quality thresholds.

C. Variance budget and the Monte Carlo gap

The historical altimeter benchmark raises a specific question: can the broad single-track scatter be explained by deterministic methodology noise alone? The answer is no. The observational methodology noise $\sigma_{\text{obs}} \approx 0.63 \times 10^{-7} \text{ m}^{-1}$ is computed from the four independent altimetric error sources identified in the altimetric error analysis [34] (their Section 3): H_s measurement precision (≈ 0.1), swell-partition approximation (≈ 0.3), fitting-method sensitivity (≈ 0.2), and point-source model deviation (≈ 0.5), all in units of 10^{-7} m^{-1} . Added in quadrature, $\sigma_{\text{obs}} = \sqrt{0.1^2 + 0.3^2 + 0.2^2 + 0.5^2} \approx 0.63 \times 10^{-7} \text{ m}^{-1}$. An end-to-end Monte Carlo analysis of the tracking pipeline [61] provides an independent check on this noise floor. The observational term accounts for only

$$\frac{\sigma_{\text{obs}}^2}{\sigma_{\hat{\mu}}^2} = \left(\frac{0.63}{1.20}\right)^2 \approx 0.28 \quad (\text{S.230})$$

of the observed variance in the altimeter sample. A purely deterministic single-track picture therefore leaves roughly 72% of the variance unexplained.

In the present framework that missing variance is supplied by intrinsic wave-eddy encounter statistics. Using the leading-order FDR-II/Itô baseline $c_0 = 1$, together with $\bar{\mu}_{\text{obs}} = 0.8 \times 10^{-7} \text{ m}^{-1}$ and $L_{\text{eff}} = 10^7 \text{ m}$, gives

$$\sigma_{\text{int}} = \sqrt{\frac{c_0 \bar{\mu}_{\text{obs}}}{L_{\text{eff}}}} \approx 0.89 \times 10^{-7} \text{ m}^{-1}. \quad (\text{S.231})$$

Including the propagated environmental contribution $\sigma_{\text{env}}^{(\mu)} \approx 0.50 \times 10^{-7} \text{ m}^{-1}$ (Section D) then gives

$$\sigma_{\text{tot}} = \sqrt{\sigma_{\text{int}}^2 + \sigma_{\text{obs}}^2 + (\sigma_{\text{env}}^{(\mu)})^2} \approx 1.20 \times 10^{-7} \text{ m}^{-1}, \quad (\text{S.232})$$

matching the observed $1.20 \times 10^{-7} \text{ m}^{-1}$. The variance budget is therefore approximately closed without any additional fit to the single-track scatter: deterministic methodology noise alone is too small, whereas methodology noise, environmental variability, and the intrinsic SVF term naturally recover the observed scale.

This comparison should not be over-read as a claim that real-ocean tracks must satisfy the near-independent-encounter baseline $c_0 = 1$ exactly. In the theory, $c_0 = 1$ is the clean leading-order reference. Weak along-ray dependence renormalises only the second moment, not the first (Section B). This is consistent with what is seen in the 241-track main-text analysis. The first-moment scaling factor remains consistent with $\beta = 1$, while any effective renormalisation is absorbed into c_0 and its partial degeneracy with σ_{meas} .

Two findings of the pipeline Monte Carlo study [61] acquire a sharper interpretation in the present framework. First, the positive correlation sometimes found between fitted $\hat{\mu}$ and the initial wave-height estimate can arise algebraically because both quantities are inferred from the same exponential regression. It is therefore not, by itself, diagnostic of a distinct amplitude-dependent or air-side dissipation mechanism. Second, when $\mathcal{S} = \mathcal{O}(1)$, single-track

fitting cannot discriminate competing functional forms of swell attenuation. Functional-form inference must instead come from ensemble means and distribution-level tests.

The same variance decomposition also clarifies the averaging regime. The crossover between the random-scatter-limited regime and the environment-limited floor occurs at only $M_\times \sim 5$ tracks (Eq. S.216), so the 202-event Jiang benchmark is already deeply environment-limited. Adding more events reduces the sampling noise, but cannot eliminate the environmental floor set by path-to-path variability in ε_{eff} .

D. Fixed-design Monte Carlo validation of the inference layer

The variance budget shows that the theoretical noise model is consistent with the observed scatter. A separate question is whether the profile-likelihood inference procedure itself is well calibrated: if the true coefficients were exactly $(\beta, c_0) = (1, 1)$, would the pipeline recover them without systematic bias?

This question is distinct from the forward observational Monte Carlo performed by Jiang et al. [61]. There, a true attenuation rate was prescribed on an idealised swell track, retrieval errors were injected, and the resulting distribution of fitted $\hat{\mu}$ was examined. That analysis quantifies how measurement and sampling errors propagate into attenuation estimates. The present experiment addresses a different question: whether the statistical inference machinery—the heteroscedastic likelihood, the optimiser, and the profile confidence intervals—is internally calibrated under the assumed model family. It therefore tests the inference layer itself, not observational realism in the sense of Jiang et al. The two exercises are complementary, not redundant.

We therefore perform a fixed-design parameter-recovery test. The generative model is the CLT bridge (Eq. S.151) restricted to the pure SVF channel. Writing $\mu_{\text{svf},i}$ for the path-averaged observable-level SVF predictor of track i (equal to $2\mu_{E,i}$ under homogeneous along-ray conditions), the synthetic observations are

$$\hat{\mu}_i^{(r)} \sim \mathcal{N}(\beta^* \mu_{\text{svf},i}, c_0^* \beta^* \mu_{\text{svf},i} / L_i + \sigma_{\text{meas}}^2), \quad (\text{S.233})$$

with imposed truth $(\beta^*, c_0^*, \sigma_{\text{meas}}^*)$. Here β is the first-moment scaling factor defined in the main text ($\hat{\mu}_{\text{obs}} = \beta \mu_{\text{model}}$), not the local step-variance ratio β_ξ of Section A. c_0 is the variance-to-mean ratio ($c_0 = 1$ at the near-independent-encounter baseline, equivalent to $\mathcal{R} = 1$ in Eq. S.151), and σ_{meas} is the additive methodology noise floor. Under these identifications, Eq. (S.233) reduces to the CLT-bridge variance $2\mu_{E,i}\mathcal{R}/L_i + \sigma_{\text{meas}}^2$ when $\mu_{\text{svf},i} = 2\mu_{E,i}$, $c_0 = \mathcal{R}$, and $\beta = 1$. The near-independent-encounter baseline is therefore the special case $(\beta, \mathcal{R}) = (1, 1)$. The real 241-track design matrix $(L_i, \mu_{\text{svf},i})$ is held fixed throughout; only the observations are regenerated. For each synthetic dataset the negative log-likelihood

$$\text{NLL}(\beta, c_0, \sigma_{\text{meas}}) = \frac{1}{2} \sum_{i=1}^N \left[\ln \sigma_i^2 + \frac{(\hat{\mu}_i - \beta \mu_{\text{svf},i})^2}{\sigma_i^2} \right], \quad \sigma_i^2 = c_0 \beta \mu_{\text{svf},i} / L_i + \sigma_{\text{meas}}^2, \quad (\text{S.234})$$

is minimised over $(\beta, c_0, \sigma_{\text{meas}})$ by L-BFGS-B with a $3 \times 3 \times 3 = 27$ -point multi-start grid. Profile-likelihood 95% confidence intervals for β and c_0 are obtained by adaptive bisection. Starting from the MLE, the profiled NLL is stepped outward until $\Delta\text{NLL} > \frac{1}{2}\chi_{0.95}^2(1) \approx 1.92$; the crossing is then located to 10^{-4} precision by bisection. Joint rejection of the true parameter vector uses $\Delta\text{NLL}(\beta^*, c_0^*, \sigma_{\text{meas}}^*) > \frac{1}{2}\chi_{0.95}^2(3) \approx 3.91$.

The deterministic laminar viscous correction is excluded from both generator and likelihood because it does not participate in the heteroscedastic fluctuation law. The experiment therefore validates the stochastic SVF inference layer, not every deterministic sub-component. For each scenario, $R = 2000$ independent replications are performed. From the recovered triplets $(\hat{\beta}^{(r)}, \hat{c}_0^{(r)}, \hat{\sigma}_{\text{meas}}^{(r)})$ we compute the bias $(\hat{\theta} - \theta^*)$, standard deviation, 95% profile-likelihood coverage (the fraction of replicates whose CI contains the true value), and the joint false-rejection rate.

Three noise scenarios are considered: a baseline $\sigma_{\text{meas}}^* = 0.63 \times 10^{-7} \text{ m}^{-1}$ matching the quadrature estimate from altimetric error sources [34], a low-noise case (0.30×10^{-7}), and a high-noise case (1.00×10^{-7}). In all three, the imposed truth is $(\beta^*, c_0^*) = (1, 1)$. Table S2 summarises the results. In every scenario the bias is negligible: $|\text{bias}(\hat{\beta})| < 0.003$ and $|\text{bias}(\hat{c}_0)| < 0.02$. The 95% profile-likelihood coverage rates are 94.6–96.0% for β and 94.6–94.9% for c_0 , consistent with the nominal level. The joint false-rejection rate—the fraction of replicates in which the true parameter vector is rejected at the 95% level under a $\chi^2(3)$ threshold—is 3.8–5.4%, again consistent with the nominal 5%. The recovered $\hat{\beta}$ and \hat{c}_0 are negatively correlated ($\rho \approx -0.58$ to -0.75), reflecting the partial degeneracy between the mean-scaling and variance-scaling roles of β . This correlation is visible in Extended Data Fig. 4d but does not compromise identifiability: both marginal standard deviations remain moderate ($\text{SD}(\hat{\beta}) \approx 0.14$ – 0.17 , $\text{SD}(\hat{c}_0) \approx 0.21$ – 0.37).

We emphasise the scope of this validation. The recovery experiment shows that the inference machinery is unbiased and properly calibrated *conditional on* data drawn from the assumed model family. It does not, by itself, establish that real-ocean tracks obey that model. That external consistency must instead come from the independent evidence assembled in the main text: the frequency and environmental dependence of the ensemble-mean decay rate, the negative-rate fraction, and the residual structure (Figs. 4 and 5).

Table S2: Fixed-design Monte Carlo recovery ($R = 2000$, $(\beta^*, c_0^*) = (1, 1)$). Bias and standard deviation are computed over the R replications. Coverage is the fraction of replicates whose 95% profile-likelihood CI contains the true value. Joint rejection uses $\Delta\text{NLL} > \frac{1}{2}\chi_{0.95}^2(3)$.

Scenario	σ_{meas}^* ($\times 10^{-7} \text{ m}^{-1}$)	$\text{bias}(\hat{\beta})$	$\text{SD}(\hat{\beta})$	$\text{bias}(\hat{c}_0)$	$\text{SD}(\hat{c}_0)$	Cov. β (%)	Cov. c_0 (%)	Joint rej. (%)
Baseline	0.63	+0.003	0.15	+0.01	0.25	95.4	94.6	5.4
Low noise	0.30	−0.000	0.14	+0.01	0.21	94.6	94.9	3.8
High noise	1.00	+0.003	0.17	+0.02	0.37	96.0	94.9	4.4

E. Cross-dataset consistency

Table S3 collects the negative-rate fractions from three independent observational sources, with alternative SNR interpretations shown where relevant. For the two altimeter samples the associated SNR estimates follow the forward model of Sections A–C; for the SAR rows an effective SNR is inferred from the observed negative fraction for consistency mapping only (Eq. S.223). All three sources sit in the $\mathcal{S} = \mathcal{O}(1)$ regime, confirming that the broad single-track scatter and its substantial negative tail are not artefacts of a single retrieval algorithm or observation platform. The differences in aggregate P_{neg} across datasets (26%, 24%, 13%) reflect differences in period and path-length distributions, environmental sampling, and measurement-noise characteristics rather than any inconsistency in the underlying physics. The sharper quantitative tests—frequency and path-length dependence, profile likelihood for β —are carried by the 241-track sample analysed in the main text.

S8. Amplitude independence of the attenuation rate

The stochastic vortex-force theory predicts that, within the far-field, non-breaking regime governed by Assumptions A1–A5, the attenuation rate μ_E is independent of wave amplitude. Because the coupling is linear in amplitude (A4, $F_k \propto a_k$), the force autocorrelation factorises as $\langle F_k(0) F_k^*(t) \rangle = \langle |a_k|^2 \rangle G_k(t)$, where G_k depends only on the bath statistics. The wave energy scales as $E_k = \frac{1}{2} \langle |a_k|^2 \rangle$ (convention of Section S2). This factor cancels identically in the Green-Kubo expression $\mu_E \propto (2E_k)^{-1} \int_0^\infty \langle F_k(0) F_k^*(t) \rangle dt = \frac{1}{2} \int_0^\infty G_k(t) dt$, so μ_E depends only on the turbulence parameters (ε , τ_{corr}) and on the wavenumber k . The damping rate is a material

Table S3: Observed and model-consistent negative-rate fractions. For the altimeter rows the SNR is derived from the forward model; rows marked † report \mathcal{S}_{eff} inferred from $P_{\text{neg,obs}}$ (Eq. S.223), so the listed $P_{\text{neg}}^{\text{pred}}$ matches the observation by construction and is shown only for bookkeeping.

Dataset	N	SNR used	$P_{\text{neg}}^{\text{pred}}$	$P_{\text{neg}}^{\text{obs}}$
Altimeter (this work)	241	$\mathcal{S}_{\text{tot}} \approx 0.73$	23%	26%
Altimeter (historical benchmark; intrinsic)	202	$\mathcal{S}_{\text{int}} \approx 0.89$	19%	24.3%
Altimeter (historical benchmark; total)	202	$\mathcal{S}_{\text{tot}} \approx 0.67$	25%	24.3%
SAR (full sample)†	1050	$\mathcal{S}_{\text{eff}} \approx 1.11$	13.3%	13.3%
SAR (95% significant subset)†	627	$\mathcal{S}_{\text{eff}} \approx 1.82$	3.4%	3.4%

property of the turbulent bath at fixed k , analogous to how the Stokes drag on a Brownian particle depends on solvent viscosity and particle geometry but not on the particle’s kinetic energy.

Two assumptions are the structural ingredients for this cancellation. A4 (linear coupling, $F_k \propto a_k$) ensures that $|a_k|^2$ can be factored out of the force autocorrelation. A5 (bath statistics independent of swell energy) is the weak-probe condition quantified in Section S2. A2 (slow amplitude variation) justifies treating a_k as quasi-constant over the Green-Kubo correlation window $\tau \lesssim \tau_c$, so that $a_k(0) a_k^*(\tau) \approx |a_k|^2$. For trans-oceanic swell all three hold with large margins. Nonlinear corrections enter at $\mathcal{O}(\delta^2) \sim 10^{-6}$ - 10^{-4} (with $\delta = u'/c_g \sim 10^{-3}$ - 10^{-2}), and the rate of energy extraction from the swell per unit surface area ($\sim 5 \times 10^{-3} \text{ W m}^{-2}$ for $H_s \sim 2 \text{ m}$) perturbs the mixed-layer NESS by only $\sim 5 \times 10^{-3}$ - 5×10^{-2} of the wind power (~ 0.1 - 1 W m^{-2}) maintaining the bath. Throughout this section we implicitly invoke Assumption A3 (Section S2). This prediction stands in sharp contrast to the amplitude-dependent swell-dissipation parameterisation used in the empirical amplitude-dependent source-term family for WAVEWATCH III [64–66]. In the current standard implementation [65], the swell source term is

$$S_{\text{swl}}(k, \theta) = -\frac{2}{3} b_1 \sigma \sqrt{B_n(k)} F(k, \theta), \quad b_1 = \frac{1}{2} B_1 H_s k_p, \quad (\text{S.235})$$

where $F(k, \theta) = N(k, \theta) \sigma$ is the energy spectrum, N the action density, $B_n(k)$ the spectral saturation ($\propto N \sigma k^3$), and B_1 a tunable coefficient. Under a uniform amplitude scaling of the swell spectrum at fixed spectral shape, the three amplitude-dependent factors combine as $b_1 \propto H_s \propto \sqrt{N}$, $\sqrt{B_n} \propto \sqrt{N}$, $F \propto N$, giving $S_{\text{swl}} \propto N^2$. The implied attenuation rate is therefore quadratic in amplitude,

$$\mu_{\text{emp}}(k, \theta) \equiv -\frac{S_{\text{swl}}(k, \theta)}{F(k, \theta)} \propto N \propto a^2 \propto H_s^2. \quad (\text{S.236})$$

Over the range of initial wave heights in the altimeter dataset ($H_{s,0} = 1.3$ - 4.9 m) [34], this predicts a factor of $(4.9/1.3)^2 \approx 14$ variation in μ_E -readily detectable in 241 distinct swell tracks. Table S4 summarises the contrasting predictions.

Table S4: Predicted amplitude dependence: SVF theory versus the empirical parameterisation.

Property	SVF (this work)	Empirical
μ_E dependence on H_s	$\mu_E \propto H_s^0$	$\mu_E \propto H_s^2$
Predicted variation over $H_s = 1.3$ - 4.9 m	$\times 1$	$\times 14$
Observed H_s - $\hat{\mu}$ correlation (241 tracks)	$r = 0.00$	-
Frequency exponent	$\omega^{8/3}$	depends on B_n

We test the prediction using satellite tracks retained under the selection criteria ($250 \leq \lambda \leq 500 \text{ m}$) [34]. A scatter plot of $\hat{\mu}$ versus $H_{s,0}$ for all 241 tracks yields $r = 0.00$ ($p = 0.98$),

consistent with no association (Extended Data Fig. 3a). To control for the dominant frequency dependence $\mu_E \propto \omega^{8/3}$, we partition the data into three period bins (12.5-14 s, $n = 71$; 14-15.5 s, $n = 90$; 15.5-18 s, $n = 80$). Within each bin the correlation is statistically insignificant at the 1% level ($|r| \leq 0.24$), with no consistent sign across bins. The largest $R^2 \lesssim 0.06$ implies at most $\sim 6\%$ of the within-bin variability could be attributed to amplitude. This is far below what would be required for a robust quadratic-amplitude trend to emerge over the observed factor-of-3.8 amplitude range (Eq. S.213, Extended Data Fig. 3b). A partial-correlation analysis in which the $\omega^{8/3}$ -dependence is first regressed out confirms the null result. $r_{\text{partial}} = 0.07$ ($p = 0.27$) (Extended Data Fig. 3c). Quartile-binned means within each period group show no systematic trend (Extended Data Fig. 3d). The non-detection is particularly significant because the dynamic range of $H_{s,0}$ (factor ~ 3.8) would produce a factor-of-14 signal under the empirical parameterisation, well above the observational noise floor characterised in Section S7 (Eq. S.213). The full four-panel analysis is presented in Extended Data Fig. 3.

The amplitude independence also clarifies the interpretation of pathwise scatter (Section S6). Because μ_E does not depend on a , the pathwise fluctuation in $\hat{\mu}$ is driven entirely by turbulent encounters along the propagation path and environmental variability, not by variations in wave amplitude. The variance budget of Section D (intrinsic, environmental, and observational components) is therefore cleanly separated from any amplitude effect, and the frequency-resolved discriminating test (Section E) is a pure test of the dissipation mechanism rather than a confounded measure of amplitude-dependent processes.

S9. Domain of validity: why remote swell isolates the universal dissipation law

The theorem-level non-negativity result and the closed-form remote-swell law have distinct domains of validity. The Green-Kubo sign theorem for the mode-level damping coefficient, $\Gamma(k) \geq 0$ (Theorem 1), requires Assumptions A1 (wave subspace), A3(i, iii) (stationarity, zero ensemble mean), A5(i) (local stationarity of the bath measure) and A6 (finite memory). In contrast, the factorised closed-form law $\mu \propto \varepsilon_{\text{eff}}^{2/3} \omega^{8/3}$ and the amplitude-independence of the attenuation rate require the additional remote-swell conditions used in Sections S2-S4. These are quasi-frozen wave amplitude over the correlation window (A2), phase decoupling between the swell and the bath (A3(ii)), linear truncation in wave amplitude (A4), and approximate factorisation of the reference measure (A5(ii)). Remote swell is precisely the regime in which these extra conditions are best satisfied. Wave breaking is rare, local wind input and nonlinear wave-wave transfer are comparatively weak, and the wave phase is set by distant forcing rather than by the local mixed-layer dynamics.

The stochastic vortex-force (SVF) coupling is therefore not unique to swell-it operates whenever waves propagate through turbulence. What is special about remote swell is not the existence of the coupling, but the fact that competing processes are weak enough for the SVF law to be isolated observationally. In actively forced wind seas, by contrast, local forcing correlates the wave field with the turbulent bath, the decoupling conditions deteriorate, and wave breaking typically dominates the wave-energy budget by orders of magnitude over the remote-swell SVF channel [67, 68].

The dominant energy sink for steep wind waves is breaking [66, 67]. For waves approaching a representative deep-water breaking threshold of order $ak \sim 0.3$ [66, 69], breaking attenuation can reach $\mu_{\text{brk}} \sim 10^{-5}$ - 10^{-4} m^{-1} , corresponding to e -folding distances of only 10-100 km. For gentle far-field swell with $ak \sim 0.01$ - 0.05 , steepness is far below onset and breaking is strongly suppressed. Under typical open-ocean remote-swell conditions it is therefore negligible to leading order within the present framework.

The phase-averaged Craik-Leibovich (CL) vortex force [6, 7] occupies a different status from the SVF. In the mode-level theory of Sections S1-S2, the CL term is conservative with respect to the resolved swell mode. It carries spectral weight at frequencies 0 and 2ω , not at the swell

frequency ω , and therefore does not enter the Green-Kubo friction coefficient derived from the projected stochastic force. It is nevertheless useful to estimate a separate quasi-steady, signed wave-mean-flow exchange associated with Stokes-shear production [35]. Under the standard quasi-steady assumption that the turbulent stresses are uncorrelated with the fast wave phase, the depth-integrated production scales as

$$\int_{-\infty}^0 P_{ws} dz \sim \tau U_s(0) \cos \Delta\theta = \rho_w u_*^{(w)2} U_s(0) \cos \Delta\theta, \quad (\text{S.237})$$

where $\tau = \rho_a u_*^{(a)2} = \rho_w u_*^{(w)2}$ is the air-sea interface stress and $\Delta\theta$ is the angle between the swell propagation direction and the local wind. Converting to a spatial attenuation rate (using $U_s(0) = a^2 \omega k$, $E = \frac{1}{2} \rho_w g a^2$, $c_g = g/(2\omega)$, $\omega^2 = gk$) gives an order-of-magnitude signed rate

$$\mu_{\text{CL}}^{(\text{qs})} \sim \frac{4 u_*^{(w)2} k^2}{g} \cos \Delta\theta. \quad (\text{S.238})$$

This quantity should not be conflated with the positive-definite stochastic attenuation coefficient μ_{SVF} . It is a slow, deterministic modulation of wave-current energy exchange whose sign is set by the local wind alignment, not the stochastic friction coefficient of the resolved swell mode derived from the Green-Kubo projection in Section S2. For $U_{10} = 10 \text{ m s}^{-1}$ and swell wavenumber $k \approx 0.02 \text{ m}^{-1}$, $u_*^{(w)} \approx 1.2 \times 10^{-2} \text{ m s}^{-1}$ and $|\mu_{\text{CL}}^{(\text{qs})}| \sim 2 \times 10^{-8} \text{ m}^{-1}$ -comparable to or smaller than μ_{SVF} .

For remote swell, the propagation direction is fixed by a distant storm and is only weakly correlated with the local wind direction. The angle $\Delta\theta$ therefore varies broadly along a trans-oceanic path, so the path-mean quasi-steady CL contribution is expected to be small owing to sign cancellations, although systematic biases from wind climatology cannot be excluded. Along any individual ray, the CL term need not vanish. Rather, it acts as a low-frequency, signed modulation on synoptic scales, not as the encounter-scale stochastic friction addressed by the SVF theory.

A heuristic encounter-scale force comparison supports the same ordering. Using $u_s \sim a^2 \omega k$ and $u_\phi \sim a\omega$, the force ratio scales as

$$\frac{|u_s \Omega|}{|u_\phi \omega'|} \sim ak \frac{\Omega}{\omega'}. \quad (\text{S.239})$$

For typical remote swell, $ak \sim 10^{-2}$ - 10^{-1} , so unless the mean-flow vorticity greatly exceeds the turbulent vorticity fluctuation, the CL force is subdominant at the encounter scale. We stress that this is only a scale argument. The cleaner distinction is the one above. The quasi-steady CL exchange is signed and low-frequency, whereas the SVF attenuation is positive-definite and arises from the autocorrelation of the mode-projected stochastic force.

For representative far-field conditions ($T \approx 14 \text{ s}$, $\varepsilon_{\text{eff}} \sim 5 \times 10^{-7} \text{ m}^2 \text{ s}^{-3}$), the SVF law gives $\mu_{\text{SVF}} \sim 0.5$ - $1 \times 10^{-7} \text{ m}^{-1}$. The SVF channel is amplitude-independent (Section S8), not signed by the local wind-swell alignment, and positive-definite ($\mu_{\text{SVF}} > 0$ always, by Theorem 1). We therefore regard remote swell as the regime in which breaking is suppressed and the quasi-steady CL modulation is sufficiently small that the SVF Green-Kubo friction can be isolated and tested. Within the present non-breaking, mode-level bulk-turbulence framework, SVF is the sole retained positive-definite stochastic friction channel for remote swell. Table S5 collects the numerical comparison, including the laminar air-viscous baseline. The classical upper limit for swell decay by laminar air-side viscous shearing [70, 71] is $\mu_v = (\rho_a/\rho_w g c_g)(2\pi/T)^{5/2} \sqrt{2\nu_{\text{air}}}$. For 10 s swell this gives $\mu_v \approx 3 \times 10^{-8} \text{ m}^{-1}$. For the 14-18 s period range typical of trans-oceanic swell, μ_v drops to $(3$ - $5) \times 10^{-9} \text{ m}^{-1}$, an order of magnitude below the SVF prediction (Table S5). Because $\mu_v \propto \omega^{7/2}$ decays faster with period than $\mu_E \propto \omega^{8/3}$, the SVF-to-viscous ratio grows as $T^{5/6}$ and the laminar channel is negligible throughout the remote-swell band. Even if the air-side

Table S5: Representative wave-energy exchange channels. Within the present non-breaking, mode-level bulk-turbulence framework, SVF is the sole retained positive-definite stochastic friction channel for remote swell. The laminar air-viscous rate [70] is included as a baseline.

Channel	Dominant regime	Sign	Typical μ (m^{-1})
Breaking	Wind sea	> 0	10^{-5} - 10^{-4}
Laminar air viscosity (Dore) ^a	All	> 0	3×10^{-9} - 3×10^{-8}
CL/Langmuir quasi-steady exchange	Remote swell	\pm	expected small in path mean
SVF	Remote swell	> 0	0.5 - 1×10^{-7}

^aLaminar (Stokes) solution [70, 71]. Even if the air-side boundary layer becomes turbulent at high orbital Reynolds number, available estimates still place the resulting enhancement well below the observed mean attenuation [18].

boundary layer becomes turbulent at high orbital Reynolds number, available estimates still place the resulting enhancement well below the observed mean attenuation [18, 71]. That the observed mean rate $\bar{\mu}_{\text{obs}} \sim 1.5 \times 10^{-7} \text{ m}^{-1}$ [61] exceeds the Dore laminar ceiling by a factor of ~ 5 was the original motivation for invoking turbulent mechanisms [18]. The SVF theory supplies the first zero-parameter, first-principles account of that turbulent excess.

References

- [1] G. K. Batchelor. *An Introduction to Fluid Dynamics*. Cambridge University Press, 1967.
- [2] Anqing Xuan, Bing-Qing Deng, and Lian Shen. Effect of an incoming Gaussian wave packet on underlying turbulence. *J. Fluid Mech.*, 999:A45, 2024.
- [3] O. M. Phillips. *The Dynamics of the Upper Ocean*. Cambridge University Press, 2nd edition, 1977.
- [4] J. Lighthill. *Waves in Fluids*. Cambridge University Press, 1978.
- [5] C. C. Mei, M. Stiassnie, and D. K.-P. Yue. *Theory and Applications of Ocean Surface Waves*. World Scientific, 2005.
- [6] J. C. McWilliams. *Quasi-linear Theory for Surface Wave-Current Interactions*. Springer, 2022.
- [7] A. D. D. Craik and S. Leibovich. A rational model for Langmuir circulations. *J. Fluid Mech.*, 73:401–426, 1976.
- [8] S. Leibovich. *On wave-current interaction theories of Langmuir circulations*, volume 99. 1980.
- [9] D. D. Holm. The ideal Craik–Leibovich equations. *Physica D*, 98:415–441, 1996.
- [10] J. C. McWilliams, P. P. Sullivan, and C.-H. Moeng. Langmuir turbulence in the ocean. *J. Fluid Mech.*, 334:1–30, 1997.
- [11] P. P. Sullivan, J. C. McWilliams, and W. K. Melville. Surface gravity wave effects in the oceanic boundary layer: Large-eddy simulation with vortex force and stochastic breakers. *J. Fluid Mech.*, 593:405–452, 2007.
- [12] P. P. Sullivan and J. C. McWilliams. Dynamics of winds and currents coupled to surface waves. *Annu. Rev. Fluid Mech.*, 42:19–42, 2010.
- [13] Yasushi Fujiwara, Yutaka Yoshikawa, and Yoshimasa Matsumura. A wave-resolving simulation of Langmuir circulations with a nonhydrostatic free-surface model: Comparison with Craik–Leibovich theory and an alternative Eulerian view of the driving mechanism. *J. Phys. Oceanogr.*, 48:1691–1708, 2018.
- [14] M. S. Green. Markoff random processes and the statistical mechanics of time-dependent phenomena. II. Irreversible processes in fluids. *J. Chem. Phys.*, 22(3):398–413, 1954.
- [15] R. Kubo. Statistical-mechanical theory of irreversible processes. I. General theory and simple applications to magnetic and conduction problems. *J. Phys. Soc. Jpn.*, 12(6):570–586, 1957.

- [16] S. Bochner. *Vorlesungen über Fouriersche Integrale*. Akademische Verlagsgesellschaft, Leipzig, 1933.
- [17] F. E. Snodgrass, G. W. Groves, K. F. Hasselmann, G. R. Miller, W. H. Munk, and W. H. Powers. Propagation of ocean swell across the Pacific. *Phil. Trans. R. Soc. Lond. A*, 259: 431–497, 1966.
- [18] F. Ardhuin, B. Chapron, and F. Collard. Observation of swell dissipation across oceans. *Geophys. Res. Lett.*, 36:L06607, 2009. doi: 10.1029/2008GL037030.
- [19] Justin E. Stopa, Fabrice Ardhuin, Romain Husson, Haoyu Jiang, Bertrand Chapron, and Fabrice Collard. Swell dissipation from 10 years of Envisat advanced synthetic aperture radar in wave mode. *Geophys. Res. Lett.*, 43:3423–3430, 2016. doi: 10.1002/2015GL067566.
- [20] Peter D. Craig and Michael L. Banner. Modeling wave-enhanced turbulence in the ocean surface layer. *J. Phys. Oceanogr.*, 24(12):2546–2559, 1994. doi: 10.1175/1520-0485(1994)024<2546:MWETIT>2.0.CO;2.
- [21] E. A. Terray, M. A. Donelan, Y. C. Agrawal, W. M. Drennan, K. K. Kahma, III A. J. Williams, P. A. Hwang, and S. A. Kitaigorodskii. Estimates of kinetic energy dissipation under breaking waves. *J. Phys. Oceanogr.*, 26(5):792–807, 1996. doi: 10.1175/1520-0485(1996)026<0792:EOKEDU>2.0.CO;2.
- [22] Stephen E. Belcher, Alan L. M. Grant, Kirsty E. Hanley, Baylor Fox-Kemper, Luke Van Roekel, Peter P. Sullivan, William G. Large, Andy Brown, Adrian Hines, Daley Calvert, Anna Rutgersson, Heidi Pettersson, Jean-Raymond Bidlot, Peter A. E. M. Janssen, and Jeff A. Polton. A global perspective on Langmuir turbulence in the ocean surface boundary layer. *Geophys. Res. Lett.*, 39(18):L18605, 2012. doi: 10.1029/2012GL052932.
- [23] B. J. Alder and T. E. Wainwright. Decay of the velocity autocorrelation function. *Physical Review A*, 1(1):18–21, 1970. doi: 10.1103/PhysRevA.1.18.
- [24] Adrean Webb and Baylor Fox-Kemper. Wave spectral moments and Stokes drift estimation. *Ocean Modelling*, 40:273–288, 2011. doi: 10.1016/j.ocemod.2011.08.007.
- [25] H. Mori. Transport, collective motion, and Brownian motion. *Prog. Theor. Phys.*, 33: 423–455, 1965.
- [26] R. Zwanzig. *Nonequilibrium Statistical Mechanics*. Oxford University Press, 2001.
- [27] Denis J. Evans and Gary P. Morriss. *Statistical Mechanics of Nonequilibrium Liquids*. Cambridge University Press, Cambridge, 2nd edition, 2008. doi: 10.1017/CBO9780511535307.
- [28] Umberto Marini Bettolo Marconi, Andrea Puglisi, Lamberto Rondoni, and Angelo Vulpiani. Fluctuation–dissipation: Response theory in statistical physics. *Physics Reports*, 461(4–6): 111–195, 2008. doi: 10.1016/j.physrep.2008.02.002.
- [29] Ming Han, Michel Fruchart, Colin Scheibner, Suriyanarayanan Vaikuntanathan, Juan J. de Pablo, and Vincenzo Vitelli. Fluctuating hydrodynamics of chiral active fluids. *Nature Physics*, 17:1260–1269, 2021. doi: 10.1038/s41567-021-01360-7.
- [30] É. Fodor, C. Nardini, M. E. Cates, J. Tailleur, P. Visco, and F. van Wijland. How far from equilibrium is active matter? *Phys. Rev. Lett.*, 117:038103, 2016.
- [31] Jean-Pierre Hansen and Ian R. McDonald. *Theory of Simple Liquids: With Applications to Soft Matter*. Academic Press, Oxford, 4th edition, 2013. ISBN 978-0-12-387032-2. doi: 10.1016/C2010-0-66723-X.
- [32] A. N. Kolmogorov. The local structure of turbulence in incompressible viscous fluid for very large Reynolds numbers. *Dokl. Akad. Nauk SSSR*, 30:301–304, 1941.
- [33] James R. Holton and Gregory J. Hakim. *An Introduction to Dynamic Meteorology*, volume 88 of *International Geophysics Series*. Academic Press, Amsterdam, 5th edition, 2013. ISBN 978-0-12-384866-6.
- [34] H. Jiang, J. E. Stopa, H. Wang, R. Husson, A. Mouche, B. Chapron, and G. Chen. Tracking the attenuation and nonbreaking dissipation of swells using altimeters. *J. Geophys. Res. Oceans*, 121:1446–1458, 2016.
- [35] F. Ardhuin and A. D. Jenkins. On the interaction of surface gravity waves and upper ocean

- turbulence. *J. Phys. Oceanogr.*, 36:551–557, 2006.
- [36] G. K. Batchelor. *The Theory of Homogeneous Turbulence*. Cambridge University Press, Cambridge, 1953.
- [37] S. B. Pope. *Turbulent Flows*. Cambridge University Press, 2000.
- [38] Ayal Anis and James N. Moum. Surface wave–turbulence interactions: Scaling $\varepsilon(z)$ near the sea surface. *J. Phys. Oceanogr.*, 25:2025–2045, 1995. doi: 10.1175/1520-0485(1995)025<2025:SWISNT>2.0.CO;2.
- [39] Zhihua Zheng, Ramsey L. Harcourt, and Eric A. D’Asaro. Evaluating Langmuir turbulence parameterizations in the ocean surface boundary layer. *J. Geophys. Res. Oceans*, 126:e2020JC016325, 2021. doi: 10.1029/2020JC016325.
- [40] F. P. Bretherton and C. J. R. Garrett. Wavetrains in inhomogeneous moving media. *Proc. R. Soc. Lond. A*, 302:529–554, 1968. doi: 10.1098/rspa.1968.0034.
- [41] M. A. C. Teixeira and S. E. Belcher. On the distortion of turbulence by a progressive surface wave. *J. Fluid Mech.*, 458:229–267, 2002.
- [42] H. Tennekes and J. L. Lumley. *A First Course in Turbulence*. MIT Press, Cambridge, MA, 1972.
- [43] H. Tennekes. Eulerian and Lagrangian time microscales in isotropic turbulence. *J. Fluid Mech.*, 67:561–567, 1975.
- [44] R. H. Kraichnan. Kolmogorov’s hypotheses and Eulerian turbulence theory. *Phys. Fluids*, 7:1723–1734, 1964.
- [45] K. R. Sreenivasan. On the universality of the Kolmogorov constant. *Phys. Fluids*, 7:2778–2784, 1995.
- [46] E. A. D’Asaro. Turbulent vertical kinetic energy in the ocean mixed layer. *J. Phys. Oceanogr.*, 31:3530–3537, 2001.
- [47] S. A. Thorpe. Langmuir circulation. *Annu. Rev. Fluid Mech.*, 36:55–79, 2004.
- [48] K. R. Sreenivasan and R. A. Antonia. The phenomenology of small-scale turbulence. *Annu. Rev. Fluid Mech.*, 29:435–472, 1997.
- [49] J. B. Edson et al. On the exchange of momentum over the open ocean. *J. Phys. Oceanogr.*, 43:1589–1610, 2013.
- [50] W. G. Large and S. Pond. Open ocean momentum flux measurements in moderate to strong winds. *J. Phys. Oceanogr.*, 11:324–336, 1981. doi: 10.1175/1520-0485(1981)011<0324:OOMFMI>2.0.CO;2.
- [51] S. D. Smith. Wind stress and heat flux over the ocean in gale force winds. *J. Phys. Oceanogr.*, 10:709–726, 1980. doi: 10.1175/1520-0485(1980)010<0709:WSAHFO>2.0.CO;2.
- [52] J. Wu. Wind-stress coefficients over sea surface from breeze to hurricane. *J. Geophys. Res.*, 87(C12):9704–9706, 1982. doi: 10.1029/JC087iC12p09704.
- [53] J. Thomson, M. S. Schwendeman, S. F. Zippel, S. Moghimi, J. Gemmrich, and W. E. Rogers. Wave-breaking turbulence in the ocean surface layer. *J. Phys. Oceanogr.*, 46:1857–1870, 2016. doi: 10.1175/JPO-D-15-0130.1.
- [54] P. Sutherland and W. K. Melville. Field measurements of surface and near-surface turbulence in the presence of breaking waves. *J. Phys. Oceanogr.*, 45:943–965, 2015. doi: 10.1175/JPO-D-14-0133.1.
- [55] E. Kunze. A unified model spectrum for anisotropic stratified and isotropic turbulence in the ocean and atmosphere. *J. Phys. Oceanogr.*, 49:385–407, 2019.
- [56] J. M. Klymak and J. N. Moum. Oceanic isopycnal slope spectra. Part II: Turbulence. *J. Phys. Oceanogr.*, 37:1232–1245, 2007.
- [57] G. D. Nastrom and K. S. Gage. A climatology of atmospheric wavenumber spectra of wind and temperature observed by commercial aircraft. *J. Atmos. Sci.*, 42:950–960, 1985.
- [58] E. Lindborg. The energy cascade in a strongly stratified fluid. *J. Fluid Mech.*, 550:207–242, 2006.
- [59] G. Brethouwer, P. Billant, E. Lindborg, and J.-M. Chomaz. Scaling analysis and simulation

- of strongly stratified turbulent flows. *J. Fluid Mech.*, 585:343–368, 2007.
- [60] T. Ishihara, T. Gotoh, and Y. Kaneda. Study of high-Reynolds number isotropic turbulence by direct numerical simulation. *Annu. Rev. Fluid Mech.*, 41:165–180, 2009.
- [61] H. Jiang, A. Mouche, H. Wang, A. Babanin, B. Chapron, and G. Chen. Limitation of the altimeter-derived swell attenuation: An example of swell propagation from the Southern Ocean. *Remote Sens. Environ.*, 200:244–253, 2017. doi: 10.1016/j.rse.2017.08.004.
- [62] S. A. Thorpe. Langmuir circulation. *Annual Review of Fluid Mechanics*, 36:55–79, 2004. doi: 10.1146/annurev.fluid.36.052203.071431.
- [63] Eric A. D’Asaro. Turbulence in the upper-ocean mixed layer. *Annual Review of Marine Science*, 6:101–115, 2014. doi: 10.1146/annurev-marine-010213-135138.
- [64] S. Zieger, A. V. Babanin, W. E. Rogers, and I. R. Young. Observation-based source terms in the third-generation wave model WAVEWATCH. *Ocean Model.*, 96:2–25, 2015.
- [65] Qingxiang Liu, W. Erick Rogers, Alexander V. Babanin, Ian R. Young, Leonel Romero, Stefan Zieger, Fangli Qiao, and Changlong Guan. Observation-based source terms in the third-generation wave model WAVEWATCH III: Updates and verification. *J. Phys. Oceanogr.*, 49:489–517, 2019. doi: 10.1175/JPO-D-18-0137.1.
- [66] Alexander V. Babanin. *Breaking and Dissipation of Ocean Surface Waves*. Cambridge University Press, 2011. doi: 10.1017/CBO9780511736162.
- [67] W. K. Melville. The role of surface-wave breaking in air–sea interaction. *Annu. Rev. Fluid Mech.*, 28:279–321, 1996.
- [68] O. M. Phillips. Spectral and statistical properties of the equilibrium range in wind-generated gravity waves. *J. Fluid Mech.*, 156:505–531, 1985.
- [69] O. M. Phillips. The equilibrium range in the spectrum of wind-generated waves. *J. Fluid Mech.*, 4(4):426–434, 1958. doi: 10.1017/S0022112058000550.
- [70] B. D. Dore. Some effects of the air-water interface on gravity waves. *Geophysical & Astrophysical Fluid Dynamics*, 10(1):215–230, 1978. doi: 10.1080/03091927808242638.
- [71] F. Collard, F. Ardhuin, and B. Chapron. Monitoring and analysis of ocean swell fields from space: New methods for routine observations. *J. Geophys. Res.*, 114:C07023, 2009. doi: 10.1029/2008JC005215.